Detection of benthic life by high-frequency hydroacoustic and seismic methods

vorgelegt von

Inken Katrin Schulze

Greifswald, 31.05.2022

Dekan: Prof. Dr. Gerald Kerth

1. Gutachter: Prof. Dr. Helge W. Arz

2. Gutachter: Prof. Dr. Sebastian Krastel

Tag der Promotion: 12.01.2023

Abstract

Seas and oceans are essential for the global ecosystem. Entire societies, economies and countless livelihoods rely on their good environmental status. Yet, pressures on marine environments are increasing. An extensive assessment and monitoring of marine habitats is a vital precondition for understanding these systems and their sustainable conservation. Remote sensing methods can temporally accelerate the mapping, improve the spatial resolution and support the interpretation of large areas. Hydroacoustic becomes the method of choice for areas deeper than the coastal zone as optical signals are limited by strong attenuation in the water column. Apart from depth measurements for the creation of bathymetric charts, the recording of backscatter strength is useful for the characterization of the seafloor surface. The direct influence of the inhabiting benthic community on the backscattered signal is rarely considered, although it can be utilized for the detection of benthic life. Information about habitat-specific backscatter responses or a hydroacoustic remote sensing catalog for benthic habitats is missing so far.

The multibeam echosounder (MBES) has the advantage of recording both, bathymetry and backscatter strength simultaneously with related incidence angle. Further, recent technological developments allow to change between frequencies. Angular range curves supported the quantification of backscatter strength of different frequencies. Acoustic data sets were complemented by ground truthing in form of sedimentological and biological samples as well as video profiles. Study areas were located offshore the island of Sylt in the North Sea as well as in vicinity to Oder Bank and close to the coast offshore Hohe Düne/Rostock, both in the Baltic Sea. Investigated habitats included sand areas inhabited by tubeworms, loose mussel clusters on top of sand areas, seagrass meadows, coarse sand and gravel areas, and a reef covered by mussels.

Multifrequency backscatter maps, combining frequencies between 200 kHz and 700 kHz, illustrate small-scale features at the seafloor not visible in monofrequent maps. Key habitats showed a specific backscatter response, which can partly be related to macrobenthic flora and fauna. Data sets recorded with a (partly calibrated) MBES in three different month (May, August, October) revealed that backscatter strength can further detect spatial as well as temporal habitat dynamics. Alterations in the sediment composition at the seafloor surface of the ecologically valuable coarse sand and gravel areas were caused by seasonal changes in local hydrodynamics.

A newly developed 3D seismic lander has the ability to support hydroacoustic remote sensing as an additional, non-destructive ground truthing method utilizing a high frequency of 130 kHz to image the shallow subsurface. Buried objects, e.g., stones, shells, fruit gummy worms, as well as sediment disturbances could be detected and visualized in a laboratory experiment. The 3D seismic lander is likely to improve the investigation of volume scatter contribution to backscatter strength and is potentially applicable for the imaging of bioturbation.

Zusammenfassung

Meere und Ozeane sind unentbehrlich für das globale Ökosystem. Ganze Gesellschaften, Wirtschaftssysteme und unzählige Existenzgrundlagen hängen von ihrem gutem ökologischen Zustand ab, trotzdem erhöhen sich die Belastungen auf die marine Umwelt. Eine umfassende Bestandsaufnahme und Überwachung der marinen Lebensräume ist eine notwendige Voraussetzung für ein Verständnis dieser Systeme und ihrer nachhaltigen Erhaltung. Fernerkundungsmethoden können die Kartierung großer Gebiete auf zeitlicher Ebene beschleunigen, in der räumlichen Auflösung verbessern und im Inhaltsgehalt unterstützen. Hydroakustik wird zum Mittel der Wahl für Gebiete tiefer als die Küstenzone, da die Signale optischer Methoden durch die Wassersäule stark gedämpft werden. Neben der Tiefenmessung zur Erstellung bathymetrischer Karten ist die Aufzeichnung der Rückstreustärke nützlich zur Beschreibung der Beschaffenheit der Meeresbodenoberfläche. Der direkte Einfluss der benthischen Gemeinschaft auf das zurückgestreute Signal wird selten betrachtet, dabei kann dieser für die Detektion benthischen Lebens genutzt werden. Informationen über habitatspezifische Rückstreustärken oder eine Katalog über die hydroaktustische Fernerkundung benthischer Habitate fehlen bisher.

Das Fächerecholot hat den Vorteil, dass es gleichzeitig sowohl die Bathymetrie als auch die Rückstreustärke einschließlich des zugehörigen Einfallswinkels aufzeichnet und zwischen den Frequenzen gewechselt werden kann. Winkelbereichs-Kurven (angular range curves) unterstützten die Quantifizierung der Rückstreustärke verschiedener Frequenzen. Die akustischen Datensätze wurden durch Ground-Truth-Daten in Form von sedimentologischen und biologischen Proben sowie Videoprofilen ergänzt. Die Untersuchungsgebiete befinden sich vor der Insel Sylt in der Nordsee, sowie in der Ostsee nahe der Oderbank und vor der Küste bei Hohe Düne/Rostock. Die untersuchten Habitate bestehen aus Sandgebieten besiedelt mit Röhrenwürmern, losen Muschelkonglomeraten auf sandigem Untergrund, Seegraswiesen, Kies- und Grobsandgebieten und einem mit Muscheln bedeckten Riff.

Multifrequente Rückstreukarten, die Frequenzen zwischen 200 kHz und 700 kHz kombinieren, bilden kleinskalige Merkmale am Meeresboden ab, die in monofrequenten Karten nicht sichtbar sind. Die Habitate weisen eine spezifische Rückstreustärke auf, welche teilweise auf makrobenthische Flora und Fauna zurückgeführt werden kann. In den Datensätzen, die mit einem (teilweise kalibrierten) Fächerecholot in drei verschiedenen Monaten (Mai, August, Oktober) aufgezeichnet wurden, zeigt sich, dass die Rückstreustärke räumliche als auch zeitliche Dynamiken aufzeigen kann. Veränderungen der Sedimentzusammensetzung an der Meeresbodenoberfläche in den ökologisch wertvollen Kies- und Grobsandgebieten sind durch saisonale Änderungen der lokalen Hydrodynamik verursacht.

Ein neuentwickelter 3D-seismischer Lander hat als weitere, zerstörungsfreie Ground-Truth-Methode die Fähigkeit hydroakustische Fernerkundungsmethoden zu unterstützen. Unter Verwendung einer hohen Frequenz von 130 kHz kann der flache Untergrund abgebildet

werden. Sowohl vergrabene Objekte, zum Beispiel Steine, Muschelschalen, Fruchtgummiwürmer, als auch Störungen im Sediment konnten in einem Laborexperiment erkannt und visualisiert werden. Der 3D-seismische Lander ist voraussichtlich dafür geeignet die Erforschung des Beitrags der Volumenstreuung zur Rückstreustärke zu verbessern und ist potentiell einsetzbar zur Abbildung von Bioturbation.

Contents

<div style="text-align: right;">

Chapter 1

</div>

Introduction

1.1 Marine Habitat Mapping

The exhaustive mapping and monitoring of the seafloor using remote sensing is necessary to obtain a comprehensive view on the marine environment and is therefore of high societal and scientific importance. Remote sensing comprises both, optical methods in very shallow water, while acoustics techniques are the method of choice for intermediate and deeper water depths.

Importance of Marine Environments

Oceans and seas are crucial for global biological diversity and the well-being of humanity. Marine ecosystems provide food, especially fish as a protein source, maintain water quality and produce oxygen. Furthermore, the marine environment is an important factor for the prosperity of economies around the world (United Nations Environment Programme, 2012). For instance, around 90% of transportation between countries is offshore (Walker et al., 2019). Coastal areas are popular for leisure and recreation purposes. Half of touristic travels lead to coastal areas and tourism can be a major contribution to the gross domestic product (GDP) especially in developing countries (Davenport & Davenport, 2006). The oceans play an important role in the regulation of the climate, e.g., by absorption of carbon dioxide or the global distribution of solar energy.

Pressure on Marine Environments

The marine ecosystems are under increasing pressures, most of which can be accounted to humanity (Steffen, Broadgate, Deutsch, Gaffney, & Ludwig, 2015). The anthropogenic pressures on marine environments, especially driven by economic interests, are increasing (e.g., tourism, transportation, submarine infrastructure, dredging of sand and gravel for construction, deep sea mining, offshore wind parks, farming, commercial fishing) with the consequence of increasing amounts of, e.g., pollution, marine litter, invasive species, habitat destruction, nitrification, overfishing and underwater noise (Harris, 2020; HELCOM, 2018). Effects of the climate change in the ocean include, e.g. an increase of fresh water influx by melting glaciers, the acidification by a higher concentration of carbon dioxide or an increase in water temperature (Turley et al., 2016).
Consequences for the marine environment are already visible on a regional scale, e.g., by the loss of populations or species. These rising pressures first lead to stressed and degenerated habitats, then to irreparable damages. It is essential to reduce the pressures of the anthropocene on ecosystems and find a balance between economic and ecological interests before they are damaged beyond the point of recovery (Dryzek & Pickering, 2018; Steffen et al., 2015).

Protection of Marine Environments

A regulatory framework for a sustainable use of the seas is a first step towards the preservation of the marine environment. As oceans are not restricted to country borders, there is a demand for assessment and protection measures on international level.

The 17 Sustainable Development Goals (SGDs) implemented in 2016 by the United Nations (UN) is a global plan to achieve a good living and a sustainable future for all. It is addressed to governments as well as to societies, economy and science. SGD 14 'Life Below Water' focuses on the conservation and sustainable use of the ocean, sea and marine resources (United Nations, n.d.-a). The importance of oceans for humanity is even more emphasized by the United Nations by proclaiming the Decade of Ocean Science for Sustainable Development (2021-2030) (United Nations, n.d.-b).

On European level, the Marine Strategy Framework Directive (MSFD) was put in place in 2008 and scheduled for implementation on national level for 2010 (European Parliament, Council of the European Union, 2008). The MSFD is the first EU directive to oblige the EU member states to ensure a 'Good Environmental Status' (GES) of their waters by 2020. GES is defined as

> ...the environmental status of marine waters where these provide ecologically diverse and dynamic oceans and seas which are clean, healthy and productive within their intrinsic conditions, and the use of the marine environment is at a level that is sustainable, thus safeguarding the potential for uses and activities by current and future generations...
>
> (Article 3(5), European Parliament, Council of the European Union (2008))

The development of a marine strategy starts with the assessment and definition of GES and environmental targets. After monitoring programs are developed and implemented, programs of measures are developed and implemented. The MSFD follows an adaptive approach, which means national marine strategies must be reviewed in a cycle of 6 years. A number of eleven qualitative descriptors, comprising detailed criteria and methodological standards, were set out and revised, to support the the EU members states with the implementation (European Commission, 2017).

In Germany, the Bundesamt für Naturschutz (BfN) is responsible for the implementation of the MSFD within the exclusive economic zone (EEZ) in North Sea and Baltic Sea. The coastal waters (12-mile zone) fall within the competence of the Bundesländer. In total, about 45% of the German waters (coastal and EEZ) are under protection.

Especially the assessment and monitoring of the marine environments rely on accurate information about habitat distribution and dynamics. In some countries large marine mapping initiatives exist to create such a database. In Norway, several institutions work together in the MAREANO project to collect a variety of detailed information of the Norwegian offshore areas (Bøe et al., 2020). Other examples are MAREMAP in the United Kingdom (Howe, Stevenson, & Gatliff, 2014) or the Integrated Marine Plan for Ireland (Inter-Departmental Marine Coordination Group, 2012).

Remote Sensing of Marine Environments

Remote sensing of marine environments is an important tool for marine spatial planning of the authorities and it supports the design and monitoring of marine protected areas (MPA). Remotely sensed information provide a base for scientific research on benthic habitats and the seafloor geology as well as for the economical use of the sea (Harris & Baker, 2020). Remote sensing enhances, e.g., the analysis of spatial distribution and dynamics of marine habitats and temporal dynamics. In addition, observation of possible anthropogenic impacts on the marine ecosystems can be imaged directly (e.g., trawling or dredging) and

indirectly (e.g., changing extension of seagrass meadows), thereby supporting a sustainable use of the sea.

Over the past decades onshore remote sensing methods, particularly satellites equipped with optical sensors, became a sophisticated tool for mapping the Earths surface including the biodiversity. The wide range of possibilities include the direct identification of individual objects, species communities or habitats. Furthermore, additional information can be indirectly derived from remote measured environmental parameters (Turner et al., 2003). This onshore methods are expanded to the coastal area to map shallow water habitats, e.g. seagrass in the turbid water of the Baltic Sea (Kuhwald, Schneider von Deimling, Schubert, & Oppelt, 2021). Apart from the optical, other bands of the electromagnetic spectrum are utilized for satellite-based remote sensing, e.g., radar or infrared, each beneficial for specific issues.

Another remote sensing method is the airborne LiDAR (Light Detection and Ranging) utilizing laser scanning for mapping with a covering of more than 10 km^2/h is possible. Similar to SoNAR (Sound Navigation and Ranging) methods, both, the topography and backscattered intensity, and recently the full waveform, can be recorded with a resolution of less than 1 m. Besides the onshore use, it is a very powerful for the mapping of coastal region by the ability to cover the transition area from land to water. Offshore mapping with LiDAR is possible up to 1.5 times the Secchi depth (Niemeyer, Song, Kogut, & Heipke, 2015). The Secchi depth in the Baltic Sea is rarely exceeds 10 m, but often only a few meters (Stock, 2015). LiDAR is suitable to map vegetation (Tulldahl & Wikström, 2012) and boulders (Hansen et al., 2021) in this depth range.

Optic remote sensing methods are efficient for mapping the (marine) environment concerning costs, time and resolution. However, penetration depth is limited as electromagnetic waves in the optical spectral range are strongly absorbed by (sea) water. Additionally, turbidity can reduce the data quality. On the contrary, acoustic waves propagate well in water and hydroacoustics becomes the method of choice for underwater mapping in depths greater than a few meters.

1.1.1 Acoustic Benthic Habitat Mapping

The general approach in the creation of habitat maps is the spatial integration of in situ sampling data and (often remotely sensed) continuous layers of environmental data. Benthic habitats are closely linked to sediment conditions (Tecchiato, Collins, Parnum, & Stevens, 2015), so in many cases the hydroacoustic mapping aims to discriminate sediment compositions (Tauber, 2012). Traditionally, seafloor maps based on acoustic data show distinct borders of separated units, which do exist, but in nature shifts between seafloor characteristics can also be gradational. Therefore, Brown, Smith, Lawton, and Anderson (2011) define the term of 'marine habitat mapping' as:

> *The use of spatially continuous environmental data sets to represent and predict biological patterns on the seafloor (in a continuous or discontinuous manner).*

Further, Brown et al. (2011) provide a comprehensive review of acoustic methods used for benthic habitat mapping including a extensive list of studies (published before 2011). Most investigations include both, bathymetry and backscatter data, on a medium (1-10 km) or broad (>10 km) scale, and collected, i.a., geological and/or biological data for ground truthing. Acoustic techniques involve mostly sidescan sonar (SSS), singlebeam echosounder (SBES) and/or multibeam echosounder (MBES). High-frequency acoustic backscatter is the most utilized data for habitat mapping. Nowadays, MBES represents the state of art and is favorably used by many scientists for benthic habitat mapping (see also Chapter 1.4.1).

Approaches for the segmentation of backscatter data developed from expert interpretation

by human eye to automated segmentation. Automated segmentation can either be image-based, where backscatter mosaics are divided into areas of similar backscatter strength (Brown et al., 2011), for instance by textural analysis based on gray-level co-occurrence matrices (Blondel & Gómez Sichi, 2009; Feldens, 2017; Lucieer, Hill, Barrett, & Nichol, 2013), object-based image analysis (Janowski et al., 2018) or machine learning (Diesing et al., 2014). Signal-based segmentation methods include, for example, angular range analysis (ARA) (Fonseca, Brown, Calder, Mayer, & Rzhanov, 2009; Hellequin, Boucher, & Lurton, 2003) or machine learning approaches (Hasan, Ierodiaconou, & Monk, 2012).

However, the quantitative understanding of high-frequency backscatter data for complex seafloor surfaces, especially considering the influence of benthic organisms, is limited. This is caused by missing interdisciplinary data acquisition and analysis. A more holistic approach could include the direct detection of macrobenthic life. Macrobenthic organisms, their shells, casts or tubes structures (Heinrich, Feldens, & Schwarzer, 2017) modify the seafloor roughness and affect therefore the acoustic backscattering directly. Additionally, bioturbation processes alter the near subsurface, which is within the penetration range of high-frequency acoustic imaging. The acoustic detection of vegetation on the seafloor is additionally supported by heights visible in bathymetric measurements or enclosed gas bubbles, which acoustic waves are sensitive to (e.g., seagrass meadows (Ballard et al., 2020; Held & Schneider von Deimling, 2019) or macroalgae (Kruss, Tęgowski, Tatarek, Wiktor, & Blondel, 2017)).

Ground Truthing

Ground truthing is necessary to relate remote sensing data to the real nature of objects or substrates. It allows for a calibration of the remotely gathered data, which is crucial for the interpretation of data. In hydroacoustics, ground truthing is essential to link acoustic maps (bathymetry or especially backscatter strength) to geological or biological characteristics of the seafloor, ideally establishing a direct inversion. Most ground truthing is conducted in the form of point samples or sampling along profiles, which results in a (very) small area coverage. Furthermore, sample collection and following evaluation are often time consuming and therefore associated with high costs. Therefore, a thorough planning of location and amount of sampling stations in advance is beneficial.

There is a variety of in situ methods available for ground truthing of marine acoustic data. Physical sample collection includes, e.g., grabs, dredges, corers, nets, traps, or research divers, each providing a certain range of surface cover, accuracy and recovery depth (Eleftheriou & Moore, 2013; Jørgensen, Renaud, & Cochrane, 2011). These methods are of destructive nature and subject to possible alterations by, e.g, transport or decay. Optical methods such as video footage (Beisiegel, Darr, Gogina, & Zettler, 2017), photography or laser-line scanning (Schönke et al., 2017) are mainly non-destructive. However, the observation of the seafloor is restricted to the surface and sometime to certain angles.

The 3D seismic lander presented in Chapter 5 provides a new, non-destructive possibility of in situ ground truthing. The 3D imaging of the near-subsurface offers chances to investigate and monitor, e.g., burrowing macrobenthos and its traces.

1.1.2 BONUS ECOMAP Project

The preparation of this thesis was embedded in the BONUS ECOMAP project (with the full title *Baltic Sea environmental assessments by innovative opto-acoustic remote sensing, mapping, and monitoring*), which officially lasted from 2017 to 2020 (Schneider von Deimling & Feldens, 2021). An international consortium of scientists at institutes and companies in the three Baltic Sea countries Poland, Denmark and Germany worked together. One

industrial partner was the multibeam sonar manufacturer Norbit Subsea, who developed and provided a calibrated device and associated software used in many surveys during the project.

The aim of the project was to test the possibilities of latest optical and acoustic remote sensing methods operating at the seafloor surface for habitat monitoring purposes including corresponding processing algorithms. The holistic approach integrated (calibrated) multibeam echosounders, shallow 3D seismics, and airborne LiDAR (Light detection and ranging) to collect new data sets of different Baltic Sea habitats of various scales (Figure 1.1). Hereby, the target zone was the near seabed domain comprised of the seafloor surface itself, the macrobenthic life and vegetation thereon, and the very shallow subsurface. This included, e.g., seagrass meadows, burrowing macrofauna, stone reefs, and shallow gas areas. A further goal was the development of suitable ground truthing and calibration methods to establish a quantitative relation between optical and acoustic data. The data processing aspect of the project included the development of full waveform analysis tools and other algorithms such as statistical analyses and machine learning tools to classify and interpret the response from different habitats, especially the macrobenthic life. The idea was to conclude the project with a remote sensing catalog gathering all results to share with other researchers and authorities.

The papers of this thesis are closely linked to the objectives of the work package located at the Leibniz Institute for Baltic Sea Research Warnemünde (IOW) focusing on small-scale habitats. The working groups *Marine Geophysics* and *Ecology of Benthic Organisms* collaboratively investigated the impact of macrofauna communities at the seafloor on roughness parameters, multifrequency backscatter strength as well as volume scatter strength to improve the discrimination power of remote sensing data regarding the identification and monitoring of marine habitats.

Acoustic data sets and corresponding sedimentological and biological ground truthing samples were collected during (repeated) surveys at different study sites at different times of the year. The focus was on the use of multiple frequencies for the measurement of backscatter strength (Chapters 2 and 3), which also allowed to investigate the seasonal dynamics of backscatter strength of key habitats (Chapter 4). A newly developed high-frequency 3D seismic lander was tested for the possibility of detecting burrowing macrofauna. In the laboratory, objects of benthic origin and simulated bioturbation structures were successfully imaged (Chapter 5). A field application and the combined use with an available laser line scanner is still pending (Section 6.1).
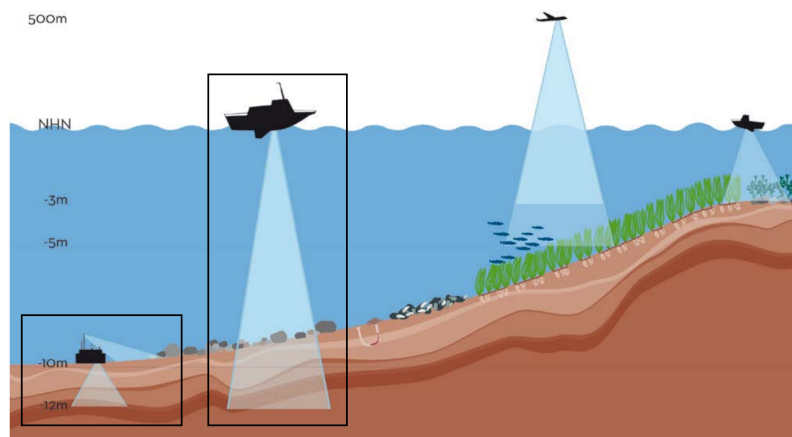

Figure 1.1: Overview of the acoustic and laser remote sensors and habitats investigated in the ECOMAP project. The two working areas targeted in this thesis are marked with black boxes.

1.2 Thesis Objectives

The overall research question of this thesis is whether benthic life and according traces can be detected with acoustic signals. In the context of the international BONUS ECOMAP project an interdisciplinary approach should investigate and expand the possibilities of remote sensing for the detection of marine organisms. The focus was on selected facies located in shallow waters of the Baltic Sea, where the seafloor is primarily dominated by macrobenthic organisms. The chapters of this thesis concentrate on the following objectives:

Backscatter response to different frequencies (Chapters 2, 3 and 4)
Multifrequency surveys using a multibeam echosounder investigate the frequency-dependent backscatter response of different habitats to enhance discrimination power of marine remote sensing.

Backscatter response to seasonal habitat changes (Chapter 4)
Seasonal habitat variability caused, e.g., by annually changing water conditions or life cycles of benthic organisms are expected to change the high-frequency scattering of the seafloor. Repeated multifrequency surveys over the course of an annual cycle with a (partly calibrated) multibeam echosounder investigate the seasonal backscatter dynamics of biotic and abiotic features in key habitats.

High-frequency 3D seismic lander for in situ-ground truthing (Chapter 5)
Burrowing organisms, their traces and eventual (tube) constructions are assumed to act as discrete scatterers and increase acoustic volume scatter due to differences in the acoustic impedance compared to surrounding sediment. The study investigates whether features within the high-frequency 3D seismics correspond to the distribution of burrowing macrofauna in a laboratory setting.

The theoretical foundations of the used acoustic remote sensing methods are described in the following section.

1.3 Theoretical Background

The section on the theoretical background of acoustic backscatter generally references from Lurton and Lamarche (2015), Lurton (2010), Jackson and Richardson (2007) and L-3 Communications SeaBeam Instruments (2000).

An acoustic wave travels through a fluid as an alternation of compression and decompression. These changes in pressure can be detected by, e.g., human ears, microphones or hydrophones.

An acoustic wave can be used to measure the water depth by recording the time (t) between the transmission and reception. When the sound speed (c) is known (for seawater typically around 1500 m/s), the water depth or range (R) is:

$$R = 0.5 * c * t \tag{1.1}$$

The factor 0.5 results from the acoustic signal traveling twice through the water column.

An acoustic wave transmitted by a sonar interacts with the seafloor, where its energy is split in different parts (Figure 1.2):

(Specular) Reflection
A incident wave is reflected at a sufficiently smooth interface at an angle symmetrical to the incidence angle away from its source. The intensity of the reflected fraction of the acoustic wave is dependent on the acoustical impedance contrast at the interface of medium 1 and medium 2, and the incidence angle (θ_i). The recording of the reflected wave is only possible if transducer and receiver are physically separated, except for case of the sounding perpendicular to the seafloor surface.

The acoustic impedance (Z) represents the "hardness" of a medium and is the product of the density (ρ) and sound speed (c).

$$Z = \rho c \tag{1.2}$$

The reflection coefficient (V) represents the ratio of reflected to incident energy based on the impedance contrast and is at normal incidence ($\theta_i = 0$):

$$V_{normal} = \frac{Z_2 - Z_1}{Z_2 + Z_1} \tag{1.3}$$

At oblique incidence the reflection coefficient is:

$$V_{oblique} = \frac{Z_2 cos\theta_i - Z_1 cos\theta_t}{Z_2 cos\theta_i + Z_1 cos\theta_t} \tag{1.4}$$

with the incidence angle (θ_i) and the transmission angle (θ_t), which are related by Snell's law (Equation 1.5).
Reflection of acoustic waves is the main process utilized for reflection seismic imaging (Section 1.3.3).

Transmission
A fraction of the incident wave is transmitted or refracted into the sediment. The

angle of transmission (θ_t) is dependent on the contrast of sound speed at the interface following Snell's law:

$$\frac{sin\theta_i}{c_1} = \frac{sin\theta_t}{c_2} \tag{1.5}$$

with the incidence angle θ_1, transmission angle θ_2, sound speed of the first medium c_1 (water) and sound speed of the second medium c_2 (sediment). However, Equation 1.5 is only valid if $\theta_2 \leq 1$. The limit angle, called *critical angle* (θ_c), can by given by:

$$\theta_c = arcsin(c_1/c_2) \tag{1.6}$$

For angles θ smaller than θ_c (Equation 1.6) a transmission into the second medium is impossible. If $c_2 > c_1$, the acoustic wave is totally reflected at angles larger θ_c. Otherwise, if $c_2 < c_1$, the reflection coefficient can become very small or zero, meaning that most or all of the energy is transmitted into the second medium. This is only likely to happen for very soft sediments, but can be relevant in the Baltic Sea basins (Schneider von Deimling, Held, Feldens, & Wilken, 2016).

Scattering

A fraction of the incident wave is spherically scattered at the interface and within the sediment volume. These processes are described in more detail in Section 1.3.2.
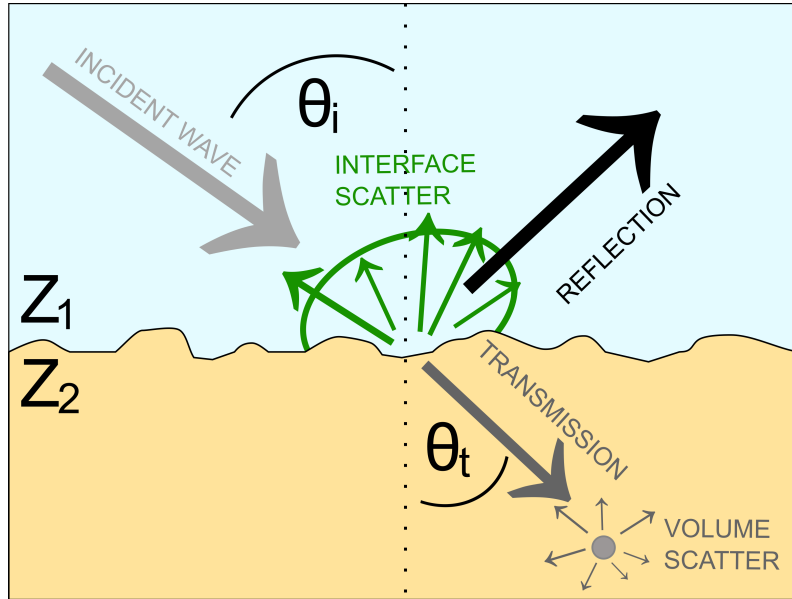

Figure 1.2: Reflection, transmission and scattering of a incident wave at the seafloor surface.

1.3.1 The Sonar Equation

The path of the acoustic wave from sending, scattering at the seafloor, propagation through the water column and to reception can be simplified represented in the sonar equation:

$$EL = SL - 2TL + TS \tag{1.7}$$

The contributing parts and their dependencies are described in the following.

Source Level (SL)

The transmitted source level is the amount of energy transmitted by a transducer as

an acoustic signal. However, the source level is complicated to determine as it is the sum of a device-specific transmitter directivity pattern, dependent on the frequency and two angles, and the nominal source level, dependent on the frequency, pulse length, power settings, band width and transmitted beam width. For calibration purposes (described in 1.4.1), the source level needs to be exactly known by the manufacturer.

Transmission Loss (TL)

The amplitude of the acoustic signal attenuates while traveling through the water column due to the effects of spherical spreading and absorption (α). The spreading can be geometrically accounted for under the assumption of a spherical propagation of the acoustic wave and is dependent on the range (R) from the source. The absorption is dependent on seawater properties, e.g., temperature and salinity, as well as the frequency of the signal. A specific absorption coefficient can be calculated using formulas with different ranges of validity and is usually given in units of dB/km.

$$TL = 20logR + \alpha R \tag{1.8}$$

The transmission loss is accounted twice for in the sonar equation as the acoustic signal passes the water column two times (transducer-seafloor-transducer).

Echo Level (EL)

The intensity of the scattered acoustic signal received back is called echo level. The echo level is the sum of the received signal, dependent on the frequency and two angles, the device-specific receiver directivity pattern, dependent on two angles, and the receiver response, dependent on the receiver and a time varying gain. For calibration purposes (described in 1.4.1), the source level needs to be exactly known by the manufacturer.

When measuring the echo level, not only the wanted scattered acoustic signal is received, but also an unknown contribution of noise. This underwater noise can result from anthropogenic sources (e.g, ship traffic, construction work), marine animals, from the sonar device itself or the carrying vessel or reverberation (e.g., unwanted scattering from objects within the water column). However, the noise level (NL) is assumed to be negligibly small compared to the wanted signal.

Target Strength (TS)

The target strength describes the relation of the incidence intensity (I_i) of the acoustic wave reaching the target to the intensity scattered (I_s) in the direction of the receiver.

$$TS = 10log_{10}\left[\frac{I_s}{I_i}\right] \tag{1.9}$$

The scattered intensity depends on the characteristics of the target and on the acoustic signal, including, e.g., the frequency, pulse length, geometry of the target and the signal. Considering the insonified area (A) on the seafloor, the target strength can be expressed as:

$$TS = BS + 10logA \tag{1.10}$$

The backscatter strength (BS) at an interface is given in decibel per unit area (dB per m^2) and is dependent on the incidence angle. The insonified area, also called *footprint*, is dependent on the incidence angle (θ_i), the range (R), the sound speed in water (c), the equivalent beamwidth (φ_{eq}) and the pulse length (τ). Therefore, the target strength at oblique incidence is:

$$TS(\theta_i) = BS(\theta_i) + 10log\left[R\phi_{eq}\frac{c\tau}{2sin\theta_i}\right] \tag{1.11}$$

1.3.2 Backscatter Strength (BS)

The scattering process at the seafloor is, apart from the frequency of the transmitted acoustic wave, independent of sonar properties. However, the backscattered signal is strongly dependent on the incidence angle and the seafloor roughness. At angles around perpendicular to the seafloor the echo is specular reflected and reaches maximum intensity. In practice, the backscatter analysis is limited to angles between 15to 70. Steeper angles are within the specular zone, where intensities are unsteady, while at grazing angles the signal-to-noise ratio decreases and uncertainties in footprint areas increase (Lurton & Lamarche, 2015).
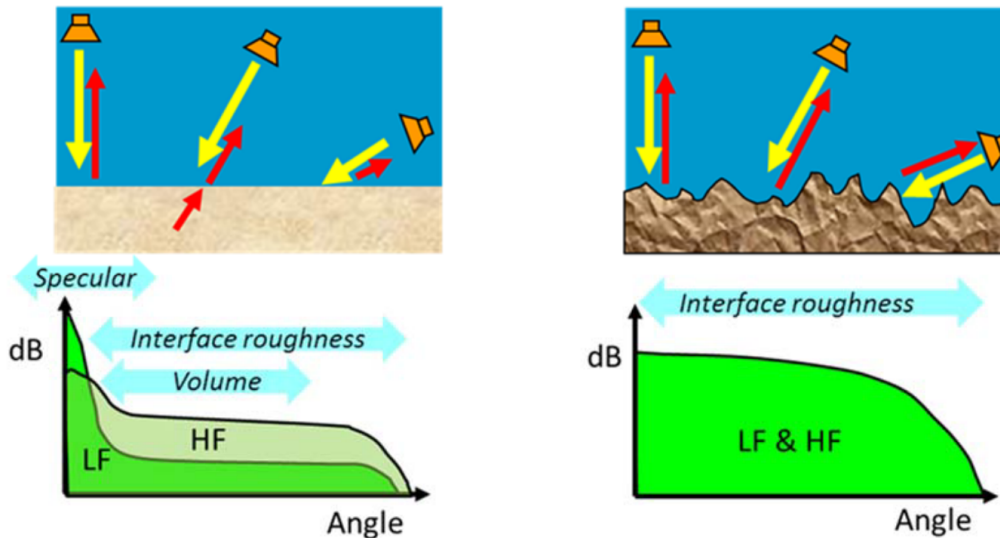

Figure 1.3: Intensity of backscatter as a function of incidence angle for soft sediments with a smooth surface (left) and coarse sediments with a rough surface (right). The difference between high frequency (HF) and low frequency (LF) is much larger for soft sediments (Lurton & Lamarche, 2015)

.

Surface Scattering

The scattering process at the seafloor surface is strongly dependent on the interface roughness in relation to the wavelength (λ) of the signal and can be described using statistical models. Expressing the geometrical roughness as standard deviation (h) of the interface, then a surface is considered 'smooth' for h $<$ λ and specular reflections are of high intensity, while scattering plays a minor role. For h $>$ λ, a interface is considered 'rough' and most of the incident acoustic energy is scattered (Lurton & Lamarche, 2015).

In acoustic field surveys during this thesis, wavelengths ranging from 75 mm at 200 kHz frequency to 2.14 mm at 700 kHz were used. This is the same scale as grain sizes of common sediments in the investigation areas, e.g., sand (0.063-2 mm) or gravel (2-63 mm). Therefore, the roughness of investigated seafloors is frequency-dependent. However, morphological effects as, e.g., ripples, or the presence of benthic flora or fauna should not be neglected as an increase in seafloor roughness can be induced by, e.g., tubeworms, even at low coverage of less than 2% (Schönke et al., 2017).

There are different approaches to quantify the roughness. A simple one is the calculation of a probability density function (pdf) sketched in Figure 1.4. An alternative representation is the roughness power spectrum of a seafloor surface (a more detailed description is given by, e.g., Jackson and Richardson (2007)).
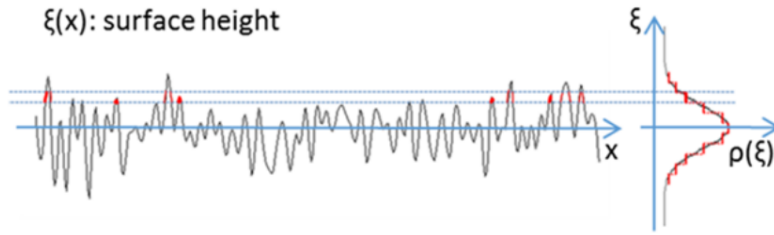
Figure 1.4: The roughness of an interface profile can be expressed in a probability density function (pdf) by inserting the distance (x) and the elevation (ξ) relative to the average of the interface (Lurton & Lamarche, 2015).

Volume scattering

Usually, high frequencies with a high attenuation are used for habitat-mapping for which the received backscatter strength is assumed to be related to an insonified area. However, acoustic signals penetrate the seafloor whereby volume scatter can contribute significantly to the total backscatter strength.

Volume scatter can occur when the transmitted incident wave encounters changes in the acoustic impedance in the sediment, caused either by objects (e.g., gas bubbles (Schneider von Deimling et al., 2013), burrowing macrofauna, shell fragments) or heterogeneities in the substrate composition (e.g., changes in sound speed or density caused by layering). The intensity of the acoustic wave penetrating into and out of the seafloor is dependent on the transmission coefficient, the attenuation within the sediment and the scattering process within the sediment.

The volume backscatter strength is highly dependent on the incidence angle and reaches its maximum at intermediate oblique angles. The specular effect dominates at low incidence angles and at high incidence angles only little of the acoustic wave is transmitted into the sediment. Low frequencies provoke a higher volume scatter due to less absorption. Finally, the sediment grain size influences the volume scatter, with the largest effect found in soft sediments. The small impedance contrast at the water-sediment interfaces allows for high transmission, the absorption in the soft sediment is low, fine-grained sediments are likely to host organisms and gas bubbles, and less surface scatter due to low roughness enhances the contribution to volume scattering (Lurton & Lamarche, 2015).

Modeling volume scatter is very complex due to the various parameters and unknown contributions. However, volume scattering can be a chance to experimentally obtain information about the very near subsurface and the corresponding benthic habitat.

Angular Dependence of Backscatter Strength

The strong angular dependence of backscatter strength can be utilized as a seafloor characterization feature. An established method are angular range curves (ARCs) for the differentiation of surface sediments (Fonseca et al., 2009; Fonseca & Mayer, 2007; Hellequin et al., 2003). The ARCs of different frequencies further enhance the discrimination power.

The angular backscatter strength is:

$$\overline{BS(\theta)} = EL(\theta) - SL + 2TL - 10log(\overline{A(\theta)}) \tag{1.12}$$

In this thesis ARCs are calculated for backscatter data sets in Chapters 2, 3 and 4.

Frequency Dependence of Backscatter Strength

The frequency-dependence of backscatter strength, as described before in the paragraphs about surface and volume scattering, can be utilized as additional discrimination of sediment composition or habitat structure and has shown the potential of improving seafloor classifications (Clarke, 2015; Costa, 2019; Gaida et al., 2018).

Chapters 2, 3 and 4 of this thesis present backscatter data recorded with multiple frequencies.

1.3.3 Seismics

Seismic methods are used for investigating the internal structure of the seafloor. Sediment profilers are designed similar to single-beam echosounders used for bathymetric mapping, but they operate at much lower frequencies to achieve larger penetration depths of up to hundreds of meters. They are a powerful to record sediment stratigraphy or finding buried objects of natural or anthropogenic origin. Seismic systems, consisting of a low-frequency source (e.g., airgun, boomer, sparker) and long receiving arrays called streamers, are able to investigate kilometer thick geological layers, which is used in the gas and oil exploration or for scientific purposes (Lurton, 2010). Especially elaborated 3D seismic cubes provide a detailed imaging of seafloor features and allow, e.g., the detection of fluid migration paths (Hustoft, Mienert, Bünz, & Nouzé, 2007), submarine mass movements (Karstens et al., 2019) or tectonic structures (Böttner et al., 2018).

The newly constructed 3D seismic lander (Section 1.4.2 and Chapter 5) for investigating the very shallow seafloor uses the same transducers for transmitting and receiving the acoustic signal comparable to sediment profilers. This simple geometry is possible due to the sounding at normal incidence to the sediment surface. Discontinuities in acoustic impedance generate reflections of the acoustic signal, while no backscattering is expected. At every interface, the acoustic signal is partly reflected towards the surface and partly transmitted deeper into the seafloor (Lurton, 2010).
The low attenuation of the used soft sediments and the low impedance contrast at the water-sediment interface allow a sufficient penetration even with the used high frequency of 130 kHz. The detection of buried objects is possible due to contrasts between the acoustic impedance of the objects and the surrounding sediment. The disturbance of the sediment by bioturbation creates heterogeneties within the sediment, e.g., water filled voids, which have a different acoustic impedance.

More details about seismic wave propagation can be found in Yilmaz (2001). The processing steps are described in Chapter 1.5. The 3D Stolt migration is based on Stolt (1978).

1.4 Methods

1.4.1 Multibeam Echosounder (MBES)

Development and Technical Possibilities of MBES

The active measurement of depth and obstacles using acoustics signals was developed in the 1920's after the sinking of the Titanic in 1912. First devices, the singlebeam echosounders (SBES), can measure the depth and intensity at a single spot at the seafloor below the ship. Additionally, echoes of targets in the water column can be detected, utilized, e.g., for fishing. Most SBES use the same transducer for transmitting and receiving and allow to switch between two frequencies in order to use the same system for different applications. Since the 1960's, sidescan sonars (SSS) are used to create acoustic images of the seafloor surface. SSSs are towed behind the ship close to the seafloor, thus they are stable in the water and mostly unaffected by waves or surface noise. They are equipped with two large antennas to the sides transmitting directed, horizontally very narrow beams. The signal is backscattered by the seafloor at grazing incidence and recorded against time. The small grazing angles increase the SSSs' sensitivity to obstacles at the seafloor surface. If objects are large, acoustic shadows are created, where no backscatter information can be received from, but object detection is enhanced. Each transmitted ping by the SSS results in a small, but up to several hundred meters wide, stripe of backscatter intensity, which are combined into a single map of the seafloor.

Multibeam echosounders (MBES) are in use since the 1970's. They combine and extend the two systems described above by being able to record bathymetric, backscatter intensity and water column data at once. MBESs consist of two transducer units, the transmitter and the receiver. Both are arranged perpendicular, the concept is called *Mill's Cross* array. Hereby, the transmission array emits an acoustic signal, which is narrow in the along-track direction. The perpendicular reception array records the returning signal with a narrow directivity in across-track direction. Thus, the backscattered signal can be allocated to a small area at the seafloor surface, the footprint, each recording representing one single beam. Modern MBESs can operate with average apertures of 60 to 75 and record a fan of several hundred separate beams after a ping with individual widths smaller than 1.
MBES systems are prone to wave movements as they are fixed to a boat or ship. Additional or integrated motion sensors are necessary to correct for the ships movements at sea.

Technical developments allow not only the recording of a single backscatter intensity per footprint, but a footprint time-series called *snippet* (Brown & Blondel, 2009). Hereby, intensity values for a certain time around the bottom detection are recorded for each beam of every ping. The across-track resolution can be improved. However, more storage space is needed when recording snippet data. Technically, also the recording of the entire water column data is possible, which can be of interest when investigating gas leakage (Schneider von Deimling, Brockhoff, & Greinert, 2007) or processes in the water column such as internal waves and turbulence (Colbo, Ross, Brown, & Weber, 2014), or the migration of zooplankton (Weinrebe, 2020). However, for studies focusing on seafloor habitats this option is only used for special purposes as it is producing enormous data volumes (several Terabyte per day depending on system settings).

MBES systems are often mainly used for depth measurements to develop bathymetric charts favorably utilizing higher frequencies to achieve a high resolution. The recording of backscatter data is often a by-product and therefore less in the focus of the MBES manu-

factures. However, recent developments allow the use of multiple frequencies with a single MBES system. Some can change the frequency with every ping, which is a requirement for a practical usage as the covered area is the same and going one-way is time-efficient. Commercial software is adapted to such multifrequency surveys and in later processing monofrequent maps can be created.

Calibration of MBES

A constant challenge when combining and comparing backscatter maps from cruises at different times and MBESs are the various backscatter levels, which can only be compared relative to each other. The solution to receive absolute backscatter values independent of sonar systems is the calibration of MBES. One calibration approach is the placement of a reference sphere in a large tank and rotating the sonar around to identify the sonar measurement characteristics to be able to compensate those. This method was applied for the 200 and 400 kHz frequencies of the Norbit iWMBS STX, which was used for the seasonally repeated measurements of the Hohe Düne area in Chapter 4. Another calibration strategy is, e.g., the use of a reference area of known backscatter, which must show stable conditions and be measured before with an alternative calibrated MBES (Lurton & Lamarche, 2015; Roche et al., 2018; Weber, Rice, & Smith, 2018).

Habitat Mapping with MBES

The considerable advantage of simultaneously recording bathymetry and backscatter strength made MBES the hydroacoustic method of choice within the international marine habitat mapping community (Lurton & Lamarche, 2015). Besides the permanently installed MBES on board of (research) vessels, smaller, transportable, but still powerful MBES are available. They can be utilized on board of small boats, which can sail the coastal areas, potentially including protected areas if equipped with an electric motor.

The accurate positioning of the device and subsequently of the beam geometry enables a precise measurement of the location of the footprint area and the incidence angle. This is a substantial advantage in case of the repetition of a survey for monitoring purposes or for identifying small-scale temporal changes (Chapter 4).

The possibility to change frequency, offered by many MBESs (some after every ping), allows for additional discrimination power of the backscatter maps. The frequency-dependent backscatter response of different habitats is presented in this thesis (Chapters 2, 3 and 4). For seafloor mapping sonars operate in the frequency range of ten to hundreds of kHz.

The introduction of snippets increased the backscatter concerning quality and resolution. The snippets cover the range of the acoustic path around the bottom detection, which coincides with the living space of the (epi-)benthic community. By combining beam time series extending above the bottom detection point and multifrequency acoustic waves with different penetration depths in soft sediments, MBES have a largely unexplored capability to survey the near seabed domain, meaning 1m around the seafloor surface.

Use of MBES in this Thesis

The data used in this thesis were recorded with a Norbit iWMBSe and a (partly calibrated) Norbit iWBMS STX, mounted to IOWs small catamaran Klaashahn, or the moonpool of RV Heincke or RV Elisabeth Mann Borgese (EMB) (Table 1.1).

Table 1.1: MBESs and frequencies used during this thesis.

	Chapter 2 (Sylt)	Chapter 3 (Oderbank)	Chapter 4 (Hohe Düne)
Vessel	RV Heincke	RV EMB	Klaashahn
Cruise	HE486	EMB188	(several)
Year of Survey	2017	2019	2019
MBES	Norbit iWMBSe	Norbit iWBMS STX	Norbit iWBMS STX
Frequencies [kHz]	200, 400, 600	200, 400, 550, 700	200, 400, 550, 700

1.4.2 3D Seismic Lander OWUHRSE

The 3D lander system used in Chapter 5 was developed within the pilot project SeaFloorScan (with the full German title *Erfassung und Darstellung von biogenen und geogenen Strukturen im und auf dem Meeresboden*). The aim was the acoustic imaging of small objects and structures on top of a (muddy) seafloor surface and within the first half a meter below. Investigations at the surface were conducted with cameras supported by LED lights for a uniform illumination and four lasers allowing a exact scaling of the photos.
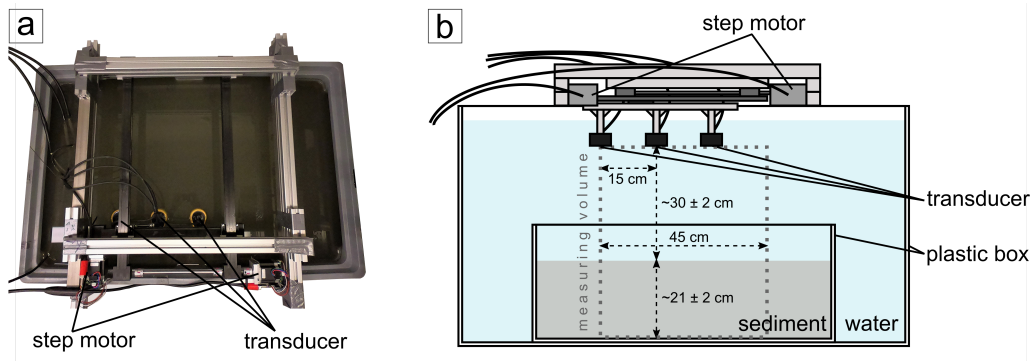

Figure 1.5: (a) Top-down photography of the test tank. The box filled with the substrate is not visible due to suspension in the water column. (b) The experimental setup consists of three transducers and two-step motors mounted on top of a water tank. The plastic box containing the buried test object is located 30 cm below the transducers and is filled with a 21 cm thick sediment layer (Schulze et al., 2021).

The 3D seismic lander for the imaging of the subsurface at a resolution of 1 cm was developed and build from scratch by IOW technician Gerald Nickel. Main components are three transducers mounted on an array, which can move in two directions powered by two step motors (Figure 1.5). The maximum penetration depth for the detection of biogenic structures is unknown and missing of physical parameters of biological structures prohibit significant modeling approaches. Therefore, transducers of different frequencies (70 kHz, 100 kHz, 120 kHz) were tested for penetration depth in muddy sediment. Finally, a frequency of 130 kHz was chosen for the acoustic signal. The sediment for laboratory experiments was retrieved in a Baltic Sea basin and sieved through a 2mm mesh, which turned out to be very time consuming due to the formation of a mud-water suspension. Initial laboratory experiments showed that the penetration depth was greater than expected and the maximum could not be determined due to size limits of the test set up. The seismic trace in SEGY format were mainly processed using code provided by Dennis Wilken (Christian-Albrechts-Universität zu Kiel) and functions from Seismic Unix (Stock-

well, 1999) and SegyMat (Mejer Hansen, 2019). For visualization, the 3D seismic volume was imported to the commercial software IHS Kingdom, commonly used by the oil and gas exploring industry.

The technical background of the 3D seismic lander, the conducted experiments as well as the seismic processing are explained in more detail in Chapter 5. For prospective plans involving the 3D seismic lander see Section 6.1.

1.5 Thesis Outline and Personal Contribution (Eigenanteil bei kumulativen Dissertationen)

This doctoral thesis consists of six chapters and an appendix. The first general chapter is introducing the dissertation topic and explaining the applied methods. Results from the finished articles and additional analysis of data set from Oder Bank (Baltic Sea) are presented and discussed, before concluding the thesis.

Chapter 2 presents the first article "**Improved Interpretation of Marine Sedimentary Environments Using Multi-Frequency Multibeam Backscatter Data**", which was published in 2018 (Feldens, Schulze, Papenmeier, Schönke, & Schneider von Deimling, 2018). According to the corresponding author, P. Feldens, all authors contributed equally to the manuscript (20% each). The doctoral candidate contributed to the formal analysis, investigation, methodology and writing the original draft. Furthermore, results were presented during a talk at the GeoHab conference 2018 in Santa Barbara, USA.

Chapter 3 presents an additional study "**Multifrequency Backscatter of Mussel Bands on Sand**" with results from a survey to Oder Bank (Baltic Sea). The methodology and data set was similar to Chapter 2, but the benthic target, mussel clusters, was different. The doctoral candidate contributed as first author to the methodology, software, formal analysis, investigation, visualization and writing. Results from this study were presented during a talk at the GeoHab conference 2019 in St. Petersburg, Russia.

Chapter 4 presents the second article "**Seasonal Change of Multifrequency Backscatter in three Baltic Sea Habitats**", which was submitted in 2022. The doctoral candidate contributed as first author to the conception and design of the study, the field work, data analysis, visualization and writing the first draft of the manuscript.

Chapter 5 presents the third article "**Laboratory Measurements to Image Endobenthos and Bioturbation with a High-Frequency 3D Seismic Lander**", which was published in 2021 (Schulze et al., 2021). The doctoral candidate contributed as first author to the methodology, software, formal analysis, investigation, visualization and writing the original draft.

Chapter 6 concludes this thesis with a short review including some challenges and an outlook.

Appendix A includes the Eigenständigkeitserklärung (Declaration of Originality) and the doctoral candidates CV with a publication list. Furthermore, information about the funding are supplemented, concluding with the acknowledgments in the very end.

Signature of the doctoral candidate

Signature of the supervisor

Paper I
Improved Interpretation of Marine Sedimentary Environments Using Multi-Frequency Multibeam Backscatter Data

Article

Improved Interpretation of Marine Sedimentary Environments Using Multi-Frequency Multibeam Backscatter Data

Peter Feldens [1,*]**, Inken Schulze** [1]**, Svenja Papenmeier** [2] **, Mischa Schönke** [1]
and Jens Schneider von Deimling [3]

[1] Marine Geology, Leibniz Institute for Baltic Sea Research Warnemünde, 18119 Rostock, Germany;
    inken.schulze@io-warnemuende.de (I.S.); mischa.schoenke@io-warnemuende.de (M.S.)
[2] Alfred Wegener Institute, Helmholtz Centre for Polar and Marine Research, Wadden Sea Research Station,
    25992 List/Sylt, Germany; svenja.papenmeier@awi.de
[3] Institute of Geosciences, Christian-Albrechts-Universität zu Kiel, 24118 Kiel, Germany;
    jens.schneider@ifg.uni-kiel.de
[*] Correspondence: peter.feldens@io-warnemuende.de

Abstract: Backscatter mosaics based on a multi-frequency multibeam echosounder survey in the continental shelf setting of the North Sea were compared. The uncalibrated backscatter data were recorded with frequencies of 200, 400 and 600 kHz. The results showed that the seafloor appears mostly featureless in acoustic backscatter mosaics derived from 600 kHz data. The same area surveyed with 200 kHz reveals numerous backscatter anomalies with diameters of 10–70 m deviating between −2 dB and +4 dB from the background sediment. Backscatter anomalies were further subdivided based on their frequency-specific texture and were attributed to bioturbation within the sediment and the presence of polychaetes on the seafloor. While low frequencies show the highest overall contrast between different seafloor types, a consideration of all frequencies permits an improved interpretation of subtle seafloor features.

Keywords: multibeam echosounder; backscatter; multi-frequency; benthic habitats; North Sea

1. Introduction

A reliable, repeatable and objective classification of seabeds, ultimately comprising both geological and biological habitats, continues to be an important issue for marine spatial planning and management as well as for research. Acoustic remote sensing by side scan sonar and multibeam echosounder obtains information on seafloor habitats based on measuring the intensity of acoustic signals backscattered from the seafloor [1,2]. The intensity of a backscattered signal depends on a number of geo-acoustic properties of the sediment surface and shallow subsurface, the water column, geometrical and technical parameters, and has been described by a number of physical and heuristic models [3–5]. The bulk backscattering level measured by the sonar comprises specular reflection, seafloor scatter and volume scatter and depends on the incidence angle and frequency of the acoustic wave. The angular dependence of backscatter levels has been used to characterize different seabeds [6,7]. A disadvantage of angular response curve (ARC)-based seafloor classification is their inherent half-swath width resolution (except for survey geometries with strongly overlapping survey lines) [8]. Therefore, ARCs are less sensitive to small-scale variations in seafloor composition and a strong synergy with backscatter mosaics corrected for the angular dependence exists, albeit this is rarely utilized [7]. A standard geological application utilizing backscatter data is the creation of sediment distribution maps [9]. In contrast to geological applications, the use of acoustic data for the delineation of biological

seafloor habitats has become more widespread only in the past years [1], although it is well-established in fisheries management [10,11].

Available studies involve surveys of cold water corals [12–14] and different benthic habitats and assemblages [15–22]. Remote sensing of benthic habitats remains a field of active research, which strongly benefits from the ongoing optimization of multibeam echosounder backscatter and the introduction of multi-frequency capabilities [23–25]. Also, based on stationary scatter experiments on the seafloor in the past [26,27], multiple frequencies have been considered as a means of improving backscatter mosaics [23]. Several of the parameters controlling backscatter are frequency dependent and the scattering itself is modulated by geological and biological inhomogeneities in the seabed. For example, seafloor roughness pertinent to acoustic scatter is defined relative to the wavelength of the acoustic source and different acoustic wavelengths are sensitive to different parts of the surface roughness power spectrum. In addition, the effects of volume scatter depend on the penetration depth of the acoustic signal into the subsurface and are generally more prominent with decreasing frequency [28].

Multi-frequency multibeam echosounder surveys are expected to improve backscatter mosaics [23] for geological and biological applications. Applications of multi-frequency datasets for seafloor surface characterization have been rare in the past, an early example being [29]. With the majority of all modern side scan sonars having a dual-frequency capacity, dual-frequency approaches were first developed for side scan sonar surveys. These studies found both distinct [30,31] and less-distinct [32] frequency dependences of marine sediments and acoustic scatter. Strong frequency dependence was reported from multibeam and single beam multi-frequency studies in regard to shallow gas surveying, taking advantage of frequency-dependent penetration depth and resonance effects [33,34]. In contrast, the frequency-dependent visibility of benthic habitats is not yet known. In this study, we show data from a multibeam echosounder survey in the North Sea recorded three times with different frequencies. With this comprehensive dataset, we showcase the possibilities and demonstrate the current limitations of using multi-frequency mosaics for the interpretation of small-scale benthic habitats in the North Sea.

2. Material and Methods

2.1. Regional Setting of the Study Area

The study site is located approx 15 km offshore the island Sylt (Figure 1) in the German Bight in water depths of 15–18 m, covering an area of 8 km^2. In the area, glacial sediments of the Saalian period were covered by Weichselian periglacial and Holocene fluvial deposits [35]. These deposits were reworked during the Holocene sea level rise, leaving a low relief seafloor topography mainly composed of marine sand [36,37]. The thickness of the uppermost layer of mobile sand deposits (potentially moved by tides and storm events) reaches 1–3 m [37]. Locally, east–west directed sorted bedforms (rippled scour depressions) composed of medium to coarse sand are observed, often exposing a transgressive layer of gravel and coarse sand present at the base of the marine sands [35,36]. Sorted bedforms in the study site have a length of ~350 m and depths of 1–2 m [36]. These bedforms can remain stable over decades, although their oscillating boundaries may be covered by fine sand for varying amounts of time [36,38,39]. Reefs of the polychaete *Lanice conchilega* are widespread in the study site but show a high seasonal and annual change in population density [22]. The tubes of *L. conchilega*, formed by cemented sediment grains and shell fragments, have a diameter of up to 0.5 cm, and protrude 1–4 cm above the seafloor by [40,41]. Aggregating in patches, these reefs can have high densities of thousands of individuals per m^2 and reach elevations of up to 20 cm [42].
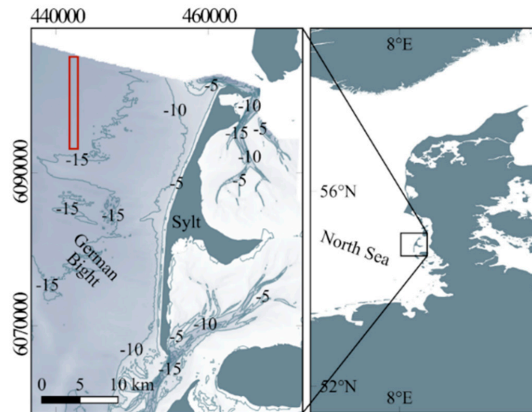
Figure 1. Location of the study site in the North Sea, marked with a red rectangle. Bathymetric data is derived from the BSH GeoSeaPortal (www.geoseaportal.de). Coordinates of the inset are in UTM32N WGS84.

2.2. Multibeam Echosounder

A Norbit iWBMSe multibeam echosounder mounted on the moonpool of FS Heincke was used together with an Applanix SurfMaster inertial navigation and attitude system. For the three surveys (recorded 13–16 May 2017), frequencies were set to 200, 400 and 600 kHz. EGNOS correction data were received to improve navigation to 0.5 m lateral accuracy. We registered backscatter strength using the Hypack 2016 software. Processing focused on removing the angular variations present in the data by applying an angular varied gain (AVG) and comparing relative backscatter levels between the frequencies [23]. No absolute dB values are given, as recommended by the authors of [25].

Except for frequency, the user-controllable settings of the multibeam system were kept constant and are shown in Table 1. System gains are largely removed from the multibeam output by the Norbit software (level BL_1). Residual effects may still be observed because the instruments are not individually calibrated. Pulse lengths and frequencies are constant throughout the swath with no sector dependence. Backscatter data were loaded in QPS Geocoder and corrected considering survey settings and frequency-dependent absorption (Table 1). For calculation of absorption coefficients [43], the temperature was estimated as 11° with salinity to 35. AVG to flatten the backscatter mosaics was calculated using a flat seafloor assumption, given that morphological differences across the study site are minor. AVGs were averaged for complete survey lines to avoid artifacts across boundaries of changing backscatter, accepting a less ideal removal of along-track artifacts. The average seafloor response within an incidence angle interval of 30° to 60° was used to normalize the data. Beam pattern effects were removed by applying the AVG. Backscatter intensities were linearly mapped to a greyscale mosaic with a resolution of 0.3 m. The dynamic range of the mosaics is 10 dB. Dark colors represent low backscatter intensities and bright colors represent high backscatter intensities. The final mosaics were filtered using a 3 × 3 box average filter. Multi-frequency mosaics were created by using three mono-frequency greyscale mosaics as input channels of an RGB image using open source GIS software (QGIS 2.18.9, www.qgis.org). The 200 kHz frequency represents the red channel, the 400 kHz frequency the green channel, and the 600 kHz frequency the blue channel.

Angular response curves (ARCs) supporting the mosaic interpretation were calculated directly from the recorded raw data files. The angular backscatter strength is [44]:

$$\overline{BS(\theta)} = EL(\theta) - SL + 2TL - 10log(\overline{A(\theta)}) \tag{1}$$

where *BS* is the angular backscatter strength, θ is the incidence angle, *EL* is the recorded echo level, *SL* is the (estimated) source level, *TL* is the transmission loss (spreading + absorption) and *A* is the ensonified

area. The calculation of the texture parameter entropy [45] supporting the mosaic interpretation was done using 32 grey levels, an inter-pixel distance of 1 and a window size of 4.5 m [46].

Table 1. Multibeam echosounder settings during data acquisition. Multiple values correspond to frequencies of 200, 400 and 600 kHz respectively. Source levels of the 200 and 600 kHz frequency are unknown.

Parameter	Value	Parameter	Value
Bandwidth chirp (kHz)	80	Spreading	0
Chirp pulse length (ms)	0.2	Absorption (dB/km)	0
Center frequency (kHz)	200/400/600	Static gain (dB)	0
Across track beam width at center frequency (°)	1.8/0.9/0.6	Along-track beam width at center frequency (°)	3.8/1.9/1.3
Absorption coefficient (dB/km)	60/100/170	Source level (dB re µPa)	-/227/-

2.3. Parametric Echosounder

Supporting high-frequency seismic data were acquired using an Innomar parametric sediment echosounder to determine the shallow subsurface geology, using primary frequencies of 100 kHz and a low frequency of 12 kHz. Data were binned to 1 m intervals, and a manual time varied gain function was applied.

2.4. Ground Truthing

Sediment samples for ground truthing were taken using a Van-Veen type grab sampler. The generally fine-grained sediment samples were analyzed by optical grain size analysis using a CILAS 1180 particle size analyzer. Given the well-sorted sand composition with low organic content, no chemical pretreatment was applied. The mode is used as a central statistical parameter, as it is less affected by the removal of particles exceeding 1 mm in diameter. For ground truthing by underwater video, we used a Kongsberg Colour Zoom Camera (Kongsberg Maritime, Kongsberg, Norway) and a GOPRO 3+ Black Edition (GoPro, San Mateo, CA, USA) both mounted on a steel frame that was towed behind the drifting research vessel.

3. Results

Several features in backscatter mosaics (Figure 2) are frequency dependent and are described in the following. The geologic framework of these features is observed in the seismic data that shows two seismic units forming the shallow subsurface of the study site (Figure 3). Seismic unit S1 is characterized by a chaotic and inhomogeneous appearance and outcrops in the area of sorted bedforms. S1 is interpreted as the onset of a coarse sand transgression layer reported to form the sorted bedforms. Sorted bedforms are clearly detectable by morphologic depressions of 0.2–1 m (Figure 3A) and a characteristic increase in backscatter intensities. Outside of the sorted bedforms, a transparent seismic unit S2 is present (Figure 3A,C). S2 is interpreted as the layer of mobile marine sediments. Its thickness across the study site varies between 0 and approx. 1 m. The minimum thickness is observed within sorted bedforms, and a decreased thickness prevails in the central study site (Figure 3B). Outside of sorted bedforms, results of the grain size distribution suggest a homogeneous, flat seafloor composed of well-sorted fine sand with a mode around 2.5 phi (Figure 4). However, various small-scale backscatter anomalies exist. Fringing the sorted bedforms, 200 kHz data shows rims of decreased backscatter intensity aligning preferably along their northwestern edges (Figure 2A). The decrease in backscatter intensities is poorly observed in 400 kHz data, and disappears for the 600 kHz mosaic, causing a bluish north-western rim adjacent to sorted bedforms in the multi-frequency mosaic (Figure 2A).

Clearly standing out from a homogeneous background, numerous patches of increased backscatter levels (high backscatter patches, HBPs) are visually delineated. HBPs cannot be observed in

bathymetric data, suggesting that the depth difference between the patches and the surrounding seafloor is less than 5 cm. In the northern part of the study site, HBPs have an irregular shape and a random distribution pattern. Their diameter is 10–25 m. In the 200 kHz mosaics, the HBPs show increased (~4 dB) backscatter intensities compared to the background sediment. The increase in intensities is reduced in the 400 kHz data (~2 dB) and hardly observed in the 600 kHz data. This results in a distinct reddish appearance of the HBP in the multi-frequency data. An increase of the silt fraction percentage is observed for sample HE486-14 retrieved from an area of densely spaced HBPs, and a poorly developed ripple pattern is recognized in nearby underwater video footage (Figure 5). An increased number of polychaetes identified as *L. conchilega* were observed in grab samples and underwater video images in the northern part of the investigation area, although overall observed population densities are low (Figure 5).
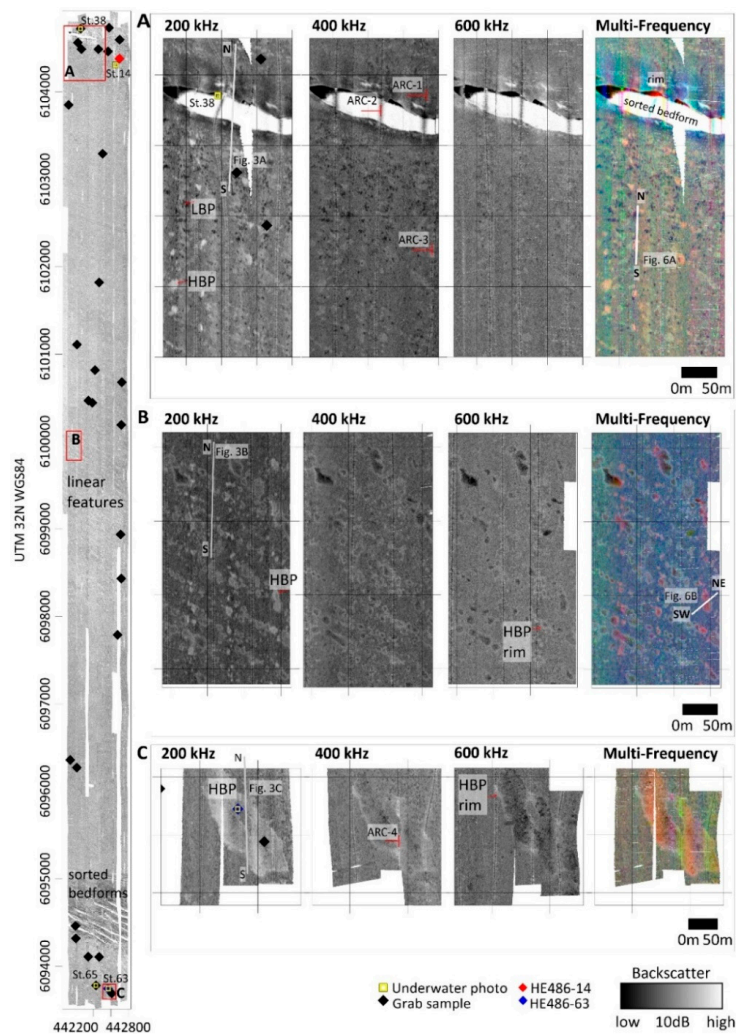

Figure 2. Backscatter data recorded in the study site. The overview image to the left shows the available data and position of the insets (**A**–**C**). The overview mosaic was contrast-stretched. Insets (**A**), (**B**) and (**C**) show mosaics of 200, 400 and 600 kHz and an RGB multi-frequency mosaic for selected areas. Examples of high backscatter patches (HBP) and low backscatter patches (LBP) are annotated. The position of seismic lines (Figure 3), grab samples (Figure 4), underwater video (Figure 5), cross sections through the multi-frequency mosaic (Figure 6), and angular response curves (ARC, Figure 7) is indicated.
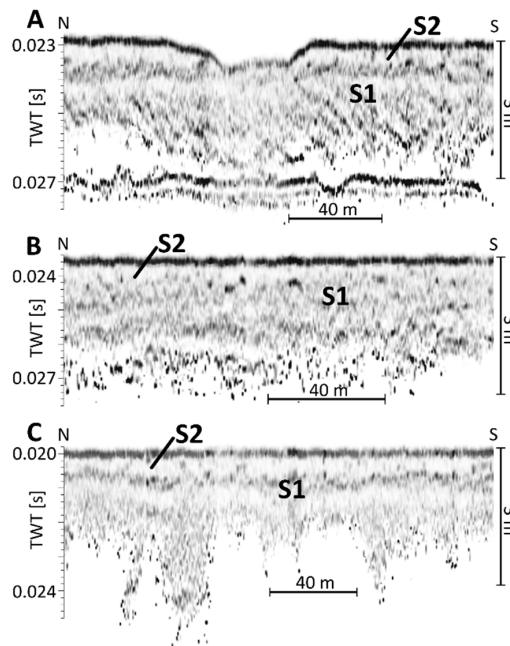
Figure 3. Seismic data reveals the geological structure of the shallow subsurface in the northern (**A**), central (**B**) and southern part (**C**) of the investigated area. A transparent layer composed of fine sand (S2) is observed above a coarse sand transgression layer (S1). Refer to Figure 2 for position of the seismic lines.
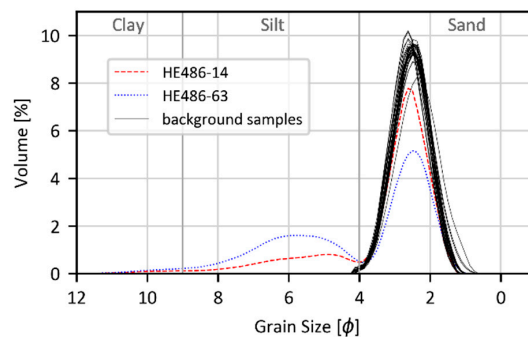

Figure 4. Grain size composition in the study site. The majority of the samples have a well-sorted fine sand composition. The position of two samples with increased silt content is marked in Figure 2.

The shape of the HBP changes towards the south of the study site. In the central part of the study site, HBPs are aligned NW-SE parallel to the observed sorted bedforms (Figure 2). The length of the HBP differs between 5 and 70 m, while their width is approx. constant at 15 m. An intensity profile crossing an HBP (Figure 6B) reveals increased backscatter levels (~2 dB) for the low frequency. The rims of the HBPs have elevated backscatter intensities, especially in the high frequency. However, an intensity decrease to background levels or below can be observed for the inner part of the HBPs mostly at high, but sometimes also at low frequencies (Figure 2B,C). In the multi-frequency data, the HBPs have a reddish center, with bluish-greenish fringes. An example HBP with a size of ~0.013 km^2 showcasing this behavior exists in the south (Figure 2C). It shows the highest backscatter intensities for the 200 kHz frequency (an increase of about 2 dB), and a reverse sensitivity with decreased backscatter intensities for the 600 kHz frequency. In the 400 kHz mosaic, only the

boundaries of the HBP are recognized, while its central area is difficult to distinguish from the surrounding background sediment. Here, sample HE486-63 revealed an increased amount of silt and clay. Underwater video footage shows a weakly developed ripple pattern, black anoxic sediment directly beneath the surface and increased suspension. In contrast, video footage outside the high backscatter patch shows a distinct rippled seafloor (Figure 5).
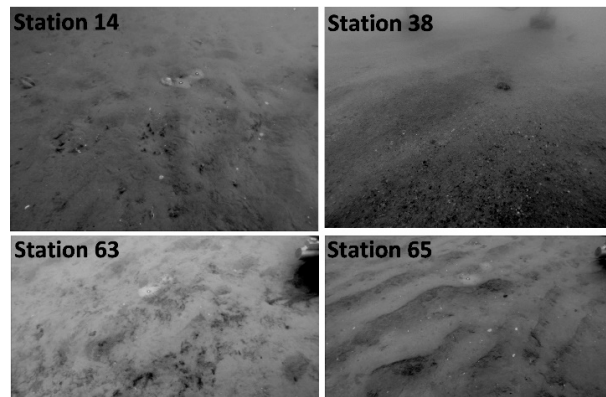

Figure 5. Underwater video footage from the northern study site (station 14) shows small numbers of *L. conchilega* tubeworms. In contrast, station 38 at the boundary of a sorted bedform comprises rippled coarse sand. In the south, station 63 shows different benthic assemblages in the center of a high backscatter patch. Outside of the patch, a clear ripple pattern prevails (station 65). Refer to Figure 2 for positions.
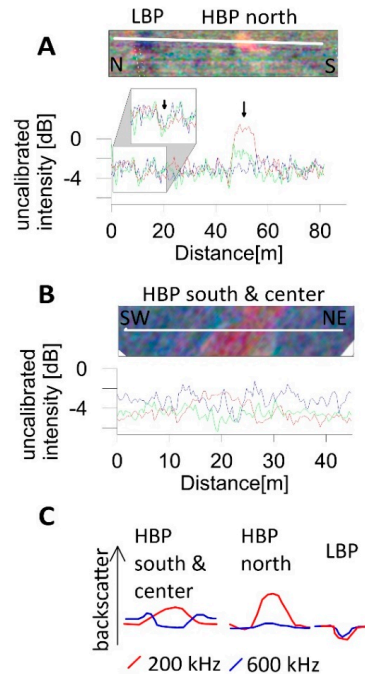

Figure 6. The cross sections (**A**) and (**B**) through the multi-frequency mosaic showcase the frequency-dependent response of high backscatter patches (HBP) and low backscatter patches (LBP). Refer to Figure 2 for the position of the cross sections. (**C**) displays the schematic of the different observed backscatter anomalies.

Smaller patches of decreased backscatter levels (low backscatter patches, LBP) can be recognized in the northern study site. For LBP, backscatter levels decrease below the background fine sand intensity for all frequencies. No rim effects can be recognized. The diameter of LBP is generally smaller than 10 m. LBPs are best observed in the 200 and 400 kHz data, where the difference to the surrounding seafloor is largest (~1.5 dB). LBPs are barely visible in the 600 kHz mosaic (Figure 2), causing a dark bluish appearance in the multi-frequency mosaic.

4. Discussion

4.1. Impact of Volume Scatter

Our multi-frequency seafloor analyses show clear evidence for significantly different backscattering strengths and image textures at specific frequencies. Principally, the low frequency mosaics show the highest contrast between different seafloor facies (Figure 2), a trend that was previously noted [23]. The frequency-specific backscatter differences could be of geological or biological origin. An example of a geological cause is the increase in high-frequency scatter intensity north of the sorted bedforms. Adjacent to the sorted bedforms, oscillating boundaries to the surrounding seafloor exist, indicating the presence of a mobile fine sand layer. It is redeposited on sub-annual timescales [36] and reduces the number of scatterers in the shallow subsurface. No HBP or LBP patches are present directly at the rim in any frequency (Figure 2A), supporting a homogenous fine sand seafloor that registers with stronger backscatter intensities at higher frequencies and decreased intensities at low frequencies. Comparable trends have been previously observed in side scan sonar [31] and multibeam data [29] for sediments of low volume scatter that allow penetration of the low, but not the high frequency [30]. For sandy sediments, penetration depth is limited to ~1 cm for 600 kHz, while 200 kHz may penetrate ~8 cm into the subsurface [47].

A geologic or biologic cause of the elongated HBP in the central part of the investigation area is more difficult to establish. The HBPs may be interpreted as buried sorted bedforms covered by a thin layer of fine sand. Temporarily or completely buried sorted bedforms have been reported elsewhere [35,38]. Elevated backscatter levels are chiefly observed in the low frequency mosaics, where acoustic waves penetrated a couple of centimeters into the subsurface. A connection to sorted bedforms that could influence volume scatter by sub-bottom layering [48] is possible based on the seismic data (Figure 3B). The transparent layer (S1), interpreted as the mobile layer of fine sand [37], is of decreased thickness in the area of elongated HBPs. This indicates a thin cover of fine sand on the coarser transgressive sand layer. However, a number of factors are in contradiction to the HBP being caused by partially buried sorted bedforms. First, there is no indication of any residual depression of HBP in seismic or bathymetric data, while the active sorted bedforms in the north and south are clearly recognized by their bathymetry. Second, no coarse sand was recovered at the top or base of the grab samples taken in their vicinity, albeit Van-Veen grab samples typically recover several centimeters of sediment. Finally, angular response curves (ARCs) of the 200 kHz data (Figure 7) from the sorted bedform in the north, a mostly featureless area composed of fine sand, and different HBPs, indicate clear differences between sorted bedforms and the remaining seafloor facies. Therefore, the HBP is less likely to be of geological origin. It cannot be ruled out that geological changes in the shallow subsurface (below a few centimeters), while not significantly affecting the acoustic backscatter, impact the benthic biology of the seafloor, thus explaining the similarity in orientation between HBPs and sorted bedforms. Nevertheless, an increase in volume scatter caused by bioturbation and organic scatterers in the shallow subsurface is the most likely cause of the increased backscatter strength of the HBP at low frequencies [49]. Volume scatter is especially prevalent in silty facies [50] due to a generally decreased acoustic impedance, and generally induced by biological activity [51]. Higher frequencies capture the fine, partially silty seafloor without notable ripple features, causing a decreased backscatter intensity [30]. Under the assumption that the rims of the sorted bedforms are composed of frequently redeposited, homogeneous fine sand, ARCs (Figure 7) confirm volume scatter in the area of HBPs at

incidence angles >~20°, apparent by increased scatter intensities for the 200 kHz data. No indications of volume scatter are observed in ARCs for the 600 kHz dataset. While volume scatter appears most prominent in the extended southern HBP, where an increased silt fraction is observed (ARC 4 in Figure 7), the extent of almost all HBPs is smaller than a half-swath width, which negatively affects the ability of ARCs to differentiate seafloor types. Therefore, the combined use of ARCs and multi-frequency mosaics may allow differences in volume scatter to be traced, for example, caused by the different presence of burrowing organisms and scatterers, over small scales.
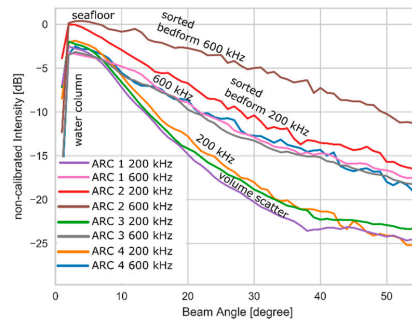

Figure 7. Angular response curves at the rim (ARC 1) and within (ARC 2) a sorted bedform, in the area of densely spaced HBP (ARC 3) in the northern study site and across a large HBP in the southern study site (ARC 4). The shape of the ARC within a sorted bedform differs clearly from all other sediments. Indications of volume scatter at >20° incidence angle are only observed in the 200 kHz dataset. Refer to Figure 2 for position.

4.2. Impact of Seafloor Scatter

The comparison of backscatter mosaics of different frequencies shows textural differences between HBPs in the southern/central and northern area of the study site, including the lack of a rim, the missing backscatter level inversion between high and low frequencies and a stronger and more rapid increase in backscatter levels (~4 dB in the northern versus ~2 dB in the central area). These differences could not have been observed using mono-frequency mosaics. The higher increase in backscatter levels, missing frequency inversion and comparable ARCs between HBPs in the central and northern study site indicate that volume scatter effects are not the only cause of the northern HBPs. Based on the assumption of a biologic cause of the HBPs, the tube-building species, polychaete *L. conchilega* is the most likely cause as it is a widespread key species in the North Sea [52] which was frequently observed in video images of the northern part of the investigation area (Figure 5), and it increases seafloor scatter [18,22]. Similar roughness-impacting organisms such as brittle star *Amphiura filiformis* that may reach high population densities and affect acoustic scatter [53] were not observed in high densities during the ground truthing. In the present bathymetric data, no morphology of the patches is detectable. Therefore, elevation differences in the surrounding seafloor are less than 5 cm. Since data collection took place in the beginning of May, the development of the worm aggregation after deconstruction during the winter [54] was probably in an early stage with a small number of adult individuals that are not expressed in ship-based bathymetric data. While video footage confirms the low densities of tubeworms, low population densities were found to significantly impact seafloor roughness at specific spatial wavelengths [55] and can be detected in backscatter data [16,22]. The fact that the northern HBP patches are best observed at 200 kHz is in contrast to previous findings [18] where a 445 kHz frequency was more effective than 132 kHz for the detection of *L. conchilega* reefs. The differences might arise due to the use of different acoustic systems (multibeam and side-scan sonar) with different footprints and pulse widths, or seasonal differences in the frequency-dependence of the backscatter strength of *L. conchilega* due to changing population densities. This needs to be further explored. In general, the largest impact of *L. conchilega* on seafloor roughness was found at spatial wavelengths of

~0.5 to 2 cm [55], where sparse *L. conchilega* populations increase the magnitude of seafloor roughness by up to 4 dBm[4]. Applying the small perturbation approximation to estimate backscatter strengths, the roughness spectrum used for the calculation of the backscatter cross section is evaluated at the Bragg wavenumber $2ksin(\theta)$, where k is the acoustic wavenumber and θ the incidence angle [28]. For an incidence angle of 45°, the spatial wavelengths at the Bragg wavenumber vary between 0.5 cm for 200 kHz and 0.2 cm for 600 kHz. The agreement of optical measurements of *L. conchilega* seafloor roughness and the frequency-dependent appearance of the northern HBP suggests that backscatter strength may be higher for lower frequencies due to changes in surface roughness caused by benthic organisms. Eventually, frequencies less than 200 kHz that were not accessible to our system would be more sensitive to tubeworm presence. Therefore, a frequency-dependent acoustic scatter may be exploited by multi-frequency surveys for benthic habitat mapping, with roughness controlled by reef density, local sediment composition, or even life cycle [21,22].

No sufficient interpretation is possible for a number of features observed in the backscatter mosaics. Several explanations are possible for the high backscatter rims observed at the boundaries of the HBP especially at higher frequencies, including either an increased surface roughness or increased presence of scatterers directly beneath the surface. However, due to the small extent of these features, a ground truthing or a detailed analysis using ARC was not possible. Similarly, the origin of the LBP observed in the northern part of the study site (Figure 2A) remains uncertain. Here, backscatter intensities decrease with increasing frequency, but are not in agreement with backscatter intensities observed for fine sand (Figure 2A, rim of the sorted bedform) or silty sediment compositions (Figure 2C). Possible explanations involve a local decrease in surface roughness (for example, due to changing grain size composition), causing locally smooth seafloor [30] combined with decreased volume scatter. However, the small extent and unsuccessful ground truthing of the LBP does not allow for a comprehensive interpretation.

4.3. Impact on Haralick Texture Parameters

Texture parameters derived from mosaics of backscatter intensity are common features for supervised or unsupervised seabed classification [56]. The acoustic frequency affects the texture parameters due to both changing survey parameters, such as footprint sizes (Table 1), but also due to the different sensitivity to seafloor features. Texture parameters derived from the backscatter mosaics in the northern part of the study site show that the different sensitivity of the mono-frequency mosaics to seafloor features carries over to derived textural parameters. Maps of seafloor entropy (Figure 8), a parameter that is closely correlated with homogeneity and contrast in sedimentary facies [46], demonstrate that the increased density of HBP and LBP in the northern part of the study site is best captured at low and medium frequencies, supporting the sensitivity of texture parameters to the presence of benthic organisms [22].
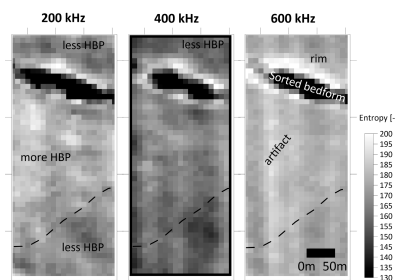

Figure 8. Texture parameter entropy for the northern region of the study site, corresponding to Figure 2A. It can be observed that the boundary between the density of less and more high backscatter patches (HBP) is more clearly observed in the 200 kHz data, while the boundary fringing the sorted bedforms is better observed in 600 kHz data. The presence of along-track artifacts is amplified in the texture images.

5. Conclusions

For sediment classification including the recognition of benthic habitats, backscatter data of lower frequencies (200 kHz) showed an increased sensitivity to changes in seafloor composition in a sedimentary continental shelf setting. It is suggested that low frequencies be incorporated in mapping programs utilizing backscatter information. The consideration of multiple frequencies allowed an improved interpretation of subtle seafloor features, although the limited availability of calibrated multi-frequency multibeam echosounders hindered quantitative data interpretation. The application of multi-frequency mosaics is especially promising for the detection of benthic life, which may vary over scales not accessible to interpretation by backscatter angular response curves or routine ground truthing. Introducing multispectral data increases data dimensionality, and may lend itself to automated seafloor classification. However, our results show that for practical application of multi-frequency data for habitat mapping, we lack the information to interpret many backscatter features of the seafloor. Therefore, the concurrent recording of calibrated multi-frequency backscatter data and precisely positioned geological and biological ground truthing, including the shallow subsurface, are required to establish interrelationships and fully utilize the potential of modern multibeam echosounders in the future.

References

1. Anderson, J.T.; Van Holliday, D.; Kloser, R.; Reid, D.G.; Simard, Y. Acoustic seabed classification: Current practice and future directions. *ICES J. Mar. Sci.* **2008**, *65*, 1004–1011. [CrossRef]
2. Brown, C.J.; Blondel, P. Developments in the application of multibeam sonar backscatter for seafloor habitat mapping. *Appl. Acoust.* **2009**, *70*, 1242–1247. [CrossRef]
3. Jackson, D.R.; Winebrenner, D.P.; Ishimaru, A. Application of the composite roughness model to high-frequency bottom backscattering. *J. Acoust. Soc. Am.* **1986**, *79*, 1410–1422. [CrossRef]
4. Lamarche, G.; Lurton, X.; Verdier, A.-L.; Augustin, J.-M. Quantitative characterisation of seafloor substrate and bedforms using advanced processing of multibeam backscatter—Application to Cook Strait, New Zealand. *Cont. Shelf Res.* **2011**, *31*, S93–S109. [CrossRef]
5. Yu, J.; Henrys, S.A.; Brown, C.; Marsh, I.; Duffy, G. A combined boundary integral and Lambert's Law method for modelling multibeam backscatter data from the seafloor. *Cont. Shelf Res.* **2015**, *103*, 60–69. [CrossRef]
6. Sternlicht, D.D.; de Moustier, C.P. Time-dependent seafloor acoustic backscatter (10–100 kHz). *J. Acoust. Soc. Am.* **2003**, *114*, 2709–2725. [CrossRef] [PubMed]
7. Fonseca, L.; Brown, C.; Calder, B.; Mayer, L.; Rzhanov, Y. Angular range analysis of acoustic themes from Stanton Banks Ireland: A link between visual interpretation and multibeam echosounder angular signatures. *Appl. Acoust.* **2009**, *70*, 1298–1304. [CrossRef]
8. Rzhanov, Y.; Fonseca, L.; Mayer, L. Construction of seafloor thematic maps from multibeam acoustic backscatter angular response data. *Comput. Geosci. J.* **2012**, *41*, 181–187. [CrossRef]
9. Stephens, D.; Diesing, M. Towards quantitative spatial models of seabed sediment composition. *PLoS ONE* **2015**, *10*, e0142502. [CrossRef] [PubMed]

10. Foote, K.G.; Aglen, A.; Nakken, O. Measurement of fish target strength with a split-beam echo sounder. *J. Acoust. Soc. Am.* **1986**, *80*, 612–621. [CrossRef]

11. Hashim, M.; Aziz, M.F.; Hassan, R.B.; Hossain, M.S. Assessing target strength, abundance, and biomass for three commercial pelagic fish species along the East coast of Peninsular Malaysia using a Split-Beam echo sounder. *J. Coast. Res.* **2017**, *33*, 1448–1459. [CrossRef]

12. Roberts, J.M.; Brown, C.J.; Long, D.; Bates, C.R. Acoustic mapping using a multibeam echosounder reveals cold-water coral reefs and surrounding habitats. *Coral Reefs* **2005**, *24*, 654–669. [CrossRef]

13. Huehnerbach, V.; Blondel, P.; Huvenne, V.; Freiwald, A. Habitat mapping on a deep-water coral reef off Norway, with a comparison of visual and computer-assisted sonar imagery interpretation. In *Mapping the Seafloor for Habitat Characterization*; Todd, B., Greene, G., Eds.; Geological Association of Canada: St. John's, NL, Canada, 2007; p. 12.

14. Glogowski, S.; Dullo, W.-C.; Feldens, P.; Liebetrau, V.; von Reumont, J.; Hühnerbach, V.; Krastel, S.; Wynn, R.B.; Flögel, S. The Eugen Seibold coral mounds offshore western Morocco: Oceanographic and bathymetric boundary conditions of a newly discovered cold-water coral province. *Geo-Mar. Lett.* **2015**, *35*, 257–269. [CrossRef]

15. Kostylev, V.; Todd, B.; Fader, G.; Courtney, R.; Cameron, G.; Pickrill, R. Benthic habitat mapping on the Scotian Shelf based on multibeam bathymetry, surficial geology and sea floor photographs. *Mar. Ecol. Prog. Ser.* **2001**, *219*, 121–137. [CrossRef]

16. Self, R.F.L.; A'Hearn, P.; Jumars, P.A.; Jackson, D.R.; Richardson, M.D.; Briggs, K.B. Effects of macrofauna on acoustic backscatter from the seabed: Field manipulations in West Sound, Orcas Island, Washington, U.S.A. *J. Mar. Res.* **2001**, *59*, 991–1020. [CrossRef]

17. Brown, C.; Hewer, A.; Limpenny, D.; Cooper, K.; Rees, H.; Meadows, W. Mapping seabed biotopes using sidescan sonar in regions of heterogeneous substrata: Case study east of the Isle of Wight, English Channel. *Underw. Technol. Int. J. Soc. Underw.* **2004**, *26*, 27–36. [CrossRef]

18. Degraer, S.; Moerkerke, G.; Rabaut, M.; Van Hoey, G.; Du Four, I.; Vincx, M.; Henriet, J.-P.; Van Lancker, V. Very-high resolution side-scan sonar mapping of biogenic reefs of the tube-worm *Lanice conchilega*. *Remote Sens. Environ.* **2008**, *112*, 3323–3328. [CrossRef]

19. McGonigle, C.; Brown, C.; Quinn, R.; Grabowski, J. Evaluation of image-based multibeam sonar backscatter classification for benthic habitat discrimination and mapping at Stanton Banks, UK. *Estuar. Coast. Shelf Sci.* **2009**, *81*, 423–437. [CrossRef]

20. De Falco, G.; Tonielli, R.; Di Martino, G.; Innangi, S.; Simeone, S.; Michael Parnum, I. Relationships between multibeam backscatter, sediment grain size and *Posidonia oceanica* seagrass distribution. *Cont. Shelf Res.* **2010**, *30*, 1941–1950. [CrossRef]

21. Raineault, N.; Trembanis, A.C.; Miller, D.C. Mapping benthic habitats in Delaware Bay and the coastal Atlantic: acoustic techniques provide greater coverage and high resolution in complex, shallow-water environments. *Estuar. Coasts* **2012**, *35*, 682–699. [CrossRef]

22. Heinrich, C.; Feldens, P.; Schwarzer, K. Highly dynamic biological seabed alterations revealed by side scan sonar tracking of *Lanice conchilega* beds offshore the island of Sylt (German Bight). *Geo-Mar. Lett.* **2017**, *37*, 289–303. [CrossRef]

23. Clarke, J.E.H. Multispectral acoustic backscatter from Multibeam, improved classification potential. In Proceedings of the United States Hydrographic Conference, San Diego, CA, USA, 15–19 March 2015.

24. Tamsett, D.; McIlvenny, J.; Watts, A. Colour sonar: Multi-frequency sidescan sonar images of the seabed in the Inner Sound of the Pentland Firth, Scotland. *J. Mar. Sci. Eng.* **2016**, *4*, 26. [CrossRef]

25. Lamarche, G.; Lurton, X. Recommendations for improved and coherent acquisition and processing of backscatter data from seafloor-mapping sonars. *Mar. Geophys. Res.* **2017**. [CrossRef]

26. Williams, K.L.; Jackson, D.R.; Thorsos, E.I.; Tang, D.; Schock, S.G. Comparison of sound speed and attenuation measured in a sandy sediment to predictions based on the Biot theory of porous media. *IEEE J. Ocean. Eng.* **2002**, *27*, 413–428. [CrossRef]

27. Williams, K.L.; Jackson, D.R.; Tang, D.; Briggs, K.B.; Thorsos, E.I. Acoustic backscattering from a sand and a sand/mud environment: Experiments and data/model comparisons. *IEEE J. Ocean. Eng.* **2009**, *34*, 388–398. [CrossRef]

28. Lamarche, G.; Lurton, X. Backscatter Measurements by Seafloor-Mapping Sonars. Guidelines and Recommendations. Available online: http://geohab.org/wp-content/uploads/2013/02/BWSG-REPORT-MAY2015.pdf (accessed on 11 June 2018).

29. Clarke, J.E.H.; Iwanowska, K.K.; Parrott, R.; Duffy, G.; Lamplugh, M.; Griffin, J. Inter-calibrating multi-source, multi-platform backscatter data sets to assist in compiling regional sediment type maps: Bay of Fundy. In Proceedings of the Joint Canadian Hydrographic and National Surveyors' Conference, Victoria, Australia, 26–29 March 2008; pp. 1–22.

30. Ryan, W.B.F.; Flood, R.D. Side-looking sonar backscatter response at dual frequencies. *Mar. Geophys. Res.* **1996**, *18*, 689–705. [CrossRef]

31. Tauber, F. Search for paleo-landscapes in the southwestern Baltic Sea with sidescan sonar. *Ber. RGK* **2011**, *92*, 323–349.

32. Collier, J.S.; Brown, C.J. Correlation of sidescan backscatter with grain size distribution of surficial seabed sediments. *Mar. Geol.* **2005**, *214*, 431–449. [CrossRef]

33. Klaucke, I.; Weinrebe, W.; Petersen, C.J.; Bowden, D. Temporal variability of gas seeps offshore New Zealand: Multi-frequency geoacoustic imaging of the Wairarapa area, Hikurangi margin. *Mar. Geol.* **2010**, *272*, 49–58. [CrossRef]

34. Schneider von Deimling, J.; Weinrebe, W.; Tóth, Z.; Fossing, H.; Endler, R.; Rehder, G.; Spieß, V. A low frequency multibeam assessment: Spatial mapping of shallow gas by enhanced penetration and angular response anomaly. *Mar. Pet. Geol.* **2013**, *44*, 217–222. [CrossRef]

35. Diesing, M.; Kubicki, A.; Winter, C.; Schwarzer, K. Decadal scale stability of sorted bedforms, German Bight, southeastern North Sea. *Cont. Shelf Res.* **2006**, *26*, 902–916. [CrossRef]

36. Mielck, F.; Holler, P.; Bürk, D.; Hass, H.C. Interannual variability of sorted bedforms in the coastal German Bight (SE North Sea). *Cont. Shelf Res.* **2015**, *111*, 31–41. [CrossRef]

37. Zeiler, M.; Schulz-Ohlberg, J.; Figge, K. Mobile sand deposits and shoreface sediment dynamics in the inner German Bight (North Sea). *Mar. Geol.* **2000**, *170*, 363–380. [CrossRef]

38. Thieler, E.R.; Pilkey, O.H.; Cleary, W.J.; Schwab, W.C. Modern sedimentation on the shoreface and inner continental shelf at Wrightsville Beach, North Carolina, USA. *J. Sediment. Res.* **2001**, *71*, 958–970. [CrossRef]

39. Murray, A.B.; Thieler, E.R. A new hypothesis and exploratory model for the formation of large-scale inner-shelf sediment sorting and "rippled scour depressions". *Cont. Shelf Res.* **2004**, *24*, 295–315. [CrossRef]

40. Ziegelmeier, E. Beobachtungen über den Röhrenbau von *Lanice conchilega* (Pallas) im Experiment und am natürlichen Standort. *Helgolander Wiss. Meeresunters* **1952**, *4*, 107–129. [CrossRef]

41. Callaway, R. Juveniles stick to adults: Recruitment of the tube-dwelling polychaete *Lanice conchilega* (Pallas, 1766). *Hydrobiologia* **2003**, *503*, 121–130. [CrossRef]

42. Rabaut, M.; Vincx, M.; Degraer, S. Do *Lanice conchilega* (sandmason) aggregations classify as reefs? Quantifying habitat modifying effects. *Helgol. Mar. Res.* **2009**, *63*, 37–46. [CrossRef]

43. Ainslie, M.A.; McColm, J.G. A simplified formula for viscous and chemical absorption in sea water. *J. Acoust. Soc. Am.* **1998**, *103*, 1671–1672. [CrossRef]

44. Hellequin, L.; Boucher, J.M.; Lurton, X. Processing of high-frequency multibeam echo sounder data for seafloor characterization. *IEEE J. Ocean. Eng.* **2003**, *28*, 78–89. [CrossRef]

45. Haralick, R.M.; Shanmugam, K.; Dinstein, I. Textural Features for Image Classification. *IEEE Trans. Syst. Man Cybern.* **1973**, *6*, 610–621. [CrossRef]

46. Feldens, P. Sensitivity of texture parameters to acoustic incidence angle in multibeam backscatter. *IEEE Geosci. Remote Sens. Lett.* **2017**, *14*, 2215–2219. [CrossRef]

47. Huff, L.C. Acoustic Remote Sensing as a Tool for Habitat Mapping in Alaska Waters. In *Marine Habitat Mapping Technology for Alaska*; Reynolds, J.R., Greene, H.G., Eds.; Alaska Sea Grant, University of Alaska Fairbanks: Fairbanks, AK, USA, 2008; pp. 29–46.

48. Schneider von Deimling, J.; Held, P.; Feldens, P.; Wilken, D. Effects of using inclined parametric echosounding on sub-bottom acoustic imaging and advances in buried object detection. *Geo-Mar. Lett.* **2016**, *36*, 113–119. [CrossRef]

49. Urgeles, R.; Locat, J.; Schmitt, T.; Hughes Clarke, J.E. The July 1996 flood deposit in the Saguenay Fjord, Quebec, Canada: Implications for sources of spatial and temporal backscatter variations. *Mar. Geol.* **2002**, *184*, 41–60. [CrossRef]

50. Jackson, D.R.; Briggs, K.B. High-frequency bottom backscattering: Roughness versus sediment volume scattering. *J. Acoust. Soc. Am.* **1992**, *92*, 962–977. [CrossRef]

51. Jensen, F.B.; Kuperman, W.A.; Porter, M.B.; Schmidt, H. *Computational Ocean Acoustics*; Springer Science & Business Media: Berlin, Germany, 2011; ISBN 9781441986788.

52. Van Hoey, G.; Guilini, K.; Rabaut, M.; Vincx, M.; Degraer, S. Ecological implications of the presence of the tube-building polychaete *Lanice conchilega* on soft-bottom benthic ecosystems. *Mar. Biol.* **2008**, *154*, 1009–1019. [CrossRef]

53. Hass, H.C.; Mielck, F.; Fiorentino, D.; Papenmeier, S.; Holler, P.; Bartholomä, A. Seafloor monitoring west of Helgoland (German Bight, North Sea) using the acoustic ground discrimination system RoxAnn. *Geo-Mar. Lett.* **2017**, *37*, 125–136. [CrossRef]

54. Carey, D. Sedimentological effects and palaeoecological implications of the tube-building polychaete *Lanice conchilega* Pallas. *Sedimentology* **1987**, *34*, 49–66. [CrossRef]

55. Schönke, M.; Feldens, P.; Wilken, D.; Papenmeier, S.; Heinrich, C.; Schneider von Deimling, J.; Held, P.; Krastel, S. Impact of *Lanice conchilega* on seafloor microtopography off the island of Sylt (German Bight, SE North Sea). *Geo-Mar. Lett.* **2017**, *37*, 305–318. [CrossRef]

56. Blondel, P.; Gómez Sichi, O. Textural analyses of multibeam sonar imagery from Stanton Banks, Northern Ireland continental shelf. *Appl. Acoust.* **2009**, *70*, 1288–1297. [CrossRef]

Chapter 3

Study
Multifrequency Backscatter of Mussel Bands on Sand

Foreword

The acoustic characteristics of mussel beds were found of particular interest during the Hohe Düne field work, and also during fieldwork of the ATLAS project (dealing with large-scale habitat mapping in coastal waters of Mecklenburg-Pomerania) project at IOW. The study reported in this chapter is based in a different location, but applied methods and processing are very similar to the paper in Chapter 2 and are not repeated here.

This is neither a published nor a submitted paper at the time of submission of this thesis.

Contributors

Inken Schulze, Peter Feldens, Mischa Schönke, Mayya Gogina, Michael L. Zettler
(all affiliated with the Leibniz Institute for Baltic Sea Research Warnemünde, IOW)

Abstract

The sedimentology of the Oderbank (Baltic Sea/German EEZ) is characterized by vast areas of fine sand. On the Oder Bank, elongated patches of mussel beds occur, which were the target of a multifrequency acoustic survey in January 2019. Most of the approx. 3 km long working transect shows a rather homogeneous backscatter pattern in a multifrequency dataset, recorded with a NORBIT iWBMS STX system. The mussel beds are expressed as elongated patches of increased backscatter strength in different frequencies (200 kHz, 400 kHz, 550 kHz, 700 kHz). Video images from a towed camera sledge show a strong overlap of high-backscatter patches with the occurrence of unattached mussel clusters on top of fine sand ripples. First results show that it is possible to detect these unattached mussel clusters and indicate a minimum abundance of mussel coverage required for detection in backscatter data. Mussel bed detection is independent of frequency. The secure identification of mussel beds in backscatter data allows to monitor their yearly dynamics. Further analysis will lead to an optimized detection strategy of mussels in the Baltic Sea.

3.1 Introduction

The mapping of habitats is important for the assessment and monitoring of marine environments. In the Baltic Sea, a habitat of special interest are the massive, spatially complex, biogenic structures that mussels build. These biogenic reefs alter the biotic and abiotic environment (van der Zee et al., 2012) and provide a variety of ecosystem services (Attard et al., 2020). Mussels themselves and associated fauna often provide essential food sources to higher and commercially important organisms (Westerbom, Lappalainen, Mustonen, & Norkko, 2018) and take part in the control of phytoplankton dynamics (Norén, Haamer, & Lindahl, 1999). Therefore, the biotope *Mytilus edulis* beds on littoral sand is listed as a habitat of principal importance in the Habitat directives (Directive, 1992). Such macrofaunal assemblage structures are often explored in terms of the species richness, abundance, biomass, and diversity. To integrate functionality, the bioturbation potential of macrofaunal assemblages can also be considered (as bioturbation has significant implication on the biogeochemical fluxes of marine sediments including climate-relevant carbon burial (Diesing, Thorsnes, & Bjarnadóttir, 2021). The conventional biological ground truthing for habitat mapping of mussel beds consists mostly of physical sampling, e.g., grabs, cores, scratch sampling by divers (Eleftheriou & Moore, 2013), and optical recordings, e.g., photos and video transects (Beisiegel et al., 2017). Either way, the investigated area size is very limited using these methods.

The presence of mussels and related bioturbation can cause changes in natural interface and volume roughness as well as sediment composition, having impact on acoustic signals (Briggs, Williams, Richardson, & Jackson, 2001; Schönke et al., 2019). This study tests whether the impact of mussels clusters of variable density can be observed in multibeam backscatter data of different frequencies. The acoustical data set is supported by physical and optical ground validation to constrain the lower sensitivity threshold for the occurring species of clam.

3.2 Data and Methods

3.2.1 Study Area

Geological Setting

The Pomeranian Bay is a shallow water area (6-20 m water depth) located in the southwestern Baltic Sea between Germany and Poland (Figure 3.1). During the Quaternary, Scandinavian ice sheets overprinted the region repeatedly (Wohlfarth et al., 2008). The following deglaciation, a complex interaction of the isostatic movements and sea level fluctuations led to various changes of the regime between freshwater and salt water to a nowadays brackish Baltic Sea (Björg, 1995). The most prominent morphological feature in the Pomeranian Bay is the Oder Bank with an average water depth of only 7-9 m in its central part. The glacial deposits are widely covered by an extended layer of mainly fine sands (Tauber, 2012).

The Pomeranian Bay with the Oder Bank is a protected area under the Habitats Directive (Directive, 1992) and part of the yearly biological monitoring of IOW, the initial reason for the choosing the survey site.
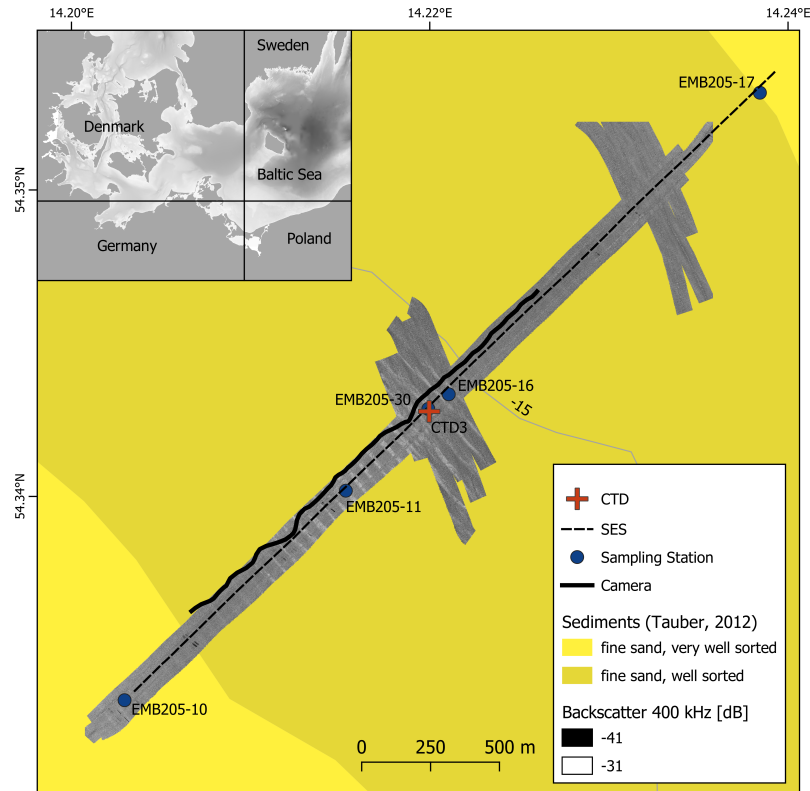
Figure 3.1: Location of the research area close to the Oder Bank in the southwestern Baltic Sea. Map projection: UTM33N WGS84.

3.2.2 Hydroacoustic Survey and Processing

Data acquisition and backscatter maps

Multibeam data acquisition for this study took place in January 2019 during cruise EMB205 on board of the German research vessel Elisabeth Mann Borgese (RV EMB).
The Norbit iWBMS STX multibeam echo sounder (MBES) is equipped with an Applanix Wavemaster sensor for motion compensation and was mounted to the moonpool of RV EMB. Since the calibration of this device was not completed at the time of the survey, backscatter data in this study are uncalibrated and can only be compared relatively (Lamarche & Lurton, 2018). Recording was done in data format s7k within the Norbit GUI. The received EGNOS correction data improved the navigation to approximately 0.5 m lateral accuracy. The ship speed varied around 3.5 knots.
The three main survey profiles in SW-NE direction of about 3000 m length and 120 m width followed from the already existing stations of the biological monitoring cruises. Based on observations of backscatter strength variations observed during a previous cruise, two smaller areas were surveyed in addition. All lines were successively sailed with 200, 400, 550, and 700 kHz frequency, since a continuous operation of the multifrequency mode was not yet possible in 2019.

For a detailed description of the MBES data processing see Chapter 2. All recording setting controlled by the user were kept stable throughout the survey, only the frequency and according absorption coefficient were changed.

Table 3.1: Multibeam echosounder setting during data acquisition.

Frequency [kHz]	200	400	550	700
Bandwidth chirp [kHz]	80	80	80	80
Chirp pulse length [ms]	0.2	0.2	0.2	0.2
Absorption coefficient [dB/km]	24	75	134	200
Spreading	40	40	40	40
Static gain	0	0	0	0

Angular Range Curves (ARC)

ARC data are assigned to two backscatter types for the angular range analysis: bare sand ripples and mussel clusters on sand, the respective areas were picked manually. The angular range curves were calculated using the raw data using the formula for angular backscatter strength (Hellequin et al., 2003):

$$\overline{BS(\theta)} = EL(\theta) - SL + 2TL - 10log(\overline{A(\theta)}) \tag{3.1}$$

The backscatter strength (BS) for a given incidence angle (θ) is calculated from the recorded echo level (EL), the source level (SL), the transmission loss (TL), and the ensonified area (A).

Parametric Echosounder

A high-frequency seismic profile was recorded with an Innomar parametric sediment echosounder to investigate the shallow subsurface geology. The sediment echosounder data was recorded during cruise EMB188 in July 2018. The primary frequency was set to 100 kHz, the secondary to 15 kHz. The data was binned at intervals of 1 m, and a manual time varying gain (TVG) was applied.

3.2.3 Ground Truthing

The HAPS is a framed sediment corer, and with its vibration unit and lids at the top and bottom, it is a suitable tool for physical ground validation in sandy environments (Kanneworff & Nicolaisen, 1972). At the stations in the working area four cores were taken each. One core for sedimentological analysis was sliced in 2 cm thick sections. The grain size of the fine-grained samples was optically analyzed with a Mastersizer 3000 using the dry measuring cell. Due to low organic content, no chemical pretreatment was applied to the sediment samples. Additionally, the depth distribution of shell debris for the top 10 cm of sediment was compiled.
For biological analysis, three replicate cores and two dredges with additional Van Veen grabs from two other stations were analyzed for abundance and biomass of dominant species.

3.2.4 Video Survey and Processing

The utilized towed video sledge is tailored to the needs of benthic imagery. It is equipped with a downward-looking camera system to record high-resolution photos and videos (Beisiegel et al., 2017). Four parallel lasers allow a scaling of the images, which cover an area of 0.8 m^2 when set on ground. As it is mounted directly at the vessel's stern center, the approximate position of the sledge at all times can be calculated including the offset to the ship's GPS reference point and gyro compass data.

In the video data, the dark mussel clusters stand out from the bright sandy seafloor. Analysis for topography reconstruction and mussel abundance estimation was based on exporting one image per second from the video data. Of the initial 5478 images, 1102 were manually sorted out due to bad quality, e.g., resuspension clouds when the video sledge touched ground. This results in some gaps in the following plots of the mussel coverage. Analysis included only the well-illuminated inner part of the images without the sledges frame.

3D Model of the Seafloor

Selected sections of the orthogonal recorded and overlapping images were used as input for the photogrammetry software Agisoft Metashape, creating a several meter long 3D model of the seafloor surface (Figure 3.2). This improves the spatial visualization, and the exported point cloud will allow further analyses of the small-scale morphological features on the seafloor surface including the mussel clusters.
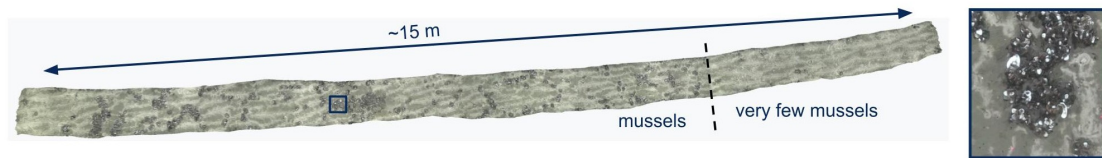

Figure 3.2: 3D image of *Mytilus edulis* clusters on rippled seafloor derived from underwater video footage. The sharp border between the mussel covered seafloor and bare sand ripples is indicated. A photo shows an example of a heterogeneous mussel cluster at the seafloor (right).

Mussel coverage

The red channel of each image was clustered, and after the application of dilation and erosion algorithms, a color intensity threshold divides the image's pixels in mussel and sand. Based on this classification, the percentage of mussel covered area is computed (an example is show in Figure 3.3).
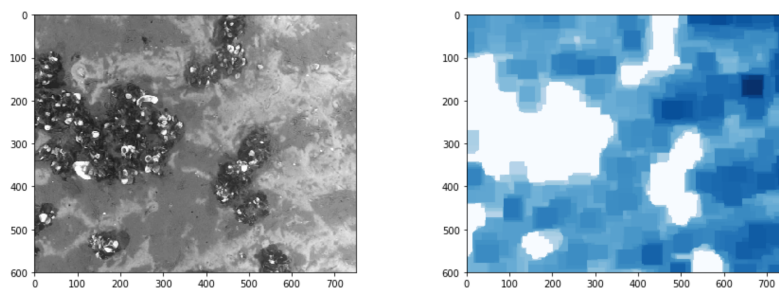

Figure 3.3: Homogeneous background sediments allowed to calculate mussel cover percentage by a color intensity threshold. In this example the mussel clusters in the photo (left) covered 25.1% of the image, represented by white color (right).

Benthic Species Identification

A reduced number of still images from video footage was used for benthic species identification. The software CPCe was used to identify classes beneath 50 randomly overlaid digital

points on each photo. The number of points for each identified taxon was standardized to percentage cover of the seafloor surface.

3.3 Results

3.3.1 Subsurface, Grain Size and Benthic Species

Subsurface

The sediment echo sounder profile (Figure 3.4, for location see Figure 3.1) indicates a thin homogeneous surface layer (composed of sand). Thickness of the layer increases to 1-2 ms between a profile offset of 1500 to 2500 meters. Below, an undulating series of reflectors is observed, that reach close to the seafloor surface especially at an offset from 0 to 1500 meters. No ground truthing of these reflectors is available. Video and hydroacoustic data show no indication of the reflectors outcropping at the seafloor.
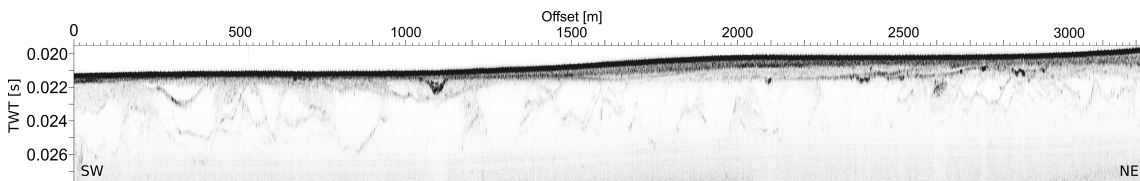

Figure 3.4: The sediment echosounder profile shows a thin superficial layer (composed of fine sand), with underlying, undulating reflectors.

Grain Size and Shell Debris

The retrieved HAPS cores are up to 30 cm in length, however analysis is concentrated on the upper 10 cm as hydroacoustics signals might be sensitive down to this depth. The investigation area is dominated by a homogeneous seafloor surface, composed of fine sand with a grain size of around 200 µm (Table 3.2). Variations in grain sizes with increasing depth are small. The content of shell debris is increasing at all stations from a depth of about 8 cm (Figure 3.5), particularly at Station EMB205-10, located in the southwestern edge of the study area.

Table 3.2: Grain sizes of the surface sediments (0-1 cm) at the HAPS stations in the working area (for location see Figure 3.1).

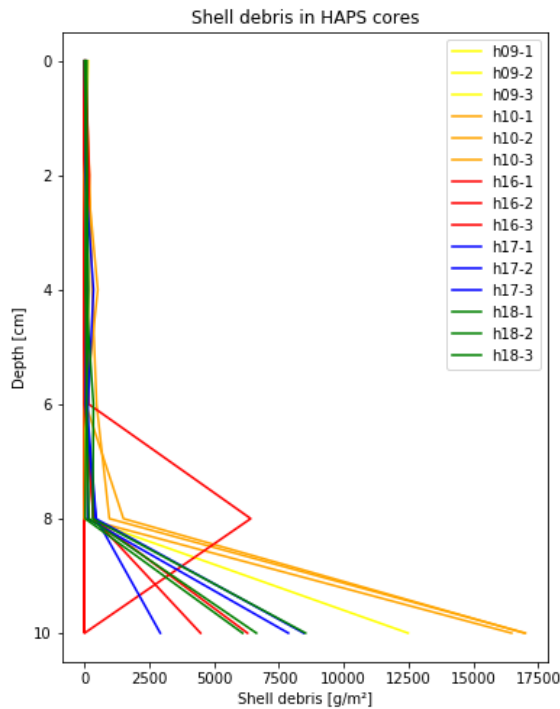| Station	EMB205-10	EMB205-11	EMB205-16	EMB205-17
Dx(10)[µm]	136	142	139	149
Dx(50)[µm]	211	221	214	228
Dx(90)[µm]	325	343	328	345

Figure 3.5: Distribution of shell debris in HAPS corer samples (abbreviated with "h" in the figure) for the upper 10 cm of sediment. Note: There are three core samples at every station. Stations EMB205-09 (h09) and EMB205-18 (h18) are located outside of the study area.

Benthic Species and Mussel Coverage

The benthic species in the HAPS core samples were analyzed for abundance and biomass. Overall abundance is controlled by *Peringia ulvae*, while wet biomass is dominated by *Cerastoderma glaucum* at most stations. Noteworthy, *Mytilus edulis* is only sampled at station 11, where it contributes significantly to wet biomass. The results are summarized in Figure 3.6. Mussel clusters on top of the fine sand ripples consist mostly of blue mussels (*Mytilus edulis*) with the bay barnacle (*Amphibalanus improvisus*) and the lagoon cockle (*Cerastoderma glaucum*) attached to it, as identified in the video footage and in dredge and grab samples.

A 3D image (Figure 3.2) visualizes the sharp boundary between the occurrence of patchy mussel clusters of variable density and the sandy seafloor with only isolated occurrences of mussels and no extended clusters. Within the mussel clusters, mussel coverage derived from the video data varies between 0% and 49.8% (Figure 3.8). The regular distance between peaks of high coverage is approximately 50 m.

Available underwater photos were assigned to groups defined by Hierarchical Cluster and Non-metric Multi-Dimensional Scaling analysis based on coverage data. The two most frequent groups were characterized by a relative high coverage with unattached mussel clusters or bare sand indicating an infauna-dominated habitat, respectively. Examples of the two major groups are shown in Figure 3.7.
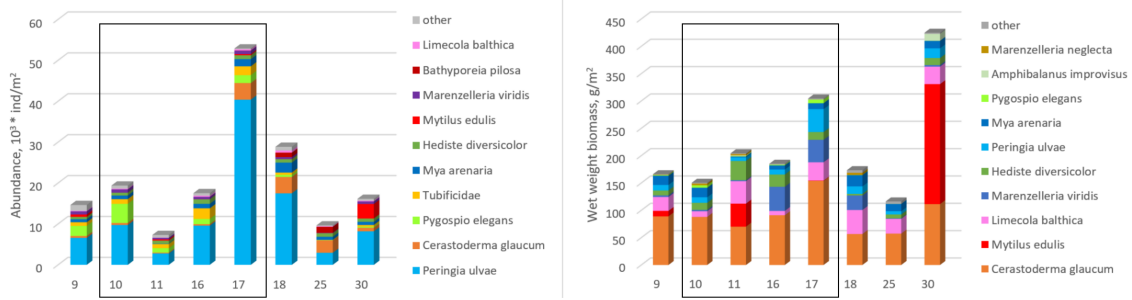
Figure 3.6: Abundance (left) and biomass (right) of dominant species at each sampling site. Species contributing to over 96% of total abundance and 98% of total wet weight biomass are shown. Stations within the study area are marked by black boxes.
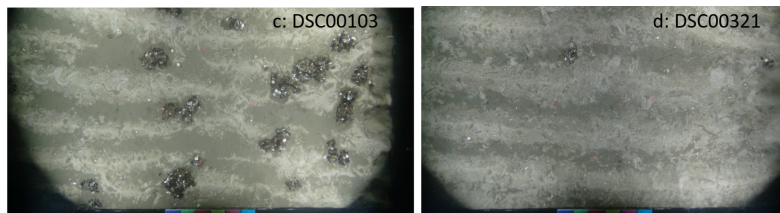

Figure 3.7: Underwater photos of two major groups, dominated by unattached mussel clusters (left) and sand (right).
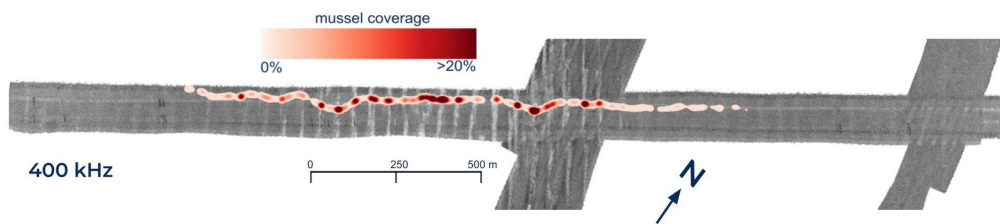

Figure 3.8: MBES backscatter map at 400 kHz frequency. A relation between backscatter intensity and mussel coverage as identified on video footage is recognized. Data gaps in mussel coverage exist due to rejected photos of bad quality.

3.3.2 MBES Backscatter Characteristics and video transects

Stripes of high-backscatter strength run parallel in the central part of the investigation area with a very regular spacing of approximately 50 m. Their appearance is similar in all four frequencies and intensity of the stripes decreases towards the southwest and to the northeast. The shape of the stripes is uneven and partly interrupted (Figure 3.9). The position of the stripes is not related to the apex of undulating reflections observed in subsurface data especially towards the southwest (Figure 3.4). The comparison with underwater video images allows to relate the high backscatter stripes to the occurrence of mussel clusters. Furthermore, the high coverage peaks coincide with the backscatter stripes of high intensity (Figure 3.8).
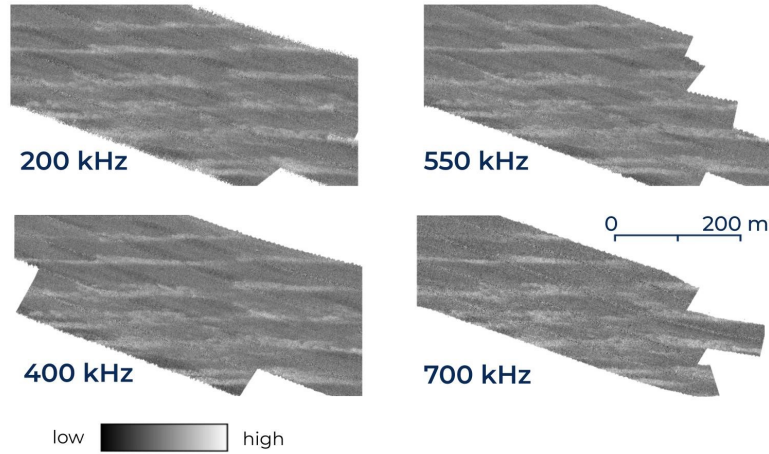
Figure 3.9: The central part of the investigation area at different frequencies (200, 400, 550, and 700 kHz). Elongated stripes of increased backscatter intensity are interpreted as mussel beds based on comparison with underwater video videos. The change in intensity compared to the surrounding fine sand seafloor varies subtly between the frequencies.

The angular range curves (Figure 3.10) show an increase of 2-3 dB for angles more than 30 across the higher backscatter stripes (mussel clusters). This pattern is similar for all four frequencies.
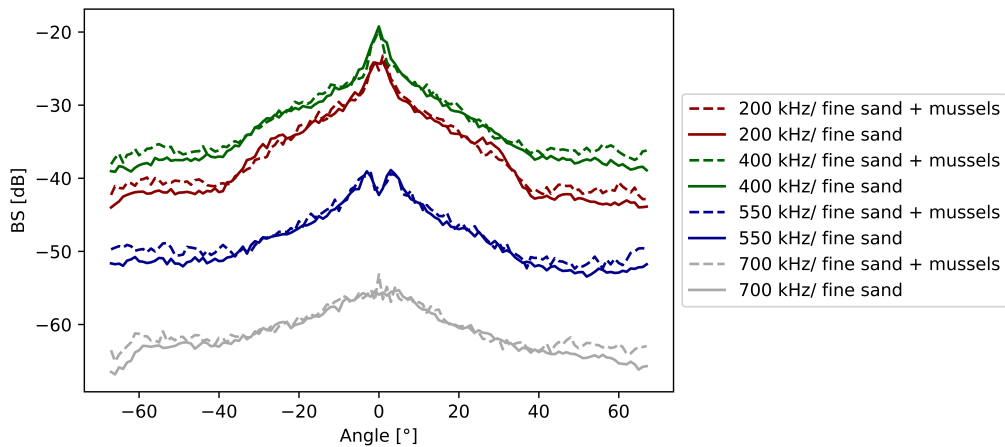
Figure 3.10: The angular range curves (ARC) show an increase of 2-3 dB for incidence angles of more than 30 in all four frequencies if mussel clusters are present.

3.4 Discussion and Outlook

The surface of the study area is composed of fine sands, confirmed by the sediment samples and video footage. While subsurface layering is present closely beneath the seafloor, no outcropping geological features or changes in sediment composition could be observed on the seafloor. This would be especially expected in the SW part of the investigation site, where the fine-sand cover appears to be thin (Figure 3.4). Therefore, the presence of stripes of increased backscatter strength are related to a biological origin, the appearances of loose mussel clusters in the video footage showing a similar regularity. Yet, a cause for the formation of the loose mussel clusters in elongated stripes was not found. Local

hydrodynamic conditions, such as Langmuir circulation (Barstow, 1983), likely have an influence as the mussel clusters are not attached to the ground and easily moved. The high spatial heterogeneity observed in backscatter intensities and the positional inaccuracy of HAPS point samples indicates that the results of the HAPS species analysis are difficult to directly relate to the acoustic information. This in turn indicates that few point samples are inadequate to build time series of species distribution in the (rather homogeneous) Oder Bank habitat, especially if distribution of benthic depends on oceanographic conditions.

Video data and coverage analysis shows that a certain abundance of mussels is required for the reliable detection above background noise in backscatter data. Preliminary, this threshold is estimated with 10%, confirming earlier results by Schönke et al. (2019) that low abundance benthic life is not imaged in acoustic data. A quantitative relationship between backscatter intensity and mussel coverage can not be derived at this time. As observed in Figure 3.8, a thin horizontal line of apparently increasing backscatter intensity crosses the video footage. This line represents an acoustic artifact, and unfortunately crosses a large percentage of the video footage.

The measurement of backscatter strength for the detection of mussel on a sandy seafloor is not frequency-dependent when compared to other investigated habitat types in this thesis. This is confirming the observations of the mussel-covered reef at the study site Hohe Düne (Chapter 4), where backscatter differences between frequencies are very small. Therefore, in the range of frequencies available on our multibeam system, no recommendation can be made regarding frequencies for mussel detection. In addition, the along-track backscatter intensities are unaffected by buried shell layers reaching close to the seafloor. This indicates that even the lowest frequency does not penetrate sufficiently to 8-10 cm in this environment to change the measured backscatter through increased volume scatter. This limit is in line with observed penetration depths for 200 kHz in fine sand (Huff, 2008).

The video footage turned out to be an effective ground truthing method, not only for benthic species identification but for potentially improving the interpretation of backscatter measurements. The downward-looking positioning of the video camera allowed for the creation of high-quality 3D models. The images enhanced the spatial visualization of mussel clusters as well as surface sediment morphology, e.g. sand ripples. Furthermore, roughness spectra of the point clouds exported from the 3D model can be calculated to quantify the impact of mussels on surface roughness (Schönke et al., 2017) over larger spatial scales when combined with underwater laser line recordings, important for backscatter intensity (Ferrini & Flood, 2006).

3.5   Conclusion

This study tested the direct impact of mussels (*Mytilus edulis*) on backscatter strength. Mussel clusters and their spatial extension can be well detected in backscatter data independent of available frequencies. Qualitatively, a relation between abundance and backscatter intensity can be observed, but requires further investigation.

Paper II
Seasonal Change of Multifrequency Backscatter in three Baltic Sea Habitats

Seasonal Change of Multifrequency Backscatter in three Baltic Sea Habitats

Inken Schulze [1,*]**, Mayya Gogina** [1]**, Mischa Schönke** [1]**, Michael L. Zettler** [1] **and Peter Feldens** [1]

[1]*Leibniz Institute for Baltic Sea Research Warnemünde, Germany*

Correspondence*:
Inken Schulze, Seestrasse 15, 18119 Rostock, Germany
inken.schulze@io-warnemuende.de

2 ABSTRACT

This study investigates the seasonality of acoustic backscatter intensities, exploring three habitats in the southwestern Baltic Sea: (1) a mussel covered reef, (2) coarse sand and gravel and (3) seagrass meadows. Backscatter information of different, partly calibrated, frequencies (200, 400, 550 and 700 kHz) were collected in three seasons (May, August, October). The acoustic data were supported by point-samples and video profiles for grain size and benthic community analysis. Angular response curves helped to quantify the seasonal backscatter response of the different frequencies. The multifrequency and multiseasonal backscatter maps distinguish the three habitats and reveal variable seasonal differences in acoustic backscatter, but not all changes in benthic community can be recognized in the acoustic data. (1) The high backscatter response of the mussel-covered reef shows little seasonal differences and was frequency independent. (2) The ecologically valuable coarse sand and gravel areas show small-scale seasonal alterations in the sediment composition and morphology, mainly caused by changes in local hydrodynamics. Higher frequencies were found best suited to identify coarse sand and gravel. (3) Seagrass meadows seasonality is dominated by growth of seagrass blades, increasing the backscatter response compared to bare sand. The use of multiple frequencies is beneficial as the low frequency is sensitive to changes in the shallow subsurface and benthic features such as seagrass rhizomes, while the higher frequency highlight changes related to coarser sediment.

Keywords: habitat mapping; multibeam echo sounder; backscatter; angular response curves; multifrequency; Baltic Sea

1 INTRODUCTION

Habitat mapping is of growing importance to assess the environmental state of the sea and for subsequent monitoring to identify changes. In shallow waters, acoustic surveys can complement remote sensing based on satellites and airplanes. In turbid waters as well as intermediate and deeper water depths where optical methods such as satellite imaging and LiDAR cannot be used (Song et al., 2015), acoustic remote sensing is the method of choice. Targets for acoustic remote sensing include the geological conditions, but also the biodiversity, particularly benthic life (Rattray et al., 2009). Abiotic and biotic properties of the seafloor are affected by seasonal changes of, e.g., temperature, oxygen, salinity, daylight, wind stress or currents. However, the research data about seasonal changes in acoustic backscatter data is limited, especially

1

31 regarding the influence of benthic habitats on acoustic signals. In general, understanding of seasonal
32 variability in benthic habitats and inhabitating macrofaunal communities is still limited.

33 In acoustic remote sensing, backscatter data recorded with multibeam echosounder (MBES) or side-
34 scan sonar (SSS) are widely used to derive sedimentological parameters (e.g. grain size), and localize
35 hard substrates (Dartnell and Gardner, 2004; Tauber, 2012; Papenmeier et al., 2020), which are often
36 required as basic input for benthic habitat maps or for habitat modelling (Darr et al., 2014; Schiele et al.,
37 2015). In recent years, studies have indicated a great potential for an improved seafloor classification and
38 interpretation (Clarke, 2015; Gaida et al., 2018; Janowski et al., 2018; Feldens et al., 2018; Brown et al.,
39 2019; Costa, 2019). The focus is hereby not only on the high frequencies allowing for a high resolution,
40 but on the investigation of the optimal frequency combination for the distinction of specific habitats. The
41 inclusion of lower frequencies seem to provide more contrast, especially in soft sediment habitats (Costa,
42 2019). The signal penetrates deeper into the sediment than in case of higher frequencies, generating
43 additional volume scattering that may be used to differentiate habitats. Even though the exact scattering
44 depth remains unknown, more comprehensive information about the upper centimeters of seafloor can be
45 gained (Feldens et al., 2018), that is of interest for investigations of sediment layering, bioturbation traces,
46 or roots/rhizomes. A limited, but increasing number of studies investigate the direct impact of benthic
47 communities on backscatter properties of commonly used acoustic devices, thereby opening the possibility
48 of efficiently surveying basic biological parameters of macrobenthic communities. Recent investigations
49 show a potential for acoustic mapping of, e.g., tube worms (Heinrich et al., 2017), squid egg clusters (Foote
50 et al., 2006), mussel beds (Snellen et al., 2008), corals (Czechowska et al., 2020), or bristle worms (Feldens
51 et al., 2018). In case of benthic flora studies include, e.g., seagrass meadows (Held and Schneider von
52 Deimling, 2019) (an extended list of papers can be found in the review paper Gumusay et al. (2019)), or
53 macroalgae (Kruss et al., 2017). Increasing sensitivity brings up the question to which extent seasonality is
54 reflected in acoustic surveys of abiotic and biotic habitats. This is important for both the establishment of
55 time series for monitoring purposes, as well as for interpreting the results of acoustic surveys undertaken in
56 different seasons.

57 In this meso-scale field study, we test if seasonal changes can be observed in the MBES backscatter
58 strength of different frequencies (calibrated 200 and 400 kHz, uncalibrated 550 and 700 kHz) in shallow
59 water habitats close to the coastline (for location see Figure 1). Three habitat types, which are common in
60 the southern Baltic Sea, are the focus of our investigation: (1) a reef covered by mussel banks, (2) coarse
61 sand and gravel (CSG) and (3) seagrass meadows on fine sand. The comparison of backscatter mosaics
62 for three months (May, August, October) highlights seasonal changes. The compilation of multifrequency
63 backscatter to a false-color image allows for a rapid spatial overview, while angular response curves show
64 more detailed information on the acoustic response of the habitats to different frequencies. Biological and
65 sedimentological ground truthing with grab samples support and validate the acoustic measurements.

2 MATERIALS AND METHODS

2.1 Study site

67 The investigation site is located near Hohe Düne/Rostock (HD) in the southern Baltic Sea in water
68 depths of 5-7 m and less than 1200 m distance to the coast (Figure 1). The site was chosen based on
69 accessibility, and presence of different habitats according to the HELCOM Underwater biotope and habitat
70 classification system (Schiele et al., 2015). Three different biotopes were predicted for the study site:
71 Photic sand dominated by multiple infaunal bivalve species including *C. glaucum/ M. balthica/ M. arenaria*

72 (AA.J3L9), photic mixed substrate dominated by algae (AA.M1C/S), and photic mixed substrate dominated
73 by epibenthic community (AA.M*1). Nearby, photic sand dominated by multiple infaunal polychaete
74 species including *Ophelia* spp. and *Travisia forbesii* (AA.J3L11) is found. The area is under anthropogenic
75 influence including: frequent waves formed by large ferries, commercial fishing with gill nets, proximity of
76 marina, and high coastal tourism activities. Additionally, there is a freshwater discharge from the Warnow
77 River, after its flow through the city of Rostock.

2.2 Field work

79   Acoustic data in the Hohe Düne focus area were recorded using a Norbit STX echo sounder mounted
80 on IOW's research vessel Klaashahn, a 7 m long aluminum catamaran. Surveys were done in May 2019,
81 August 2019 and October 2019, to cover three different seasons. Weather conditions in May 2019 allowed
82 only for a limited dataset. The Norbit iWBMS STX multibeam echo sounder (MBES) is equipped with an
83 Applanix Wavemaster sensor for motion compensation. The received EGNOS correction data improved the
84 navigation to better than 1 m accuracy both in latitude and longitude. In August and October, real-time
85 kinematic positioning (RTK) corrections were used to improve the navigation to cm accuracy. To ensure
86 calibration, data were recorded using an equiangular spacing of 512 beams without roll compensation,
87 following manufacturer recommendations for the use of calibrated systems. The pulse length was set to 0.2
88 ms. Although systems settings are removed by the calibration process, all user-controllable gain settings
89 were kept stable throughout the survey, only the frequency was changed. The ship speed varied around
90 3.5 knots. Line direction was enforced by weather conditions and wave direction. Sampling of sediment
91 and biological material was done using a grab sampler with an area of 0.04 m^2. Additional measurements
92 included the water temperature, the salinity, and the level of oxygen. Underwater video data was recorded
93 along parallel profiles at the slowest possible speed with a forward and oblique-looking HD video camera
94 (Seaviewer Sea Drop 6000 HD). The optical and physical ground truthing was mostly done within the
95 same week as the acoustic survey, however some delays (up to one month) were caused by bad weather
96 conditions. Grain size analysis was done by sieving for sediments with components larger than 2 mm,
97 while optical grain size analysis was done for samples composed of fine sand.

2.3 Acoustic data processing

2.3.1 Backscatter data

100   Data were re-exported utilizing Norbit software to incorporate true heave correction and correct the data
101 against manufacturer-supplied system bias. The result of the export are s7k-files, with uncalibrated snippet
102 and manufacturer-calibrated backscatter time series data available for the 200 and 400 kHz frequency. The
103 determination of system bias of the MBES was done by the manufacturer for the frequencies of 200 and
104 400 kHz by calibration with spheres in a test tank, and is applied through a device-specific calibration
105 file. Bathymetric grids were created utilizing the software QPS Qimera with a resolution of 0.25 m. In
106 the software QPS FMGT backscatter mosaics with a resolution of 0.25 m were created. An angle varying
107 gain (AVG) in 'flat' mode with a window size of 300 pings was applied and the mosaicing style set to
108 'blend'. Some data gaps were caused by bad weather conditions, which made navigation along straight lines
109 difficult with the available vessel. The data obtained in August did not allow the creation of an adequate
110 bathymetric map due to wave impact.

2.3.2 False color images

For visualization purposes the backscatter mosaics are combined to false color images. For better comparison, the backscatter range for each frequency is the same for all maps in this study (Table 1). The different frequencies are assigned to two or three of the color channels (red, green and blue, RGB), creating dualfrequency or multifrequency backscatter maps. As only two frequencies (200 and 400 kHz) are calibrated and available for all three months, the dualfrequency maps are preferably shown and discussed. False color images are also used to visualize the seasonality of the investigation site. In this case, each color channel (RGB) is assigned to the backscatter intensity of one month.

2.3.3 Angular response curves

The calibration allows the direct display of angular response curves (ARC) to support the interpretation of the backscatter maps and the identification of habitats. The angular backscatter strength (Hellequin et al., 2003) is defined as:

$$\overline{BS(\theta)} = EL(\theta) - SL + 2TL - 10log(\overline{A(\theta)}) \tag{1}$$

where BS is the angular backscatter strength, θ is the incidence angle, EL is the recorded echo level, SL is the source level, TL is the transmission loss (spreading + absorption) and A is the ensonified area. Due to the manufacturer calibration, only values for spreading and absorption (Table 1) were set during data export in the Norbit GUI. To display the ARC, data were exported to s7k format and the snippet information was exported with mbsystem (Caress and Chayes, 1996, 2017). The incidence angle was then calculated from height above the seafloor and across-track distance, assuming a flat seafloor assumption. This assumption is valid for our investigation site, as the observed slope values are minor. To reduce noise, the data of 100 pings was averaged, and then binned into 2°-intervals, displayed from 0° to 70°.

2.4 Biological data processing

Samples were washed through 1 mm mesh-size and preserved in 4% buffered formaldehyde-seawater solution. All macrobenthic organisms were sorted, identified to the lowest possible taxonomic level, counted and weighted to obtain wet weight biomass (WW). Ash-free dry weight biomass (AFDW) was also derived from wet weight using conversion factors (Gogina et al., 2022). Taxonomy was checked to follow the World register of Marine Species WoRMS.

Kruskal-Wallis test was used to identify significant differences in terms of main biological parameters. Community composition was analyzed using multivariate techniques hierarchical cluster analysis and analysis of similarity (ANOSIM) in the program PRIMER v7 (Clarke and Gorley, 2015). Biological resemblance among samples was quantified using pairwise Bray-Curtis similarities on log-transformed WW biomass data (as it was expected to be more relevant for acoustic response, than AFDW). Indicator Value analysis (IndVal (Dufrêne and Legendre, 1997)) implemented in R package "labdsv" (Roberts, 2013) was used on biomass data matrix to identify the main taxa which were responsible for differences in community structure. IndVal is a product of specificity (mean biomass of a given taxon within a cluster compared with the other clusters) and fidelity (taxon occurrence at stations belonging to a cluster), with values reaching 100% when a given taxon is observed at all stations of only one cluster.

3 RESULTS

3.1 Overview

The bathymetric and backscatter maps of the Hohe Düne (HD) investigation site are displayed in Figure 2. The water depths varies between 4.8 m and 7.4 m. The area was separated into the broad habitats coarse sand and gravel (CSG), reef covered with mussels and seagrass meadows. Their typical appearance in underwater video footage is shown in Figure 3. The three habitats are recognized by their different appearance in a multifrequency backscatter mosaic (Figure 2b). The general morphological differences within the HD site are minor. The reef forms a local bathymetric height elevated approximately 60 cm above the surrounding seagrass meadows and the CSG habitats. Small-scale morphological changes within the patchy seagrass meadows cannot be determined due to interference of the plants with the acoustic signal. Within the CSG area, elongated dunes protrude a few tens of centimeters above their surroundings (Figure 2a). The clay and silt, sand and gravel distribution for the three facies is shown in Table 2. The same stations were sampled in different seasons. Larger boulders are present in the video footage, but could not be retrieved with the utilized grab equipment.

The analysis of benthic communities, from 53 samples collected during the three sampling campaigns, resulted in 643 observations of 64 taxa, including: 23 taxa of arthropods (crabs, shrimps, barnacles), 20 taxa of annelids (polychaetes and oligochaetes), 14 species of molluscs (clams, sea slugs, snails), 4 species of bryozoans, 1 species of platyhelminths (flat worms), 1 species of echinoderms (sea star) and 1 taxa of nemerteans (ribbon worms) (details in supplementary material Table S1). In all three seasons, higher values of wet biomass were found in the central and south-eastern parts of the study site, corresponding to the reef habitat (details on biomass in the investigation site are given in Supplementary Figure S1). Wet biomass values in the CSG habitat were consistently the lowest, particularly for the two stations in the north-west and north-east corners of the study area (HD13 and HD16). However, both, high seasonal fluctuation and variability between replicates was observed in all habitats, presumably also related to small-scale patchiness in the investigation site and relatively small sampling area of the grab (0.04 m^2).

3.2 Reef

3.2.1 Acoustics and Geology

The Reef facies is characterized by generally high backscatter intensities (Table 3). On the reef, stripes and patches of intermediate-backscatter intensity oriented in NW-SE direction appear irregularly (Figures 4c-h). They are recognized in bathymetric data as shallow hollows (Figures 4a,b) and ground truthing shows exposed sand patches. In the October multifrequency backscatter map with the additional frequency of 550 kHz (Figure 2b), the exposed sand patches appear in dark blue colors, indicating a preferred high-frequency response. Outside of the sand patches, changes in dominant frequency are controlled by background noise with little frequency sensitivity, resulting in an overall bright yellowish colour in the dual-frequency (Figures 4i-k) and bright greyish colors in the three-frequency mosaic (Figure 2b). Boundaries of the Reef facies to the CSG and Seagrass facies are generally distinct (Figures 2b).

The sediment samples retrieved in the Reef facies have an overall composition of fine to medium sand (Table 2). Stones and large boulder accumulations are observed in underwater video footage, but appear rarely in the exposed sand patches (Figures 3d-f).

185 3.2.2 Biology

186 The majority of the Reef facies is covered by variable densities of the mussel *Mytilus edulis* (Figures
187 3a-c). *M. edulis* contributes to biomass with 80 to 99%. Decreasing densities of *M. edulis* correspond to
188 the occurrence of patches of exposed coarse sand. Camera profiles show that at the transition from the
189 high-backscatter reef to the low backscatter sand patches mussels are replaced by rippled sand (Figures
190 3d-f). Excluding blue mussels, however, the remaining biomass is lower than at the seagrass habitat and is
191 dominated by crustaceans, isopods and gastropods. Species that discriminate this habitat are *Amphibalanus*
192 *improvisus*, *Microdeutopus gryllotalpa*, *Gammarus spp*, *Littorina saxatilis*, *Littorina littorea*, *Pusillina*
193 *inconspicua*, *Polydora cornuta* and *Alitta succinea* (detailed countings in Table S1). *Asterias rubens*
194 was mostly observed in video records from this zone. The vegetation was mostly represented by foliose
195 and encrusting red algae of phylum Rhodophyta, like *Polysiphonia fucoides*. Less common were the
196 observations of relatively small specimens of *Delesseria sanguinea*.

197 3.2.3 Seasonal Change - Geology

198 For the complete Reef facies, a reduction of backscatter intensity is observed at the 200 kHz frequency
199 from May to August, while average values remain constant from August to October (Table 3). The
200 backscatter strength decreased for 200 kHz from May to October, although isolated spots of increasing
201 backscatter strength occur (Figures 5a,c,e). These spots formed from August to October (Figures 4l,m).
202 As a consequence, in the multiseasonal backscatter map the Reef facies is represented by reddish colors.
203 The exposed sand patches (low-backscatter stripes) show the strongest backscatter response in October,
204 represented by dark bluish colors (Figure 6a).

205 For the 400 kHz frequency, a slight overall increase of backscatter strengths is observed from May to
206 August, while a slight decrease prevails during the second time period from August to October (Figures
207 4n,o). For the total observation period from May to October, mainly an increase of backscatter strength at
208 isolated spots is observed (Figures 5b,d,f). In the multi-seasonal map (Figure 6b), the higher response in
209 August is indicated by a greenish colour, and some blue patches point out spots of maximum backscatter
210 intensity observed in October.

211 An interesting detail is observed in the southeast of the Reef facies (marked with circles in Figure 5).
212 Dense seagrass patches embedded in the reef in an area also densely covered by *Mytilus edulis* show a
213 strong decrease in backscatter from May to October for both frequencies, the 200 kHz and 400 kHz. This
214 is in contrast to backscatter seasonality in the Seagrass facies as described later.

215 3.2.4 Seasonal Change - Biology

216 Though both total biomass and biomass of blue mussels were slightly higher in autumn, according to
217 Kruskal-Wallis test these changes were not significant. Surprisingly, *Amphibalanus improvisus* nearly
218 disappeared in summer, but showed significant increase of biomass in autumn comparing to spring values
219 (Table S1, Figure S3). *A. improvisus* is commonly attached to various bivalve shells (dead or alive),
220 including blue mussels, and is known to tolerate strong water flow, large range of salinity and high
221 levels of pollution. Thus such an abrupt drop in biomass can possibly be explained by predation. Apart
222 from benthofagous fish, *Asterias rubens* and the crab *Carcinus maenas* both prey upon blue mussels and
223 associated epibionts (Laudien and Wahl, 1999). A prominent change in video data is the occurrence of
224 the pseudo-seasonal red algae *Polysiphona fucoides* during summer (Figure 3b). This is a relatively small
225 pseudo-seasonal seaweed that can sometimes be seen as an indicator for high nutrients availability and
226 fast growth rates. Annual fronds of many red seaweeds typically regenerate in spring and die back in the

227 autumn, causing seasonal change in the seaweed cover that is most dense between April to September
228 (Maggs and Hommersand, 1993).

229 ### 3.3 Coarse sand and gravel (CSG)

230 #### 3.3.1 Acoustics and Geology

231   The CSG facies is located in the northeast and northwest of the investigation site. The transition of
232 CSG to Seagrass facies is continuous, with a gradual increase of response to higher frequencies in the
233 multifrequency backscatter mosaics (Figure 2b). The transition from the CSG to the Reef facies is generally
234 sharp. Within the CSG facies, a high percentage of gravel and coarse sand was observed at sample locations
235 HD12 (in August) and HD16 (in October), where backscatter intensities are elevated. Remaining sample
236 locations showed low to intermediate backscatter intensities and fine to medium sand, with HD14 and
237 HD13 showing increased medium sand contents, and sample HD16 (in August) dominated by fine sand
238 (Table 2). The alteration of the sediment regimes can be observed in the seasonal video footage (Figures
239 3d-i). The monofrequency images show little difference in areas composed of fine to medium sand, though
240 contrast in the 200 kHz frequency increased, which is reflected in the dualfrequency mosaic (compare
241 Figures 7d,g). Seafloor composed of coarse sand gravel shows relatively stronger backscatter intensities
242 at higher frequencies, which results in greenish colours in the dualfrequency mosaic (compare Figures
243 7f,i) and bluish colours in the multifrequency mosaic with 550 kHz (Figure 2b). Areas with a stronger
244 response to high frequency scatter are widespread in the northwest of the study site, and less common in
245 the northeast.

246 #### 3.3.2 Biology

247   Community displays lowest total biomass, total abundance and species richness (Figure S1). The
248 similarity of community structure of the two stations considered to be concisely located within the CSG
249 habitat (HD13 and HD16) is relatively low (Figure S2). The biomass at station HD13 in April and August
250 was dominated by blue mussels (*M. edulis*), but the species was completely absent in the October sample.
251 However, large mussel patches on coarse sand were observed in some video data from October. The
252 second species in terms of biomass dominance was *P. ulvae*. Characteristic taxa revealed for this habitat
253 by Indicator Value analysis based on biomass were polychaetes *Capitella capitata*, *Hediste diversicolor*,
254 and *Paraonis fulgens*. Overall abundance was dominated by *P. ulvae* with a minimum of 100 ind/m^2 in
255 spring and a maximum of 7325 ind/m^2 in autumn (when the contribution of taxa exceeded 95% of relative
256 abundance at both station). Traces of *Arenicola marina* were also observed with underwater imaging in
257 this zone, though density was lower comparing to seagrass habitat, and shape of coiled castings was less
258 pronounced due to sediment properties.

259 #### 3.3.3 Seasonal Change - Geology

260   The bathymetry of the CSG facies indicates a seasonal change. In May, the seafloor is characterized by a
261 smooth seafloor morphology with few large scale features, while in October NW-SE elongated sediment
262 ripples shape the seafloor in the northeast (Figures 7a,b).In the backscatter maps, corresponding small-scale
263 stripes of increasing backscatter strength develop from May to October, elongated in the same NW-SE
264 direction (Figures 7c-h). Generally, average backscatter intensities in the CSG facies remain constant
265 throughout the seasons (Table 3), however differences are observed on smaller scales.

266   Low to intermediate backscatter areas (fine to medium sand) show an intensity decrease, while high
267 backscatter areas (coarse sand and gravel) show an intensity increase in the period from May to August

268 (Figures 5a,b and more detailed Figures 7l,n). Towards autumn, the backscatter increases for areas of fine to
269 medium sand from August to October, but decreases for areas composed of coarse sand and gravel (Figures
270 5c,d and more detailed Figures 7m,o). Seasonal changes at the 200 kHz frequency are more pronounced for
271 the fine sand to gravel areas, while the changes in the 400 kHz frequency focus on coarse sand and gravel
272 seafloor. The result is a reversed appearance in the difference plots for the change from May to August and
273 August to October (Figures 5a-d), but a similar pattern for both frequencies in the difference plot from May
274 to October (Figures 5e,f).

275 The multiseasonal backscatter maps represent small-scale seasonal variations within the coarse sand
276 and gravel seafloor by compositions of bright colors (Figure 6). The fine to medium sand seafloor shows
277 less seasonal variations, and consequently dark colors dominate. Spots of green or blue color indicate
278 small-scale backscatter variations in August and October. The high-backscatter stripes in the northeast
279 developed in August and October appear are more distinct in the 400 kHz frequency (green-blueish colors).

280 3.3.4   Seasonal Change - Biology

281 The biomass of *P. ulvae* and *C. glaucum* increased from spring to autumn, though the pattern for the
282 latter species was not consistent between stations. At both stations the biomass of *M. arenaria* was high in
283 summer, but the species was absent or contributed only little in other seasons.

284 **3.4   Seagrass**

285 3.4.1   Acoustics and Geology

286 Sediment in the seagrass area is dominated by fine sand (Table 2). Seagrass itself affects both
287 measurements of bathymetry and backscatter intensity. The bathymetry map shows a smooth seafloor
288 surface in May, except for data artefacts (Figure 8a). In October, numerous patches with sharp edges and
289 small diameters (smaller 1.5 m) occur, protruding the sediment by up to 0.4 m (Figure 8b).

290 The Seagrass facies is generally characterized by low to intermediate backscatter intensities for the
291 uncovered sandy seafloor (as in May, Figures 8c,f) and high backscatter intensities if seagrass patches
292 are present (Table 3). In the multifrequency image from October with an additional frequency of 550
293 kHz (Figure 2b), the seagrass appears in patches of red to brownish colors, indicating a relative increase
294 of 200 kHz scatter. In May, the combination of cloudy patches of increased backscatter strength on a
295 low-backscatter background at 200 kHz frequency (Figure 8c) and only few patches of medium backscatter
296 strength on a low-backscatter background at 400 kHz frequency (Figure 8f) results in a dualfrequency
297 backscatter map dominated by dark, reddish colors (Figure 8i). For August and October, both frequencies
298 show patches of increased backscatter strength (visible in Figures 8d,e,g,h). Contrast is increased in the
299 200 kHz frequency, causing several red spots in the dual-frequency mosaics (Figures 8j,k).

300 3.4.2   Biology

301 The seagrass habitat is shaped by common eelgrass *Zostera marina* species. Traces of presence and
302 sediment reworking by the lugworm *Arenicola marina*, particularly its coiled castings, were commonly
303 observed at video records between the seagrass canopies. Contributing most to the overall similarity
304 between samples (stations HD01, HD02, HD05, HD09) were biomass-dominating bivalves *Mya arenaria*,
305 *Cerastoderma glaucum* and *Macoma balthica*. Their average share of total biomass corresponded to 24, 23
306 and 19%, respectively.

58

307 ### 3.4.3 Seasonal Change - Geology

308 From May to October, increased backscatter strengths are observed for both frequencies, although for the
309 200 kHz frequency some patches of decrease occur (Figures 5e,f). The increase of seagrass abundance
310 from May to August (Figures 3j-l) coincides with an increase of backscatter intensities especially for the
311 400 kHz frequency (Figures 5a,b, Table 3). During the period from August to October, both frequencies
312 showed either constant or only slightly decreasing backscatter strengths, with only occasional patches of
313 increase (Figures 5c,d and detailed Figures 8m,o). Higher backscatter strength in August and October
314 resulted in the appearance of the Seagrass facies as green-turquoise patches on dark background in the
315 multiseasonal backscatter maps (Figure 6a).

316 ### 3.4.4 Seasonal Change - Biology

317 Biomass of Cerastoderma glaucum and Peringia ulvae increased from spring to autumn, whereas biomass
318 of M. arenaria and M. balthica were highest in spring and significantly decreased thereafter. Presumably
319 due to the impact of winter storms eelgrass canopies were significantly reduced in April compared to higher
320 cover in August and October (Figure 3). Total density of macrofauna in samples collected from seagrass
321 meadows habitat indicated significant increase from season to season (Figure S1). Generally, ANOSIM
322 results suggested that there were no significant differences between seasons in the infauna community
323 structure expressed in biomass. For further details, refer to Table S1.

324 ## 3.5 Angular range analysis

325 The angular response curves show the behavior of the different frequencies with regard to the specific
326 habitat and season. The decrease of backscatter intensity with increasing incidence angle backscatter ranges
327 is larger for the 200 kHz frequency comparing to 400 kHz. The Reef facies shows larger seasonal variability
328 in the low frequency, where the backscatter strength decreases throughout the year. The higher frequency
329 shows a slight increase of backscatter values for August and only minor differences between May and
330 October. The CSG facies is characterized by a high variability in backscatter values. In May, backscatter
331 values are highest at 200 kHz frequency, and distinctly lowest at 400 kHz. Backscatter values for August
332 and October show only minor differences for both frequencies. The ARC for both, Reef facies and CSG
333 facies, show undulations in all months, more pronounced at 200 kHz frequency. The Seagrass facies shows
334 overall lowest backscatter values and a surprisingly strong backscatter increase for beam angles above 40°,
335 particularly at 400 kHz frequency. This effect is less pronounced in May.

4 DISCUSSION

336 ### 4.1 Application of multifrequency data

337 The combination of remote sensing and in-situ sampling is complementary. Due to different spatial
338 scales available for interpretation (Turner et al., 2003) it allows a more complete view on benthic habitats.
339 Onshore, the use of remote sensing became increasingly sophisticated over the past decade, ranging from
340 the application of optical spectral signatures for direct detection of species composition (tree types, forest
341 types, wetland vegetation types) to indirect approaches such as measuring Chlorophyll and obtaining
342 information on habitat structure (Turner et al., 2003; Schulte to Bühne and Pettorelli, 2018). Even onshore,
343 specific species and habitats require specific approaches regarding the type and processing of remote
344 sensing data (Yokoya et al., 2017; Wang and Gamon, 2019). Onshore-developed remote sensing techniques
345 are expanded to the shallow coastal areas by investigating spectral reflectance of seagrass and marine

59

346 algae (Thorhaug et al., 2007). For instance, Kuhwald et al. (2021) developed a method to map seagrass
347 in the turbid waters of the Baltic Sea based on Sentinel-2 data. Such methods are naturally limited by
348 the optical penetration depth, but can be extended for deeper waters by acoustic methods, and be used
349 to identify benthic communities (Kloser et al., 2010). However, despite the usefulness of multifrequency
350 data for acoustic remote sensing (Costa, 2019), the catalogue of the multispectral acoustic reflectance of
351 marine habitats is still very limited (Menandro et al., 2022; Fakiris et al., 2019), especially considering the
352 effects of benthic life and seasonality. The backscatter difference plot (Figure 5) shows that improving the
353 temporal resolution by including the middle month of August in the analysis results in added value when
354 interested in the habitats' seasonal dynamics. Therefore, a catalogue of acoustic reflectance requires the
355 consideration of seasonality and ideally the use of calibrated systems or establishment of reference sites
356 (although relative measures not relying on absolute backscatter values are explored (Lamarche et al., 2011))
357 to allow comparisons between different survey areas and instruments (Roche et al., 2018; Weber et al.,
358 2018). Multispectral approaches are also important because seasonal differences in the investigation sites
359 may not be related to changes in average monofrequency backscatter intensity (which may be below the
360 effects of line azimuth and short term variability (Lurton et al., 2018; Montereale-Gavazzi et al., 2019), but
361 to changes in the response of different frequencies and angular response. Despite intense ground truthing,
362 it was not possible to relate all the information in the multifrequency mosaics to actual conditions on
363 the seafloor. However, the multifrequency backscatter approach discriminates not only between habitats,
364 but also reveals small-scale changes within a single habitat. The individual habitats are discussed in the
365 following.

4.2 Seagrass meadows

367 The clearest spectral signature in our investigation site is found within the Seagrass facies. The detection
368 of seagrass meadows is of interest for coastal and marine management. This ecologically important habitat
369 acts as nursery ground for fish, coastal protection and carbon sink (Cullen-Unsworth and Unsworth, 2013;
370 Terrados and Borum, 2004), but is also endangered by climate change (Duarte et al., 2018). Seagrass
371 performs photosynthesis and accordingly oxygen bubbles exist in the tissues and lacunae. As gas is a strong
372 acoustic reflector, seagrass, in combination with its canopy height above the seafloor, is well detectable
373 by different acoustic systems using different frequencies (Fakiris et al., 2019). Seagrass meadows have
374 been studied extensively with acoustic methods (Gumusay et al., 2019; Ballard et al., 2020). The prior
375 studies did not consider seasonal changes in the seagrass' acoustic footprint. A characteristic seasonal
376 effect of seagrass is a mean increase of about 1 dB and 2.5 dB between May and August for the angular
377 corrected mosaic details at 200 kHz and 400 kHz, respectively. Changes between August and October are
378 on average smaller (Table 3). Average changes of 2 dB in a backscatter mosaic can be caused both by lines
379 of different azimuth depending on conditions at the seafloor (Lurton et al., 2018) and short term variability
380 of acoustic measurements on sandy sediments (Montereale-Gavazzi et al., 2019). Therefore, it is not the
381 average increase of backscatter intensity in the seagrass area, but the presence of local changes of up to 7
382 dB that represents the most important seasonal effect (Figure 8).

383 The ARC for the Seagrass facies show a strong increase of backscatter values at high angles of incidence
384 ($¿$ 40°). Usually, a decrease in acoustic backscatter at increasing incidence angles is expected for sandy
385 seafloor (Yu et al., 2015). The effect correlates with seagrass density (which is increasing from May to
386 August, Figure 3). ARCs of seagrass meadows reported in previous studies did not show this effect, but
387 it was observed consistently in our investigation (Hasan et al., 2012; Fakiris et al., 2019; De Falco et al.,
388 2010). The backscatter increase at high incidence angles increases with frequency, similar to the effect
389 observed for backscatter intensity in mosaics. We argue that this inversion at higher incidence angles is

390 caused by the acoustic beam travelling through a larger amount of dense seagrass when compared to low
391 incidence angles. Scatter from bubbles in and attached to additional seagrass blades is preserved in the
392 multibeam time series data which covers 0.5 m below and above the bottom detection. The increased
393 sensitivity of the 400 kHz frequency is explained by the size of gas bubbles being closer to the wavelength
394 of the higher frequency (Lurton, 2002). This behavior may be a characteristic feature of dense seagrass
395 meadows, and reduced for decreasing meadow density.

396   The different seasonal response of frequencies in the Seagrass facies is related to different penetration
397 depths. Signals of lower frequencies have a larger penetration depth in sandy environments (von Deimling
398 et al., 2013). At 500 kHz, the penetration in sandy sediment is estimated with 1.2 cm, while 100 kHz
399 frequency penetration is approximately 9 cm (Huff, 2008). The difference in penetration depth can explain
400 the reduced backscatter increase between May and August at 200 kHz frequency compared to 400 kHz
401 (Figure 8). Although only few seagrass leaves were present after the winter storms, the buried rhizomes
402 were still remaining. Those are located closely below the seafloor surface and can include oxygen bubbles
403 (Borum et al., 2007). Therefore, rhizomes are expected to cause increased volume scatter at 200 kHz
404 frequency compared to 400 kHz. The exceptional decrease in backscatter strength from May to August
405 from seagrass patches enclosed by the southeastern reef area (marked in Figure 5) is possibly caused by
406 already high backscatter values in May. Mussel beds typically show higher backscatter values compared to
407 seagrass (Table 3). Seafloor covered by mussels which is overgrown by dense seagrass meadows result in
408 relatively lower backscatter values, because dense seagrass meadows blocks the acoustic response of the
409 substrate it is growing on (Gumusay et al., 2019).

410 4.3   Coarse sand and gravel

411   The characteristic signature of the CSG facies is the increased high-frequency response for gravelly
412 seafloor (Figure 7), readily observed in a subset of ARC curves of coarse sand and gravel seafloor (Figure
413 10). The multifrequency maps are particularly useful for the identification of gravelly seafloor, especially
414 with the inclusion of the (uncalibrated) 700 kHz (Figure 10b). The ratio between the seafloor roughness
415 and wavelength of the acoustic signal increases with frequency. Consequently, the specular component of
416 the incident acoustic signal is decreasing and the spherical scattering in all the directions increases, as the
417 seafloor surface becomes relatively rougher (Lurton, 2002). This explains the almost constant backscatter
418 strength ARC at 700 kHz frequency over all incidence angles (Figure 10a). Additionally, the wavelength at
419 high frequencies is comparable to the sediment grain size (both are a few millimeter), thus additional wave
420 effects, e.g., interference, might occur. The gravelly areas are ecologically valuable habitats, but apparently
421 have a seasonal appearance in the investigation site. The multiseasonal data for the CSG facies (Figure 6)
422 and repeated underwater video footage (Figure 3) indicate dynamic in bedstate and sediment composition,
423 with an increasing amount of coarse sand and gravel fractions and increasing exposure leading to the
424 formation of large-scale ripple structures in August and October. Hydrodynamics at the investigation site
425 form elongated small-scale sediment ripples that change the seafloor roughness (as visible in August,
426 Figures 3h,k). Presumably, similar effects may be present in comparable CSG habitats in the Baltic Sea,
427 and should be the target of further studies.

428   The relative increase of lower frequency sensitivity to areas of fine to medium sand can be explained by
429 an additional contribution of volume scatter (Feldens et al., 2018) due to increased penetration depth as
430 discussed earlier for the Seagrass facies. In the CSG facies, the occurrence of worm casts is associated
431 with fine to medium sands, and can be used as an optical indicator of changes in sediment composition
432 (Longbottom, 1970). It can be assumed that features such as worm casts and worm tubes affect volume

433   scatter, as has been demonstrated in the laboratory (Schulze et al., 2021). However, the effects are so far
434   difficult to quantify for seafloor with low benthic coverage (Schönke et al., 2019). Benthic macrofauna in
435   the CSG facies is low in biomass, abundance and species richness, but a significant amount of blue mussels
436   (*M. edulis*) is found in April and August. They were absent in the grab sample collected in October, but
437   large patches were visible in the video footage, which again emphasizes the limits of point samples in
438   habitats of considerable small scale heterogeneity.

4.4   Reef

440   The average acoustic backscatter is seasonally relatively constant compared to the other investigated
441   facies, with a decrease of 1 dB from May to October at 200 kHz frequency and an increase of 0.3 dB
442   at 400 kHz frequency between May and October, including an intermediate increase of 0.9 dB between
443   May and August (Table 3). A dominating effect on the Reef facies is the presence of *M. edulis* growing
444   attached to stones and boulders. Given that the sediment between mussel clumps and stones (which cannot
445   be individually recognized) is of fine to medium sand composition, the increase of backscatter compared to
446   the CSG and Seagrass facies is at least partially caused by the mussel coverage. This is in line with previous
447   studies reporting increased column scatter caused by the presence of mussels or shell hash (Schulze
448   et al., 2021; Lyons, 2005). Then, the constant backscatter suggests that mussel coverage remained similar
449   throughout the year, while the multifrequency maps (Figure 2b) suggest a constant response of the habitat
450   to all used frequencies. However, an analysis of the relationship between mussel coverage and backscatter
451   intensity is not possible with our dataset. While small-scale changes in backscatter intensity are found
452   for mussel-covered seafloor and changes in mussel abundance are observed in underwater footage, the
453   small-scale heterogeneity does not allow to unambiguously relate underwater video footage displaying
454   mussel abundance to acoustic data.

455   Patches within the reef composed of coarser sand display lower backscatter intensities compared to
456   mussel-covered areas, and the increased difference between high and low frequency indicates the presence
457   of coarser substratum. This is interesting to note, as it is known that *Mytilus edulis* avoids regions of coarser
458   sediment (with the exception of drifting not-attached aggregates of *M. edulis* clumps).

459   A clear change observed in video data is the occurrence of red algae *Polysiphona fucoides* in August.
460   While algae could be identified in acoustic remote sensing in prior studies (Rattray et al., 2009), it was not
461   possible to differentiate the occurrence of *P. fucoides* in August using multifrequency backscatter mosaics
462   in our investigation site. Potentially, the algae could be imaged by water column imaging (Schimel et al.,
463   2020), however, this is beyond the scope of our study.

5   CONCLUSION

464   Backscatter mosaics and angular response curves based on a multi-season multifrequency backscatter
465   survey in the Hohe Düne investigation site (southern Baltic Sea) revealed characteristic spectral features for
466   seagrass as well as coarse sand and gravel habitats. The results complement point-based sampling methods
467   with full-coverage high-resolution data. Seasonal developments of these habitats could be displayed in
468   maps based on acoustic remote sensing. However, limitations in positioning accuracy of point samples still
469   prevent a full understanding of the multispectral signal, especially in areas with high patchiness of habitats
470   and their structuring inhabitants, which was apparent for a reef habitat in the investigation site. Additional
471   field studies and controlled laboratory experiments are required to better understand the acoustic impact of
472   benthic life and to interpret the information included in multispectral acoustic information.

CONFLICT OF INTEREST STATEMENT

473 The authors declare that the research was conducted in the absence of any commercial or financial
474 relationships that could be construed as a potential conflict of interest.

AUTHOR CONTRIBUTIONS

475 IS, PF, and MZ contributed to conception and design of the study. IS and MG were responsible for the field
476 work. IS led the data analysis, supported by the other authors (MG, PF, MS, MZ). IS and MG visualized
477 the results. IS and PF wrote the first draft of the manuscript. All authors contributed to manuscript revision,
478 read, and approved the submitted version.

FUNDING

ACKNOWLEDGMENTS

SUPPLEMENTAL DATA

487 Supplemental data includes additional details on the biological community analysis. Table S1 provides a
488 detailed account of species counts. Figure S1 gives details on biomass in the investigation site, while Figure
489 S2 reports the results of the community analysis. Figure S3 provides information on seasonal changes of
490 species in the reef habitat.

DATA AVAILABILITY STATEMENT

491 All data is stored on dedicated servers of the Leibniz Institute for Baltic Sea Research Warnemünde. The
492 raw data supporting the conclusions of this article will be made available by the authors, without undue
493 reservation.

494   The raw multibeam echo sounder datasets analyzed for this study are currently uploaded to
495 the Zenodo archive. The respective dois are: 10.5281/zenodo.6594143 (October 2019, 700 kHz),
496 10.5281/zenodo.6594837 (August 2019, 700 kHz), 10.5281/zenodo.6594850 (October 2019, 400 kHz),
497 10.5281/zenodo.6594854 (October 2019, 200 kHz), 10.5281/zenodo.6594858 (August 2019, 400 kHz),
498 10.5281/zenodo.6594867 (August 2019, 200 kHz), 10.5281/zenodo.6594874 (May 2019, 400 kHz),
499 10.5281/zenodo.6594882 (May 2019, 200 kHz).

REFERENCES

Ballard, M. S., Lee, K. M., Sagers, J. D., Venegas, G. R., McNeese, A. R., Wilson, P. S., et al. (2020). Application of acoustical remote sensing techniques for ecosystem monitoring of a seagrass meadow. *The Journal of the Acoustical Society of America* 147, 2002–2019

Borum, J., Sand-Jensen, K., Binzer, T., Pedersen, O., and Greve, T. M. (2007). Oxygen movement in seagrasses. In *Seagrasses: biology, ecologyand conservation* (Springer). 255–270

Brown, C. J., Beaudoin, J., Brissette, M., and Gazzola, V. (2019). enMultispectral Multibeam Echo Sounder Backscatter as a Tool for Improved Seafloor Characterization. *Geosciences* 9, 126. doi:10.3390/geosciences9030126

Caress, D. W. and Chayes, D. N. (1996). Improved processing of hydrosweep ds multibeam data on the r/v maurice ewing. *Marine Geophysical Researches* 18, 631–650

[Dataset] Caress, D. W. and Chayes, D. N. (2017). MB-System: Mapping the Seafloor

Clarke, J. E. H. (2015). Multispectral acoustic backscatter from multibeam, improved classification potential. In *Proceedings of the United States Hydrographic Conference, San Diego, CA, USA*. 15–19

Clarke, K. and Gorley, R. (2015). Getting started with primer v7. *PRIMER-E: Plymouth, Plymouth Marine Laboratory* 20

Costa, B. (2019). Multispectral acoustic backscatter: How useful is it for marine habitat mapping and management? *Journal of Coastal Research* 35, 1062–1079

Cullen-Unsworth, L. and Unsworth, R. (2013). Seagrass meadows, ecosystem services, and sustainability. *Environment: Science and policy for sustainable development* 55, 14–28

Czechowska, K., Feldens, P., Tuya, F., Cosme de Esteban, M., Espino, F., Haroun, R., et al. (2020). Testing side-scan sonar and multibeam echosounder to study black coral gardens: a case study from macaronesia. *Remote Sensing* 12, 3244

Darr, A., Gogina, M., and Zettler, M. L. (2014). enFunctional changes in benthic communities along a salinity gradient– a western Baltic case study. *Journal of Sea Research* 85, 315–324. doi:10.1016/j.seares.2013.06.003

Dartnell, P. and Gardner, J. V. (2004). Predicting seafloor facies from multibeam bathymetry and backscatter data. *Photogrammetric Engineering & Remote Sensing* 70, 1081–1091

De Falco, G., Tonielli, R., Di Martino, G., Innangi, S., Simeone, S., and Parnum, I. M. (2010). Relationships between multibeam backscatter, sediment grain size and posidonia oceanica seagrass distribution. *Continental Shelf Research* 30, 1941–1950

Duarte, B., Martins, I., Rosa, R., Matos, A. R., Roleda, M. Y., Reusch, T. B., et al. (2018). Climate change impacts on seagrass meadows and macroalgal forests: an integrative perspective on acclimation and adaptation potential. *Frontiers in Marine Science* 5, 190

Dufrêne, M. and Legendre, P. (1997). Species assemblages and indicator species: the need for a flexible asymmetrical approach. *Ecological monographs* 67, 345–366

Fakiris, E., Blondel, P., Papatheodorou, G., Christodoulou, D., Dimas, X., Georgiou, N., et al. (2019). Multi-frequency, multi-sonar mapping of shallow habitats—efficacy and management implications in the national marine park of zakynthos, greece. *Remote Sensing* 11, 461

Feldens, P., Schulze, I., Papenmeier, S., Schönke, M., and Schneider von Deimling, J. (2018). enImproved Interpretation of Marine Sedimentary Environments Using Multi-Frequency Multibeam Backscatter Data. *Geosciences* 8, 214. doi:10.3390/geosciences8060214

Foote, K. G., Hanlon, R. T., Iampietro, P. J., and Kvitek, R. G. (2006). Acoustic detection and quantification of benthic egg beds of the squid loligo opalescens in monterey bay, california. *The Journal of the Acoustical Society of America* 119, 844–856

544   Gaida, T. C., Tengku Ali, T. A., Snellen, M., Amiri-Simkooei, A., van Dijk, T. A. G. P., and Simons, D. G.
545   (2018). enA Multispectral Bayesian Classification Method for Increased Acoustic Discrimination of
546   Seabed Sediments Using Multi-Frequency Multibeam Backscatter Data. *Geosciences* 8, 455. doi:10.
547   3390/geosciences8120455

548   Gogina, M., Zettler, A., and Zettler, M. L. (2022). Weight-to-weight conversion factors for benthic
549   macrofauna: recent measurements from the baltic and the north seas. *Earth System Science Data* 14,
550   1–4. doi:10.5194/essd-14-1-2022

551   Gumusay, M. U., Bakirman, T., Tuney Kizilkaya, I., and Aykut, N. O. (2019). A review of seagrass
552   detection, mapping and monitoring applications using acoustic systems. *European Journal of Remote*
553   *Sensing* 52, 1–29

554   Hasan, R. C., Ierodiaconou, D., and Laurenson, L. (2012). Combining angular response classification and
555   backscatter imagery segmentation for benthic biological habitat mapping. *Estuarine, Coastal and Shelf*
556   *Science* 97, 1–9

557   Heinrich, C., Feldens, P., and Schwarzer, K. (2017). Highly dynamic biological seabed alterations
558   revealed by side scan sonar tracking of lanice conchilega beds offshore the island of sylt (german bight).
559   *Geo-Marine Letters* 37, 289–303

560   Held, P. and Schneider von Deimling, J. (2019). New feature classes for acoustic habitat mapping—a
561   multibeam echosounder point cloud analysis for mapping submerged aquatic vegetation (sav).
562   *Geosciences* 9, 235

563   Hellequin, L., Boucher, J.-M., and Lurton, X. (2003). Processing of high-frequency multibeam echo
564   sounder data for seafloor characterization. *IEEE Journal of Oceanic Engineering* 28, 78–89

565   Huff, L. C. (2008). Acoustic remote sensing as a tool for habitat mapping in alaska waters. *Marine Habitat*
566   *Mapping Technology for Alaska; Reynolds, JR, Greene, HG, Eds* , 29–46

567   Janowski, L., Trzcinska, K., Tegowski, J., Kruss, A., Rucinska-Zjadacz, M., and Pocwiardowski, P. (2018).
568   enNearshore Benthic Habitat Mapping Based on Multi-Frequency, Multibeam Echosounder Data Using
569   a Combined Object-Based Approach: A Case Study from the Rowy Site in the Southern Baltic Sea.
570   *Remote Sensing* 10, 1983. doi:10.3390/rs10121983

571   Kloser, R., Penrose, J., and Butler, A. (2010). Multi-beam backscatter measurements used to infer seabed
572   habitats. *Continental Shelf Research* 30, 1772–1782

573   Kruss, A., Tegowski, J., Tatarek, A., Wiktor, J., and Blondel, P. (2017). Spatial distribution of macroalgae
574   along the shores of kongsfjorden (west spitsbergen) using acoustic imaging. *Polish Polar Research* ,
575   205–229

576   Kuhwald, K., Schneider von Deimling, J., Schubert, P., and Oppelt, N. (2021). How can sentinel-2
577   contribute to seagrass mapping in shallow, turbid baltic sea waters? *Remote Sensing in Ecology and*
578   *Conservation*

579   Lamarche, G., Lurton, X., Verdier, A.-L., and Augustin, J.-M. (2011). Quantitative characterisation of
580   seafloor substrate and bedforms using advanced processing of multibeam backscatter—application to
581   cook strait, new zealand. *Continental Shelf Research* 31, S93–S109

582   Laudien, J. and Wahl, M. (1999). Indirect effects of epibiosis on host mortality: seastar predation on
583   differently fouled mussels. *Marine Ecology* 20, 35–47

584   Longbottom, M. (1970). The distribution of arenicola marina (l.) with particular reference to the effects of
585   particle size and organic matter of the sediments. *Journal of Experimental Marine Biology and Ecology*
586   5, 138–157

587   Lurton, X. (2002). *An introduction to underwater acoustics: principles and applications*, vol. 2 (Springer)

588 Lurton, X., Eleftherakis, D., and Augustin, J.-M. (2018). Analysis of seafloor backscatter strength
589   dependence on the survey azimuth using multibeam echosounder data. *Marine Geophysical Research*
590   39, 183–203

591 Lyons, A. P. (2005). The potential impact of shell fragment distributions on high-frequency seafloor
592   backscatter. *IEEE Journal of Oceanic Engineering* 30, 843–851

593 Maggs, C. and Hommersand, M. (1993). Seaweeds of the british isles. volume i. rhodophyta. part 3a.
594   ceramiales. *Natural History Museum, London*

595 Menandro, P. S., Bastos, A. C., Misiuk, B., and Brown, C. J. (2022). Applying a multi-method framework
596   to analyze the multispectral acoustic response of the seafloor. *Frontiers in Remote Sensing* , 29

597 Montereale-Gavazzi, G., Roche, M., Degrendele, K., Lurton, X., Terseleer, N., Baeye, M., et al. (2019).
598   Insights into the short-term tidal variability of multibeam backscatter from field experiments on different
599   seafloor types. *Geosciences* 9, 34

600 Papenmeier, S., Darr, A., Feldens, P., and Michaelis, R. (2020). Hydroacoustic mapping of geogenic hard
601   substrates: Challenges and review of german approaches. *Geosciences* 10, 100

602 Rattray, A., Ierodiaconou, D., Laurenson, L., Burq, S., and Reston, M. (2009). Hydro-acoustic remote
603   sensing of benthic biological communities on the shallow south east australian continental shelf.
604   *Estuarine, Coastal and Shelf Science* 84, 237–245

605 Roberts, D. (2013). labdsv: Ordination and multivariate analysis for ecology. package version 1.7-0. *URL:*
606   *http://cran.r-project.org/web/packages/labdsv*

607 Roche, M., Degrendele, K., Vrignaud, C., Loyer, S., Le Bas, T., Augustin, J.-M., et al. (2018). Control of
608   the repeatability of high frequency multibeam echosounder backscatter by using natural reference areas.
609   *Marine Geophysical Research* 39, 89–104

610 Schiele, K. S., Darr, A., Zettler, M. L., Friedland, R., Tauber, F., von Weber, M., et al. (2015). enBiotope
611   map of the German Baltic Sea. *Marine Pollution Bulletin* 96, 127–135. doi:10.1016/j.marpolbul.2015.
612   05.038

613 Schimel, A. C., Brown, C. J., and Ierodiaconou, D. (2020). Automated filtering of multibeam water-column
614   data to detect relative abundance of giant kelp (macrocystis pyrifera). *Remote Sensing* 12, 1371

615 Schönke, M., Wiesenberg, L., Schulze, I., Wilken, D., Darr, A., Papenmeier, S., et al. (2019). Impact of
616   sparse benthic life on seafloor roughness and high-frequency acoustic scatter. *Geosciences* 9, 454

617 Schulte to Bühne, H. and Pettorelli, N. (2018). Better together: Integrating and fusing multispectral and
618   radar satellite imagery to inform biodiversity monitoring, ecological research and conservation science.
619   *Methods in Ecology and Evolution* 9, 849–865

620 Schulze, I., Wilken, D., Zettler, M. L., Gogina, M., Schönke, M., and Feldens, P. (2021). Laboratory
621   measurements to image endobenthos and bioturbation with a high-frequency 3d seismic lander.
622   *Geosciences* 11, 508

623 Snellen, M., Simons, D. G., and Riethmueller, R. (2008). enHigh frequency scattering measurements
624   for mussel bed characterisation. *The Journal of the Acoustical Society of America* 123, 3627–3627.
625   doi:10.1121/1.2934852

626 Song, Y., Niemeyer, J., Ellmer, W., Soergel, U., and Heipke, C. (2015). Comparison of three airborne laser
627   bathymetry data sets for monitoring the german baltic sea coast. In *Remote Sensing of the Ocean, Sea
628   Ice, Coastal Waters, and Large Water Regions 2015* (SPIE), vol. 9638, 209–217

629 Tauber, F. (2012). Meeresbodensedimente in der deutschen ostsee= seabed sediments in the german baltic
630   sea. *BSH, Bundesamt für Seeschifffahrt und Hydrographie*

631 Terrados, J. and Borum, J. (2004). Why are seagrasses important?-goods and services provided by seagrass
632   meadows. *European seagrasses: an introduction to monitoring and management* , 8–10

633 Thorhaug, A., Richardson, A., and Berlyn, G. (2007). Spectral reflectance of the seagrasses: Thalassia
634   testudinum, halodule wrightii, syringodium filiforme and five marine algae. *International Journal of*
635   *Remote Sensing* 28, 1487–1501
636 Turner, W., Spector, S., Gardiner, N., Fladeland, M., Sterling, E., and Steininger, M. (2003). Remote
637   sensing for biodiversity science and conservation. *Trends in ecology & evolution* 18, 306–314
638 von Deimling, J. S., Weinrebe, W., Tóth, Z., Fossing, H., Endler, R., Rehder, G., et al. (2013). A low
639   frequency multibeam assessment: Spatial mapping of shallow gas by enhanced penetration and angular
640   response anomaly. *Marine and petroleum geology* 44, 217–222
641 Wang, R. and Gamon, J. A. (2019). Remote sensing of terrestrial plant biodiversity. *Remote Sensing of*
642   *Environment* 231, 111218
643 Weber, T. C., Rice, G., and Smith, M. (2018). Toward a standard line for use in multibeam echo sounder
644   calibration. *Marine Geophysical Research* 39, 75–87
645 Yokoya, N., Grohnfeldt, C., and Chanussot, J. (2017). Hyperspectral and multispectral data fusion: A
646   comparative review of the recent literature. *IEEE Geoscience and Remote Sensing Magazine* 5, 29–56
647 Yu, J., Henrys, S. A., Brown, C., Marsh, I., and Duffy, G. (2015). A combined boundary integral and
648   lambert's law method for modelling multibeam backscatter data from the seafloor. *Continental Shelf*
649   *Research* 103, 60–69

FIGURE CAPTIONS AND TABLES

Table 1. Minimum and maximum backscatter intensities used in the Hohe Düne investigation area mosaics, and the absorption values used for the different months.

Frequency [kHz]	200 calibrated	400 calibrated	550 uncalibrated	700 uncalibrated
Backscatter min/max [dB]	-55/-35	-47/-27	-64/-44	-75/-55
Absorption May [dB/km]	29	68	-	-
Absorption August [dB/km]	27	61	96	141
Absorption October [dB/km]	30	69	113	170
Bandwidth [kHz]	80	80	80	80
Pulse length [µs]	200	200	200	200

Table 2. Percentages of gravel, coarse sand, medium sand, fine sand and silt and clay in sediments of different facies. The same stations were sampled in different seasons. Position of the geological samples are indicated in Figure 2a.

ID	Facies	Date	Gravel	Coarse Sand	Medium Sand	Fine Sand	Silt and Clay
HD01	Seagrass	2019_08	0.0	0.0	14.9	84.5	0.6
HD02	Seagrass	2019_04	0.0	0.3	25.2	73.5	1.0
HD02	Seagrass	2019_08	0.0	2.1	35.0	62.5	0.5
HD05	Seagrass	2019_04	0.0	0.0	12.3	87.5	0.2
HD05	Seagrass	2019_08	0.0	0.0	11.2	88.7	0.2
HD09	Seagrass	2019_04	0.0	1.8	51.2	46.9	0.1
HD09	Seagrass	2019_08	0.0	0.7	50.7	48.6	0.0
HD10	CSG/Seagrass	2019_04	0.0	1.0	62.4	36.0	0.6
HD10	CSG/Seagrass	2019_08	0.0	2.9	72.9	23.5	0.7
HD08	CSG	2019_11	4.5	27.5	60.1	7.9	0.0
HD13	CSG	2019_04	1.0	16.0	66.9	15.7	0.4
HD14	CSG	2019_04	0.0	18.1	69.8	11.8	0.3
HD14	CSG	2019_08	0.0	0.5	52.2	47.3	0.0
HD16	CSG	2019_04	0.0	2.0	33.3	64.7	0.0
HD16	CSG	2019_08	25.8	46.7	18.4	11.1	0.1
HD16	CSG	2019_11	24.2	33.6	34.0	8.1	0.1
HD12	CSG	2019_04	0.0	1.6	49.5	48.9	0.0
HD12	CSG/Reef	2019_08	20.0	28.4	48.3	4.6	0.0
HD12	CSG/Reef	2019_11	14.3	37.2	46.2	4.4	0.1
HD04	Reef	2019_04	7.4	14.3	43.4	34.3	0.5
HD04	Reef	2019_08	0.0	1.2	67.7	30.4	0.8
HD07	Reef	2019_04	7.7	6.6	46.9	38.3	0.4
HD15	Reef	2019_08	rock	6 cm diameter			

Table 3. Average backscatter (standard deviation) [dB]

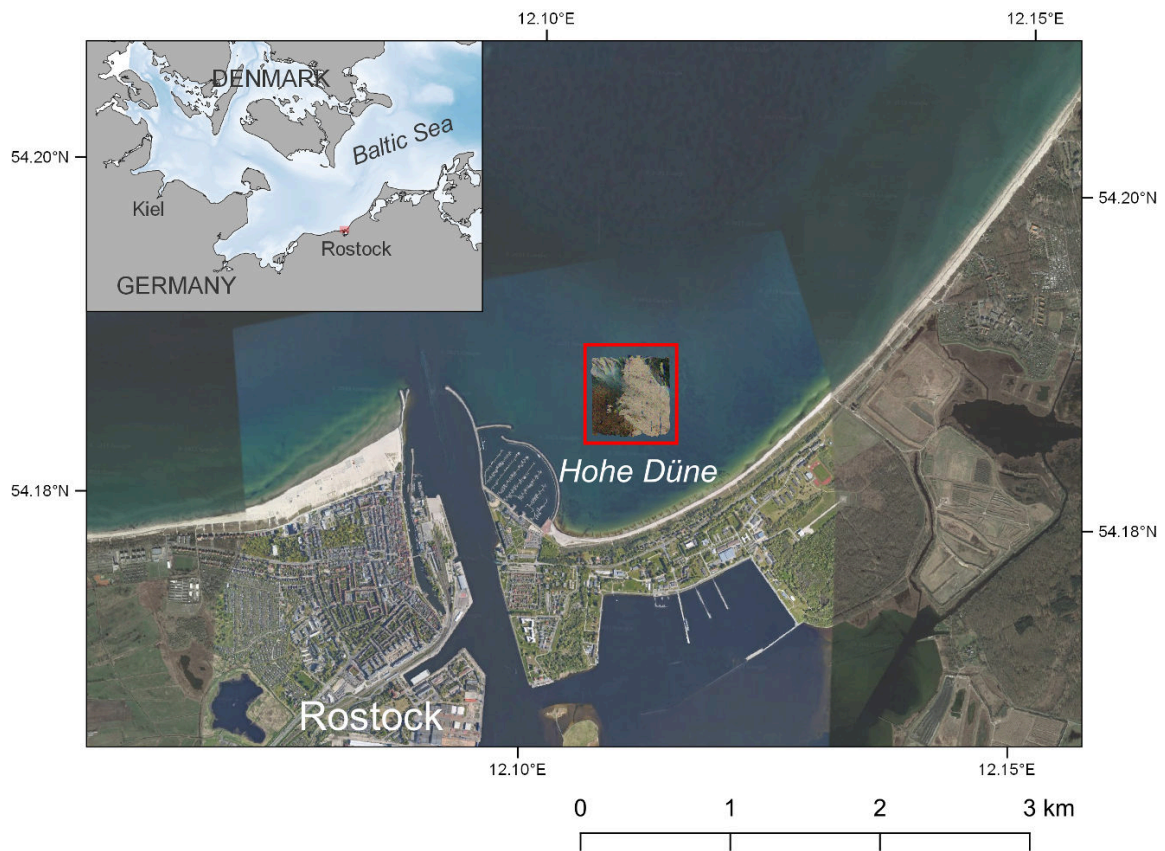| Month	Reef	CSG	Seagrass
200 kHz (calibrated)			
May	-41.9 (1.9)	-47.0 (3.6)	-49.2 (1.9)
August	-42.8 (1.8)	-48.2 (3.6)	-48.3 (2.5)
October	-42.9 (1.8)	-47.3 (3.5)	-48.3 (2.1)
400 kHz (calibrated)			
May	-36.0 (1.9)	-39.1 (3.3)	-43.4 (2.0)
August	-35.1 (1.7)	-38.9 (3.1)	-40.9 (2.1)
October	-35.7 (2.3)	-39.1 (3.6)	-41.5 (2.6)

Figure 1. Location of the Hohe Düne research area close to the coast of Rostock in the southwestern Baltic Sea. Map projection is UTM33N WGS84. Background image: Google 2022.
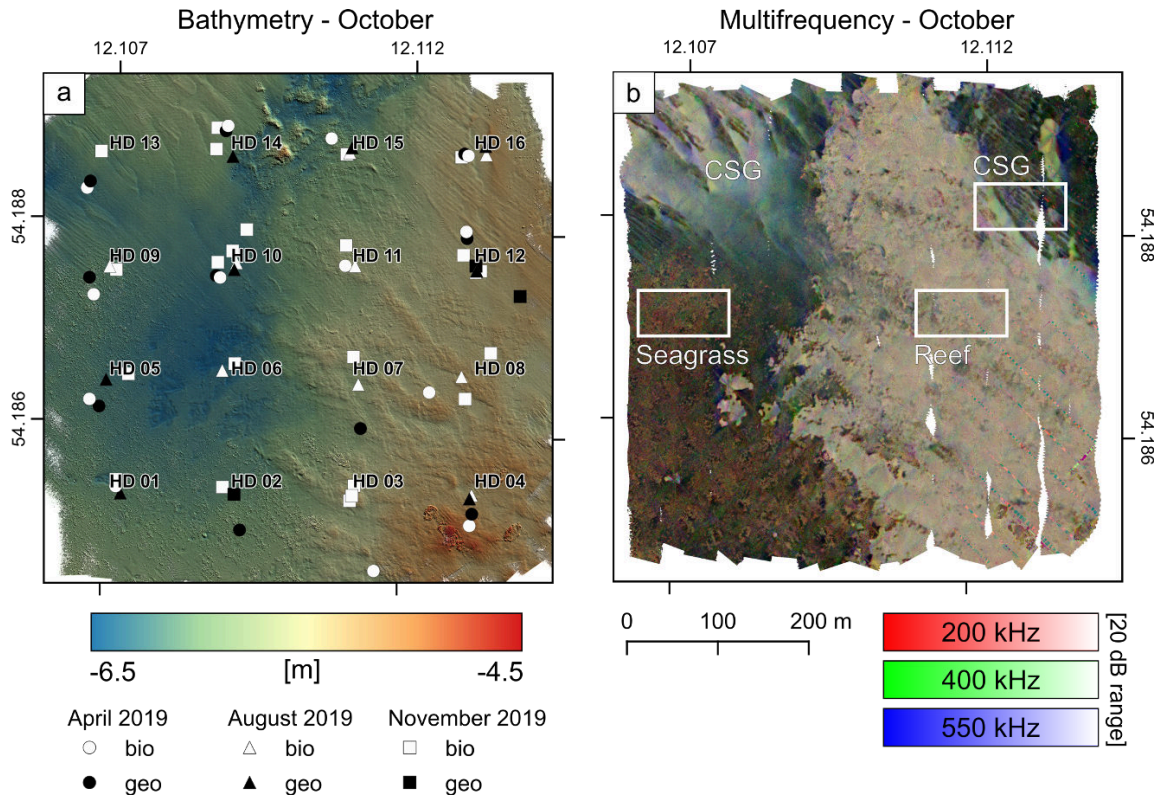
Figure 2. (a) Hillshaded (sun azimuth of 35°, sun elevation of 20°) bathymetry of the working area recorded in October 2019 at 400 kHz frequency. The position of grab samples for biological and sedimentological (Table 2) analysis are indicated around the planned stations (HD01 to HD16). **(b)** Multifrequency backscatter map (200, 400 and 550 kHz) recorded in October 2019. The three identified facies and the positions of detailed views in Figures 4 (Reef), 7 (CSG) and 8 (Seagrass) are indicated. The combination of the backscatter maps of different frequencies using the three channels of a false color image allows for an easy, visible distinction of the present habitats.
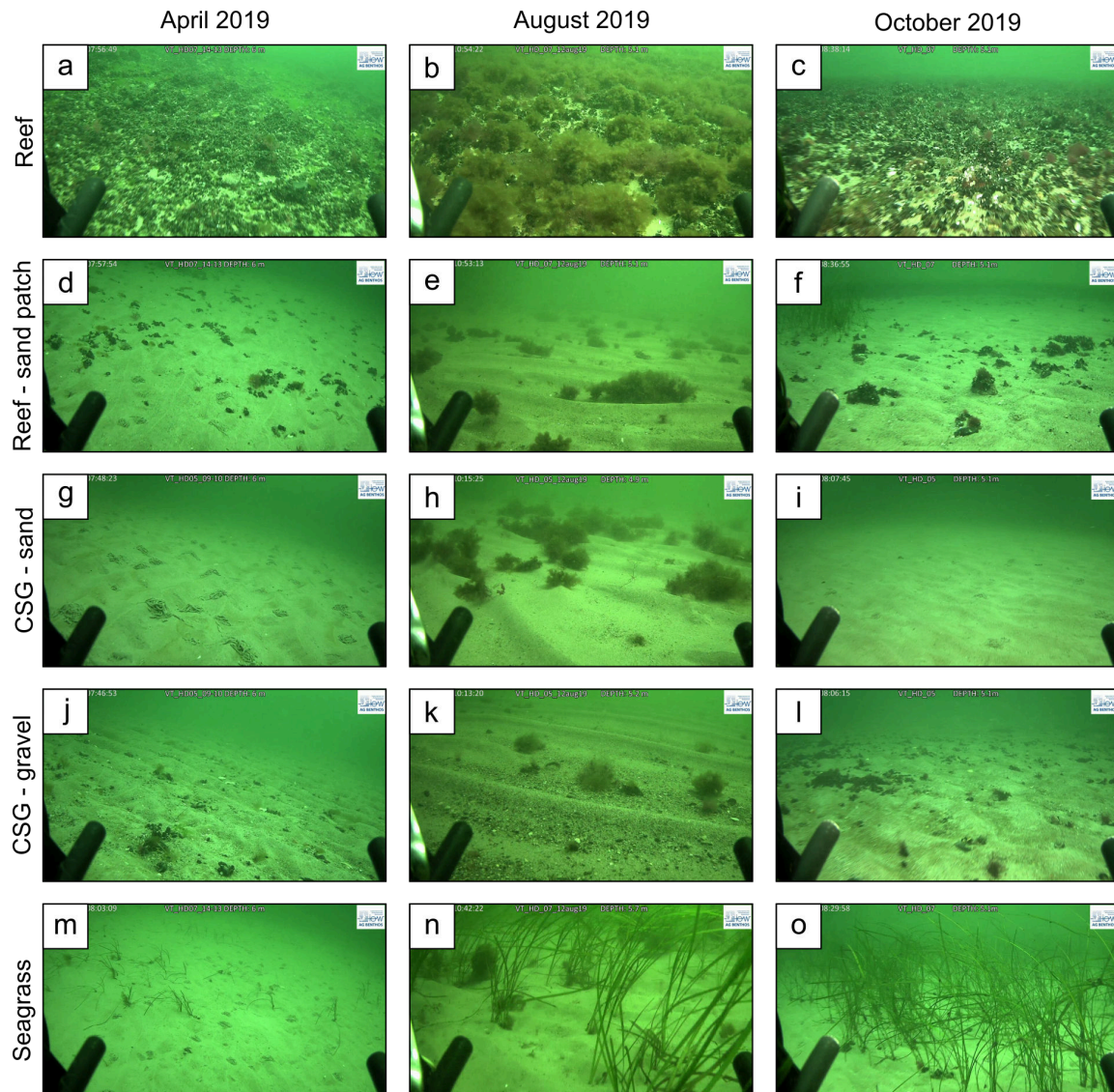
Figure 3. Video stills of the three facies from different months. **(a-f)** The Reef facies is characterized by the stones and boulders, covered by *Mytilus edulis*. In August, red algae grow as a dense layer on top. Sand patches enclosed by the reef occur in NW-SE orientation. The maximum distance between the three photo positions is 1.5 m and 5.5 m for the reef itself and sand patches, respectively, and the locations are shown in Figure 4a. **(g-l)** The CSG facies is characterized by a local change of sandy (g-i) and gravelly (j-l) composition. In April the seafloor is covered by undulating ripples, complemented by worm casts in the sandy parts and loose shells in the gravelly parts. In August, the seafloor surface forms distinct, oriented ripples with loose algae accumulations. In October, the seafloor again shows isolated ripples less pronounced compared to April. In the gravelly areas, shell clusters appear. The maximum distance between the three photo positions is 9.5 m and 7.5 m for the sand and gravel CSG areas, respectively, and the locations are shown in Figure 7a. **(m-o)** The Seagrass facies is characterized by the growth of seagrass patches in the sandy environment. While there are only few blades in April, the density of seagrass canopies observed in August is still present in October. The maximum distance between the three photo positions is 3.5 m and the locations are shown in Figure 8a.
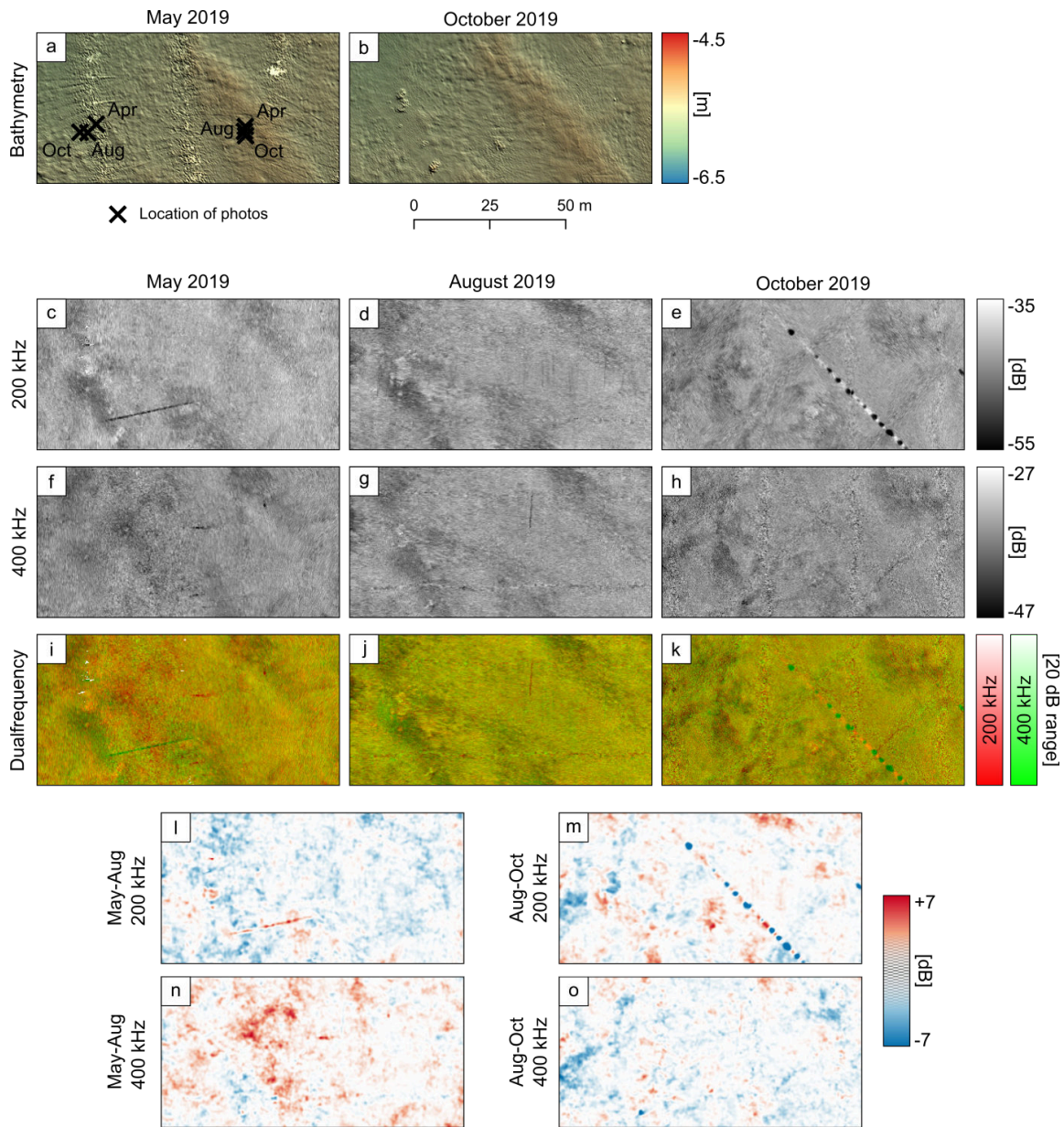
Figure 4. Detailed view of acoustic maps of the Reef facies (for location see Figure 2b). **(a-b)** Bathymetry in May (200 and 400 kHz combined) and October (400 kHz). The resolution is 0.25 m and a hillshade is added with sun azimuth of 35° and sun elevation of 20°. **(c-e)** Backscatter mosaic at 200 kHz frequency for May, August and October 2019. **(f-h)** Backscatter mosaic at 400 kHz frequency for May, August and October 2019. **(i-k)** Dualfrequency backscatter mosaic for May, August and October 2019. The 200 kHz frequency is assigned to the red color channel and 400 kHz assigned to the green color channel. **(l-m)** Difference plots of the 200 kHz backscatter mosaics with a 5 cell lowpass filter showing the change between May to August (l) and August to October (m). **(n-o)** Difference plots of the 400 kHz backscatter mosaics with a 5 cell lowpass filter showing the change between May to August (n) and August to October (o).

72

Figure 5. Difference plots of acoustic backscatter between May, August and October, with a 5 cell lowpass filter. Red color corresponds to an increase in backscatter strength, blue color is a decrease in backscatter strength. The center of the color map is transparent to highlight only relevant differences. The backscatter map in the background was recorded in May (a,b), August (c,d) and October (e,f). The circles mark seagrass patches enclosed by the reef showing a reversed seasonal backscatter difference.

73
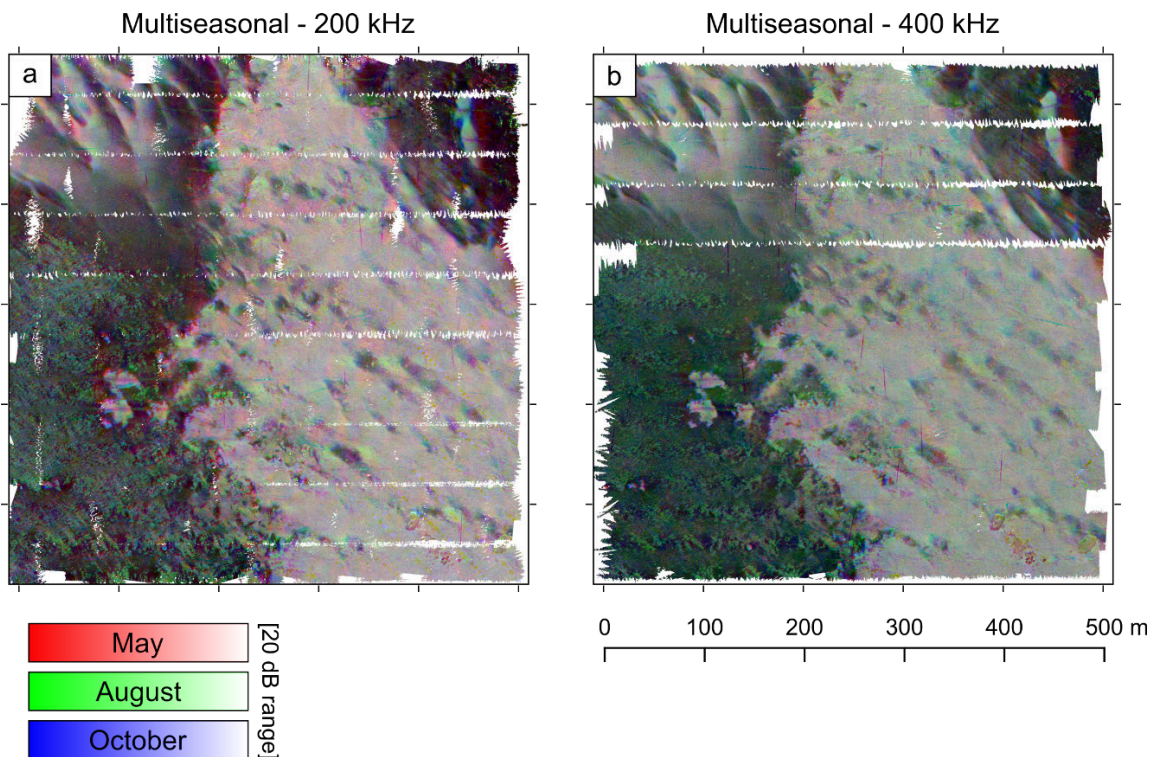
Figure 6. Multiseasonal backscatter maps, where the RGB channels of the false color images are assigned to the backscatter maps of the month May, August and October, respectively. **(a)** 200 kHz frequency. The CSG facies is characterized by the change of dark colors, indicating generally low backscatter values, and brighter stripes, which vary in color, assumed to be caused by hydrodynamically induced shifts in sediment composition. Besides the low-backscatter stripes, the Reef facies appears in a bright reddish color, indicating generally high backscatter values with a maximum in May. The Seagrass facies is dominated by the cloudy seagrass patches in green-turquoise colors based on high backscatter values in August and October. **(b)** 400 kHz frequency. The Reef facies appears in a bright greyish color, representing only small differences between the months compared to 200 kHz.
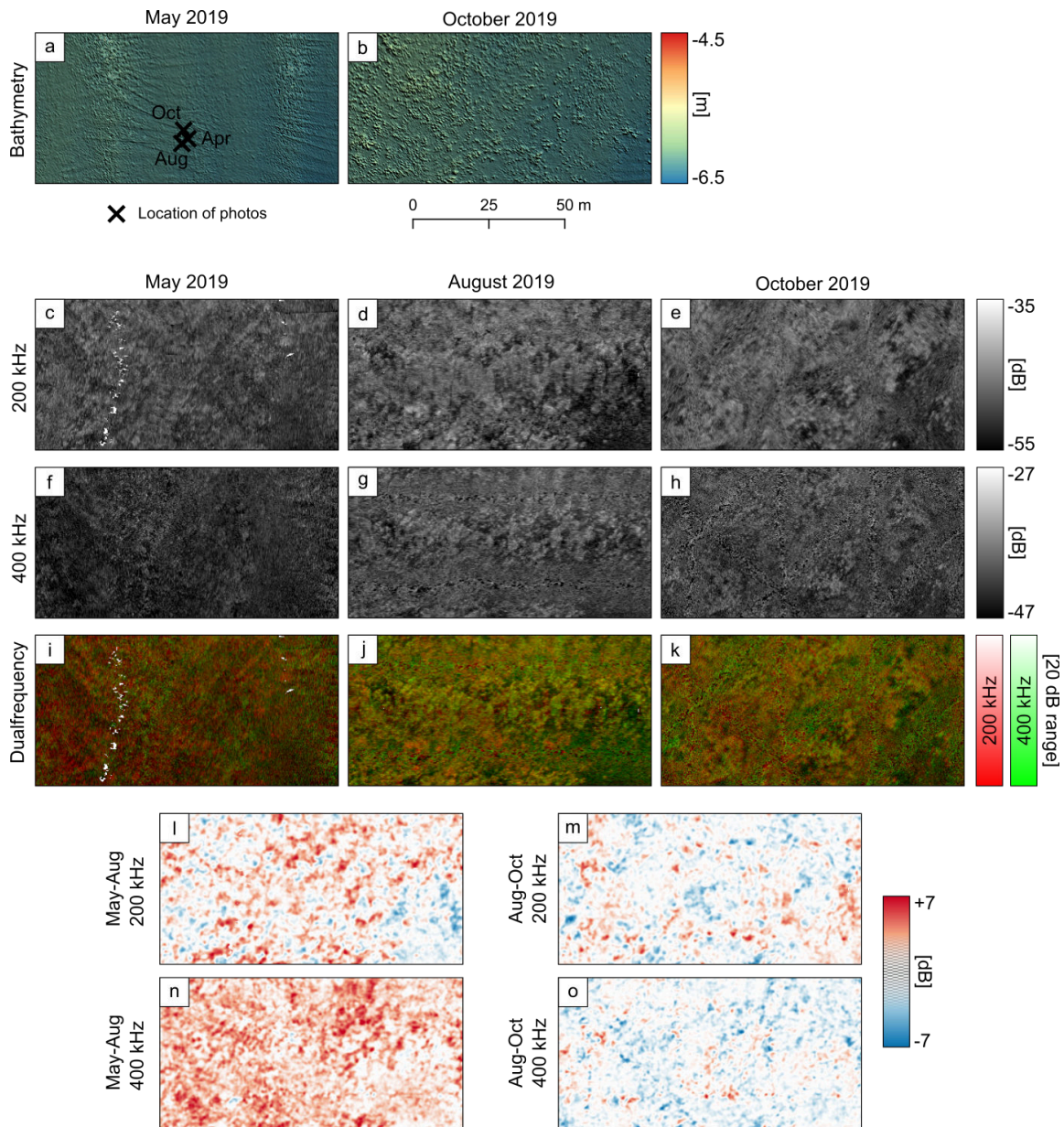
74
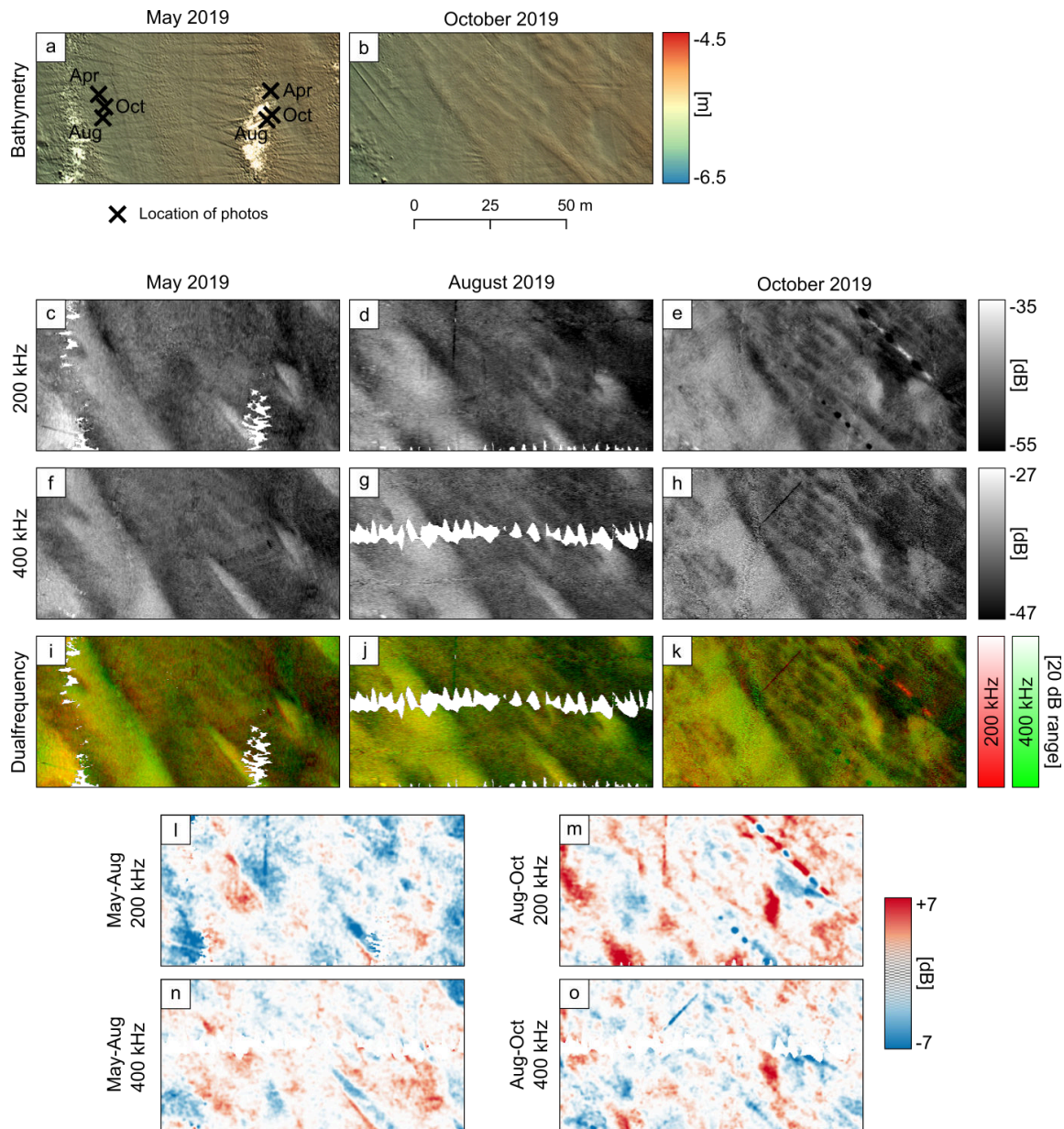
Figure 7. Detailed view of acoustic maps of the CSG facies (for location see Figure 2b). **(a-b)** Bathymetry in May (200 and 400 kHz combined) and October (400 kHz). The resolution is 0.25 m and a hillshade is added with sun azimuth of 35°and sun elevation of 20°. **(c-e)** Backscatter mosaic at 200 kHz frequency for May, August and October 2019. **(f-h)** Backscatter mosaic at 400 kHz frequency for May, August and October 2019. **(i-k)** Dualfrequency backscatter mosaic for May, August and October 2019. The 200 kHz frequency is assigned to the red color channel and 400 kHz assigned to the green color channel. **(l-m)** Difference plots of the 200 kHz backscatter mosaics with a 5 cell lowpass filter showing the change between May to August (l) and August to October (m). **(n-o)** Difference plots of the 400 kHz backscatter mosaics with a 5 cell lowpass filter showing the change between May to August (n) and August to October (o).

75

Figure 8. Detailed view of acoustic maps of the Seagrass facies (for location see Figure 2b). **(a-b)** Bathymetry in May (200 and 400 kHz combined) and October (400 kHz). The resolution is 0.25 m and a hillshade is added with sun azimuth of 35°and sun elevation of 20°. In May, the seafloor appears smooth (besides artefacts), while in October many elevated seagrass patches are visible. **(c-e)** Backscatter mosaic at 200 kHz frequency for May, August and October 2019. **(f-h)** Backscatter mosaic at 400 kHz frequency for May, August and October 2019. **(i-k)** Dualfrequency backscatter mosaic for May, August and October 2019. The 200 kHz frequency is assigned to the red color channel and 400 kHz assigned to the green color channel. **(l-m)** Difference plots of the 200 kHz backscatter mosaics with a 5 cell lowpass filter showing the change between May to August (l) and August to October (m). **(n-o)** Difference plots of the 400 kHz backscatter mosaics with a 5 cell lowpass filter showing the change between May to August (n) and August to October (o).

76
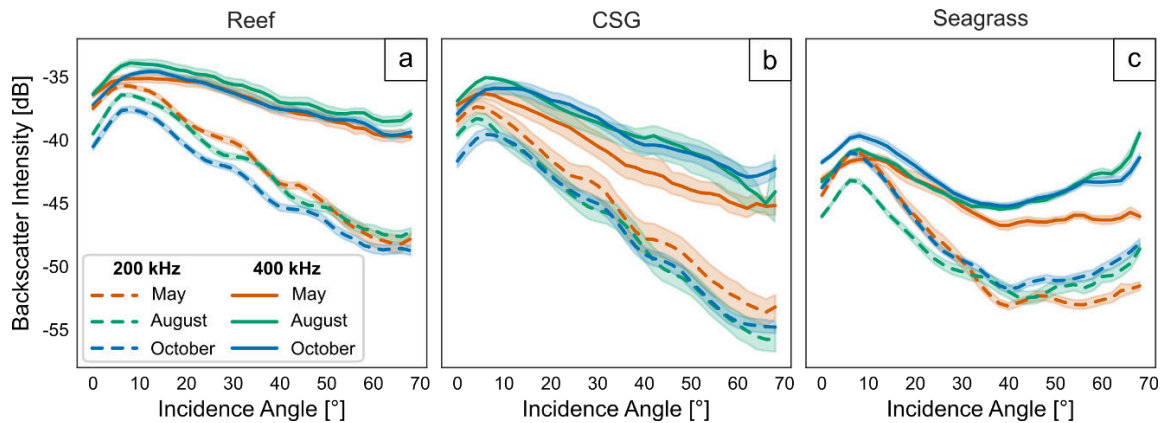
Figure 9. Angular range curves (ARCs) at 200 kHz and 400 kHz frequency for the three facies and three month. Data are extracted from the respective facies details presented before (see Figure 2b for locations). A 95%-confidence interval was added to the curves.
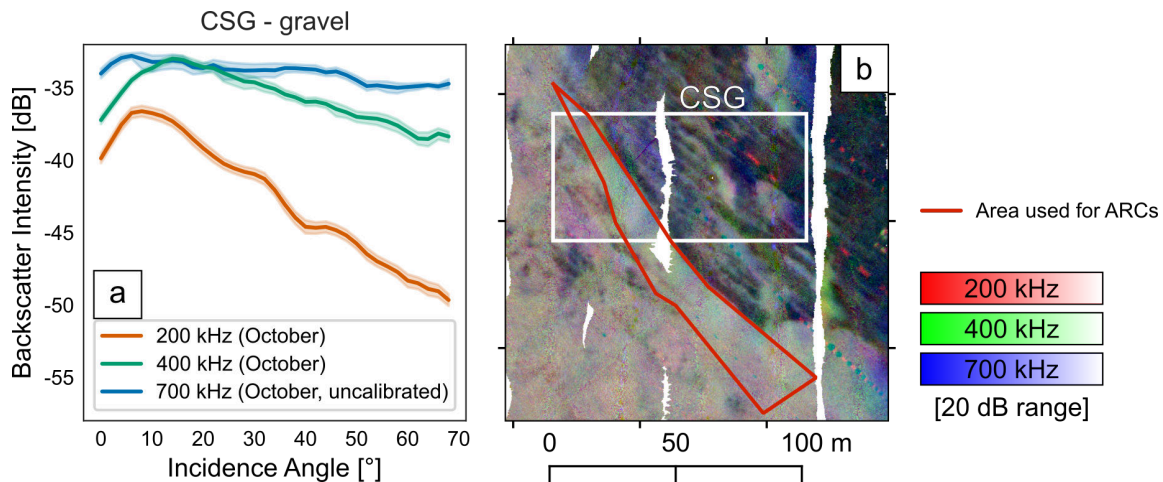

Figure 10. (a) Angular range curves (ARCs) at 200, 400 and 700 kHz frequency (October) for a gravelly area within the CSG facies. A 95%-confidence interval was added to the curves. The uncalibrated backscatter values of the 700 kHz frequency allow only for a relative comparison. **(b)** The exact area used for the ARCs is outlined in red. The multifrequency backscatter map (200, 400, 700 kHz) in the background shows the transition from the Reef to CSG facies in October. The NW-SE orientated ripple occurring in October are prominently visible as bright bluish colors surrounded by dark colors.

77

Supplementary Material

1   SUPPLEMENTARY TABLES AND FIGURES

Table S1: List of taxa recorded in the defined habitats per sampling campaign and respective frequency of occurrence (empty cell indicates absence).

Group	Taxa	Seagrass			Reef			CSG			transfer		
		Apr	Aug	Oct	Apr	Aug	Oct	Apr	Aug	Oct	Apr	Aug	Oct
	N stations	4	4	4	6	7	8	2	2	2	4	5	5
Amphipoda	*Ampithoe rubricata*		25		17		38						20
Amphipoda	*Bathyporeia pilosa*	25						50			25	20	
Amphipoda	*Calliopius laeviusculus*					14							
Amphipoda	*Gammarus*		25			29						20	
Amphipoda	*Gammarus inaequicauda*										25		
Amphipoda	*Gammarus locusta*		25			43					25	20	
Amphipoda	*Gammarus oceanicus*										25		
Amphipoda	*Gammarus salinus*		50		83	86	63		50		25	60	20
Amphipoda	*Gammarus zaddachi*						13				25		
Amphipoda	*Grandidierella japonica*		25			14	13		50				
Amphipoda	*Melita palmata*		25		17		38				25		
Amphipoda	*Microdeutopus gryllotalpa*		50	25	100	86	75				25	60	20
Amphipoda	*Monocorophium insidiosum*						13						
Arachnida	*Halacaridae*				17	29	38				25	20	20
Bivalvia	*Cerastoderma edule*					14							
Bivalvia	*Cerastoderma glaucum*	50	100	100		29	25		50	100		60	40
Bivalvia	*Limecola balthica*	100	100	100			13				50	40	40
Bivalvia	*Mya arenaria*	100	100	100		71	100		100	50	75	100	60
Bivalvia	*Mytilus edulis*	100	50	75	100	100	100	50	100		100	60	80
Bivalvia	*Parvicardium pinnulatum*					14	50						
Bryozoa	*Alcyonidium polyoum*				33								
Bryozoa	*Calliopora lineata*				17								
Bryozoa	*Einhornia crustulenta*	25		25	17					25	25		
Bryozoa	*Electra pilosa*				33								20
Cirripedia	*Amphibalanus improvisus*		25		100	29	100				25	40	20

2

Table S1: List of taxa recorded in the defined habitats per sampling campaign and respective frequency of occurrence (empty cell indicates absence).

Group	Taxa	Seagrass Apr	Seagrass Aug	Seagrass Oct	Reef Apr	Reef Aug	Reef Oct	CSG Apr	CSG Aug	CSG Oct	transfer Apr	transfer Aug	transfer Oct
Cumacea	*Diastylis rathkei*	25									25		
Decapoda	*Carcinus maenas*						13						
Decapoda	*Crangon crangon*			25		29			50			40	
Decapoda	*Rhithropanopeus harrisii*						13						20
Diptera	*Chironomidae*		25			29	13					20	
Echinodermata	*Asterias rubens*						38						20
Gastropoda	*Brachystomia scalaris*				17		75				25		20
Gastropoda	*Ecrobia ventrosa*			25									
Gastropoda	*Hydrobia acuta*									50			
Gastropoda	*Littorina littorea*		25		83	43	50					60	
Gastropoda	*Littorina saxatilis*				83		88						
Gastropoda	*Peringia ulvae*	100	100	100	100	100	100	100	100	100	100	100	100
Gastropoda	*Pusillina inconspicua*		50	50	33	86	100		100		25	60	20
Gastropoda	*Rissoa membranacea*			25	50	14	63						20
Isopoda	*Cyathura carinata*	25			67	29	38				25	20	20
Isopoda	*Idotea balthica*	50	50	50	33	86	75				25	80	20
Isopoda	*Jaera albifrons*		25			14	25				25		
Nemertea	*Lineus ruber*		25			29							
Oligochaeta	*Enchytraeidae*	25							50	50	25	20	
Oligochaeta	*Tubificinae*	100	25	100		29	50	50	100	50	75	20	60
Platyhelminthes	*Platyhelminthes*				50		25				25		
Polychaeta	*Alitta succinea*				100		25				25		20
Polychaeta	*Arenicola marina*			75		14	13			100			80
Polychaeta	*Capitella capitata*							50	100	50			40
Polychaeta	*Dipolydora quadrilobata*							50					
Polychaeta	*Eteone longa*						13						20

80

Table S1: List of taxa recorded in the defined habitats per sampling campaign and respective frequency of occurrence (empty cell indicates absence).

Group	Taxa	Seagrass			Reef			CSG			transfer		
		Apr	Aug	Oct	Apr	Aug	Oct	Apr	Aug	Oct	Apr	Aug	Oct
Polychaeta	*Fabricia stellaris*				17	14							
Polychaeta	*Harmothoe impar*										25		
Polychaeta	*Hediste diversicolor*	100	100	100		43	13	100	100	50	75	100	60
Polychaeta	*Marenzelleria neglecta*		25										
Polychaeta	*Marenzelleria viridis*	75	25	50				50			50	40	
Polychaeta	*Nereididae*						25						
Polychaeta	*Ophelia rathkei*								50			20	
Polychaeta	*Paraonis fulgens*							50	50		75		40
Polychaeta	*Polydora cornuta*	25			50		75				25		40
Polychaeta	*Pygospio elegans*	100	100	100	100	71	38	100	100	50	100	80	60
Polychaeta	*Scoloplos armiger*												20
Polychaeta	*Streblospio shrubsolii*	75	25		17		13						20
Polychaeta	*Travisia forbesii*	75									25		20
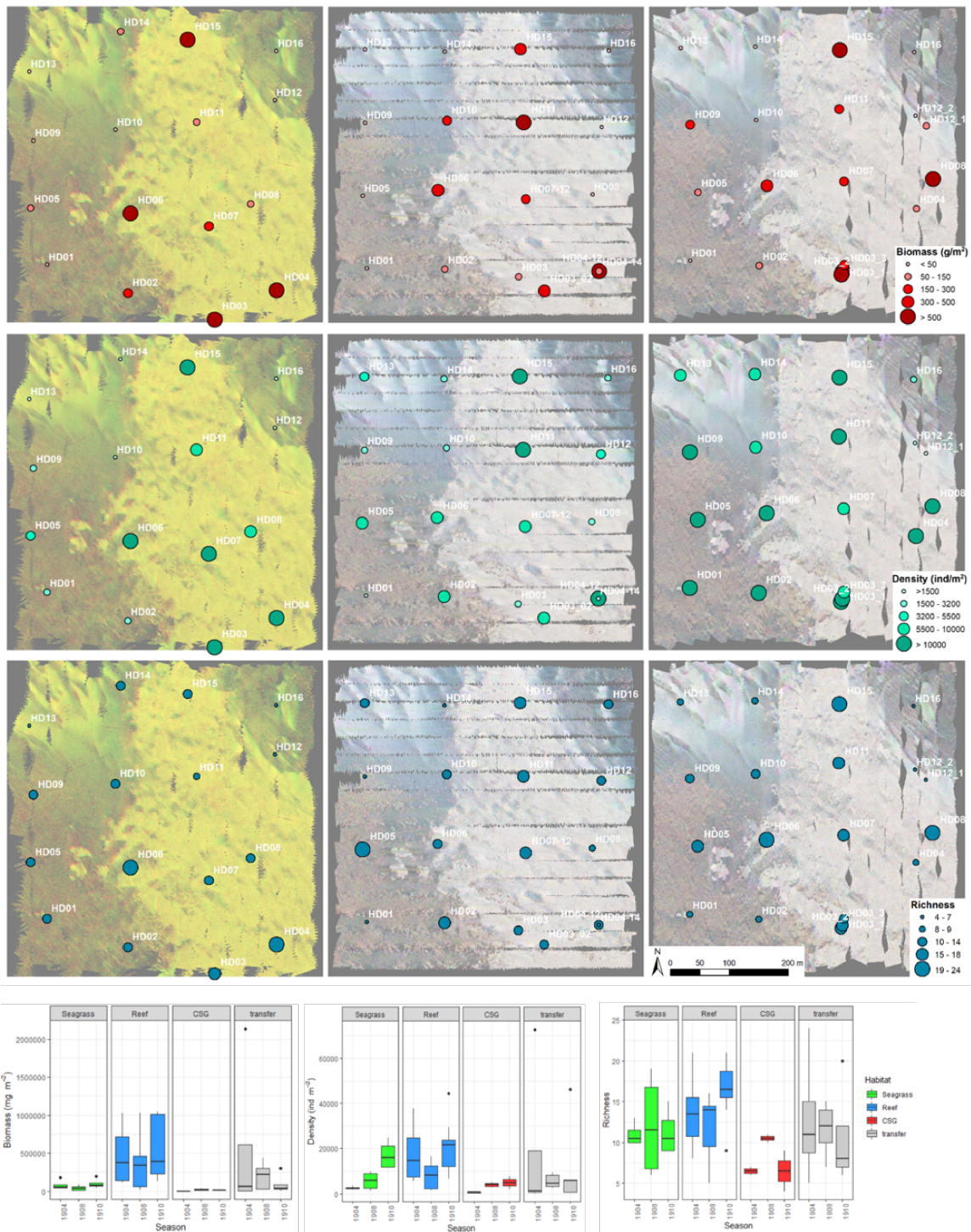
Figure S1. Biomass, density and species richness in the three season.

82
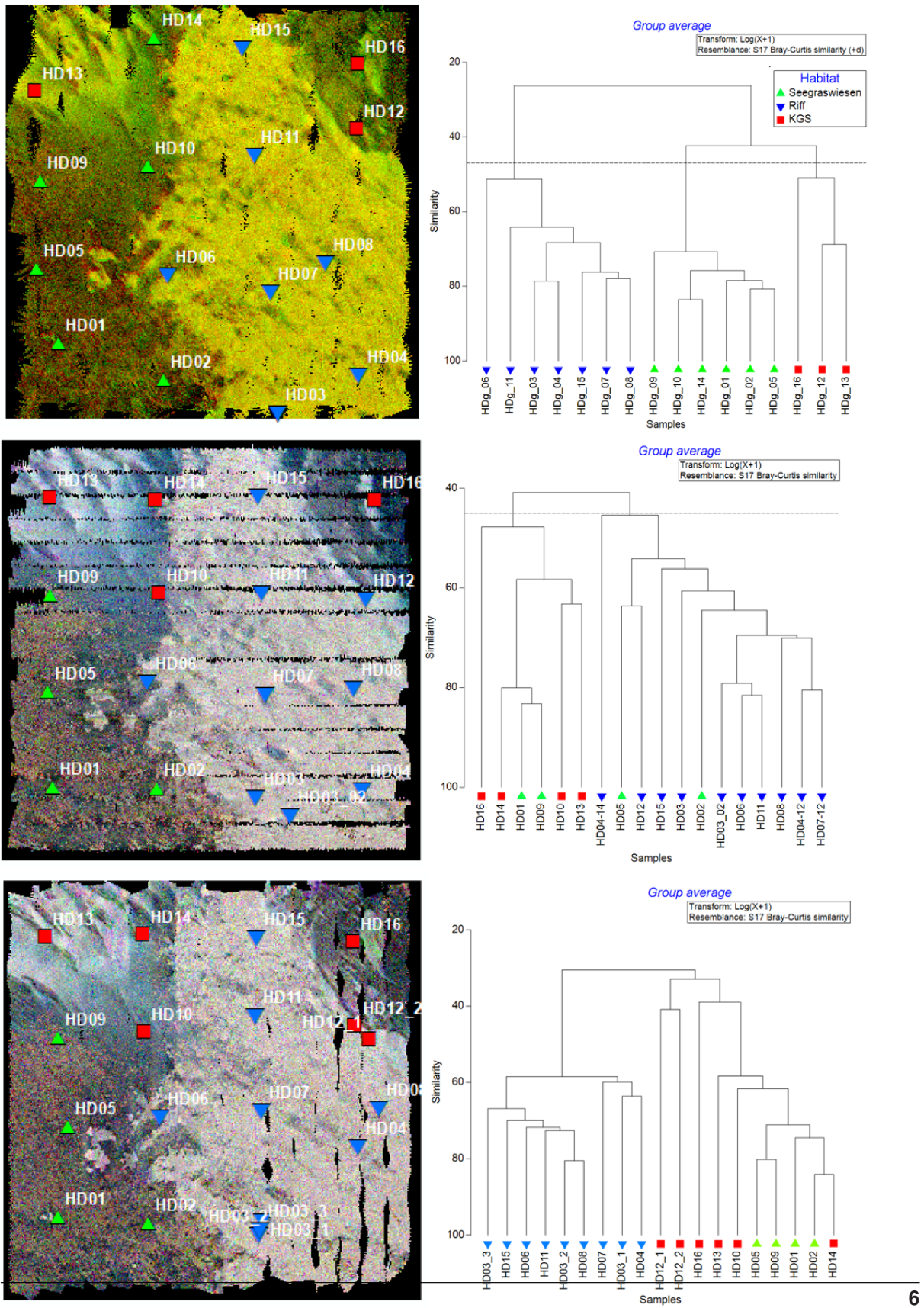
Figure S2. Community structure in the three seasons.
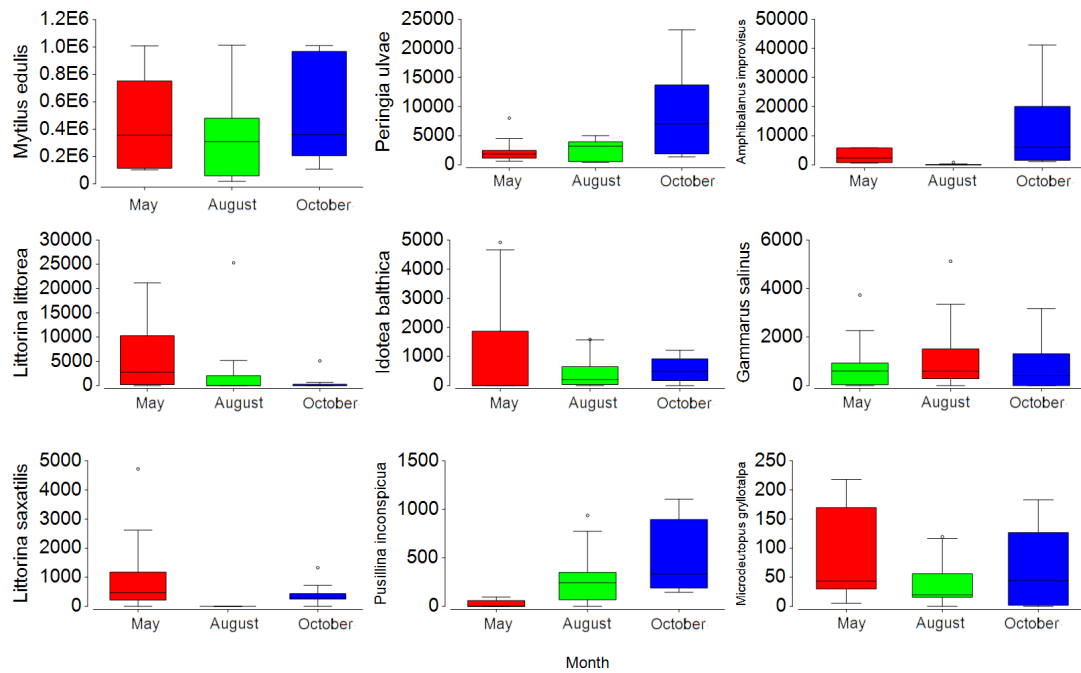
Figure S3. Seasonal changes in the wet weight biomass mg/m^2 of selected benthic macrofauna species at stations attributed to the Reef habitat. Different colors correspond to different seasons. Noteable is the increase of *Amphibalanus improvisus* biomass from summer to autumn.

Paper III
Laboratory Measurements to Image Endobenthos and Bioturbation with a High-Frequency 3D Seismic Lander

Article

Laboratory Measurements to Image Endobenthos and Bioturbation with a High-Frequency 3D Seismic Lander

Inken Schulze [1,*], **Dennis Wilken** [2], **Michael L. Zettler** [1], **Mayya Gogina** [1], **Mischa Schönke** [1] **and Peter Feldens** [1]

1   Leibniz Institute for Baltic Sea Research Warnemünde, 18119 Rostock, Germany; michael.zettler@io-warnemuende.de (M.L.Z.); mayya.gogina@io-warnemuende.de (M.G.); mischa.schoenke@io-warnemuende.de (M.S.); peter.feldens@io-warnemuende.de (P.F.)
2   Institute of Geosciences, Christian-Albrechts-Universität zu Kiel, 24118 Kiel, Germany; dennis.wilken@ifg.uni-kiel.de
*   Correspondence: inken.schulze@io-warnemuende.de

Abstract: The presented 3D seismic system operates three transducers (130 kHz) from a stationary lander and allows non-destructive imaging of small-scale objects within the top decimeters of silty sediments, covering a surface area of 0.2 m^2. In laboratory experiments, samples such as shells, stones, and gummy worms of varied sizes (down to approx. 1 cm diameter) could be located in the 3D seismic cube to a depth of more than 20 cm and differentiated by a reflected amplitude intensity and spatial orientation. In addition, simulated bioturbation structures could be imaged. In a practical application, the system allows to determine the abundance of endobenthos and its dynamic in muddy deposits in-situ and thus identify the intensity of local bioturbation.

1. Introduction

Benthic organisms change the seafloor in diverse ways to adjust it to their habitat demands. They can infiltrate the seafloor to a variable depth and create structures of short-term (e.g., burrows, [1]) and long-term existence (e.g., shell fragments, [2]). Most benthic macrofauna lives in the uppermost 10 cm of the subsurface [3], and active bioturbation is strongest in this depth interval. By reworking the sediment, bioturbation is a key process in exchange processes at the water-sediment interface [4].

The physical sampling of macrofauna is conducted by invasive methods, using various kinds of grabs, dredges, and corers in sedimentary habitats [5,6]. For quantitative macrofaunal analysis, material recovered by grabs is sieved, and most information on the spatial arrangement is lost. For cores, the vertical resolution is controlled by the scaling of potential subsamples, while information on the horizontal arrangement is mostly lost. Further disturbances from before taking a core until transportation to the laboratory and handling there are summarized by [7]. Resin casts and in situ sediment profile imaging can resolve the spatial structure of the endobenthos [8,9]. However, both methods disturb the seafloor habitat and capture only small areas. Extracting sediment and transport to the laboratory is also necessary for X-radiography [10] and CT scans [11–13]. Besides invasive sampling methods, imaging techniques are a valuable tool to investigate benthic organisms. Technological improvements in recent years make camera equipment of high-resolution applicable in marine environments [14]. In situ imaging of epibenthos is conducted using video techniques and software for image analysis and classification [15,16]. For endobenthos, optical imaging methods allow only indirect detection, e.g., in the form of burrow casts and pits [17].

Hydroacoustic surveys by multibeam echo sounders and side-scan sonar aim to measure the bathymetry and the backscatter strength of the seafloor [18]. Backscatter maps

mostly correlate to abiotic seafloor properties such as sediment grain size [19]. However, recent developments aim to derive biotic parameters from acoustic data [20–25]. The backscatter level depends, besides the physical seafloor properties itself, on the incidence angle and frequency of the acoustic wave. It includes scatter at the seafloor-water interface and a volume scatter part as the acoustic wave propagates into the subsurface. Buried objects, including endobenthos, impact volume scatter [2,10]. Besides surface scatter, volume backscatter can become the major contributor to the backscatter strength [26], but hydroacoustic surveys cannot easily detect individual objects contributing to volume scatter. Meanwhile, non-destructive acoustic remote sensing is an actively developing field of research that allows the establishment of time series, e.g., to investigate seasonal changes.

3D reflection seismic systems designed to study the subsurface increased in the resolution during the last decades [27,28]. Now they range from industrial standards with mile-long streamers to small, individual 3D sub-bottom profiling systems with a decimeter resolution. The latter systems are sufficient for the detection of objects in a decimeter scale for special engineering or archeological surveys [29–31]. However, even very high-resolution 3D seismic systems cannot resolve the cm-scale structures, e.g., of biological origin. In principle, the detection of buried, cm-sized objects by high-frequency acoustic transducers in the upper decimeters of a sediment substrate is possible. Objects of previous investigations included, e.g., gas bubbles of up to 6 mm diameter down to 6 cm sediment depth targeted at 1.0–2.27 MHz [32], clams and artificial worm tubes targeted at 1.6 MHz along with 2D profiles with a horizontal resolution of 20 mm [33], clams buried in glass beads of different size investigating the effect of grain size on the signal at 1 MHz [34], lotus roots with a diameter of 2.5–3 cm at 100 kHz [35], including seasonal monitoring [36], the effect of artificial burrows and worm tubes on sound speed and attenuation at 100–400 kHz [37], artificial cylinders as a substitute for telecommunications cables targeted with a 75 kHz sweep at sample spacing of 2–5 cm [38], and trawl marks targeted with a parametric array of 40 transducers at 30–300 kHz [39]. If applied to biological and biogeochemical studies, these non-invasive methods minimize the risk of relocating endobenthic structures during measurement, prevent disturbance during transportation, and preserve unstable sediment surfaces. In addition, they allow surveying a larger number of stations, which is important given the high spatial heterogeneity in shallow-water sedimentary settings.

In this proof-of-concept laboratory study, we evaluate if a stationary high frequency 3D seismic system with three 130 kHz acoustic transducers can detect cm-scale structures and bioturbation traces in marine mud.

2. Materials and Methods

2.1. 3D Seismic Lander System

Three identical, uncalibrated transducers (type Benthowave 7652, 15° opening angle at −3 dB) are the basic elements of a newly designed 3D seismic system, which was developed to be installed on a seafloor-lander system (Figure 1). The transducers were mounted with a fixed distance of 15 cm to each other and a grazing angle of 90° to the seafloor. Two programmable step motors move the transducer array. The central control unit, an Intel NUC, controls the position of 2 step motors via an USB-RS232 converter and activates the transducer via relay control. An AD/DA converter records the acoustic signal with a sampling rate of 3 MHz. The system was powered by 2 rechargeable batteries and can be mounted to a lander module or mooring, allowing future field studies. In the laboratory experiments, the transducers were operated at a frequency of 130 kHz, generating a signal form of 2 sine periods. Shot points were located on a square 2.5 mm grid, covering a total surface area of 45 cm × 45 cm. At each shot point, 20 repeated measurements were conducted and later stacked to enhance the signal-to-noise ratio. The signal record length was 1500 μs. A delay of 200 μs was required after signal transmission to switch the transducer into the receiving mode. Measuring the entire volume required 2.5 h, resulting in a data set recorded in SEGY format of 5.91 GB.
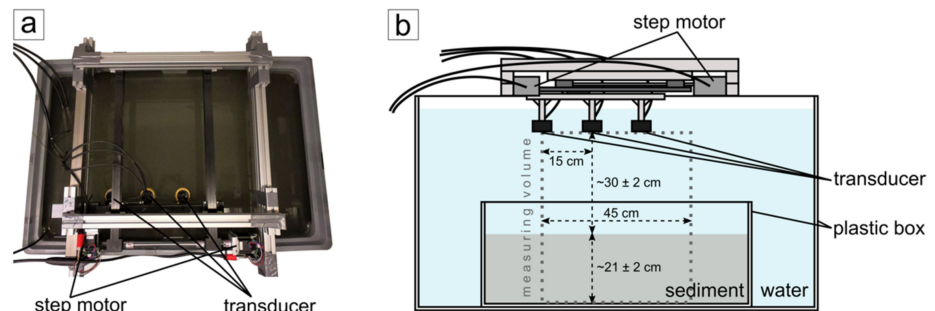
Figure 1. (**a**) Top-down photography of the test tank. The box filled with the substrate is not visible due to suspension in the water column. (**b**) The experimental setup consists of three transducers and two-step motors mounted on top of a water tank. The plastic box containing the buried test object is located 30 cm below the transducers and is filled with a 21 cm thick sediment layer.

2.2. Test Setup

A plastic box with 21 cm thick layer of soft sediments was placed in a plastic tank of ca. 0.6 m^3 (dimensions of the tank were 1.2 × 0.8 × 0.65 m) filled with purified water at a temperature of 17.5 °C for the laboratory experiments. The homogeneous sediment, with a median grain size of around 32 µm in the range of silt, was collected by repeated grab sampling from an offshore basin (Mecklenburg Bay, western Baltic Sea) at approximately 20 m water depth in 2018 and sieved through a 2 mm-mesh size to remove coarse components such as living mussels and shell hash that would have interfered with our experiments. The 3D seismic system was mounted on top of the plastic tank. The transducers were placed at a distance of 30 ± 2 cm to the sediment surface (Figure 1). The system designed to run autonomously from a battery pack was contained in a waterproof housing.

Buried objects of assorted size and material were used in the experimental setups. The objects included single, empty seashells (2.7–3.7 cm diameter), stones (1.0–5.5 cm length), and fruit gummy worms (11.5 cm length, 0.7 cm diameter). The form and size of the gummy worms resembled common annelids, e.g., the lugworm Arenicola marina. Gummy worm length extended to approximately 13 cm and diameter to approximately 1.05 cm after contact with water over a time of 3 h, while density decreased from 1 g/cm^3 to 0.7 g/cm^3. Parameters to describe variations in placement considered during the experiment series included depth below the sediment surface, distance to the next object, vertical overlap of objects, and, in the case of asymmetrical seashells, the orientation of the object. Objects were placed in the inner 30 cm × 30 cm of the measured area. In the case of stones and shells, objects were placed at least one day before measuring to allow the sediment to settle following placement. The measurements involving fruit gummy worms were conducted immediately after the placement to avoid expansion and disintegration. Other setups with no objects included different depths of manual sediment disturbance. Bioturbation of the sediment was simulated either by manual disturbance or by pushing a spatula to various depths into the sediment. In total, we measured 26 different setups over 4 months, during which noticeable compaction of the substrate took place. Sediment resuspension during object exchange with the following deposition outside the sediment box contributed to a decrease in sediment thickness and a slight increase in the distance between transducer and sediment surface.

2.3. Processing

Processing of the seismic data uses functions from the open-source package Seismic Unix [40]. A visualization of the following processing steps is displayed in Figure 2. Processing included the reading of SEGY files, stacking of 20 shots per trace, and cutting the data to 0.68 ms TWT (two-way travel time) in order to remove the box bottom indicated by very high-amplitude reflections. After applying an automatic gain correction to the

traces, a deconvolution (Wiener predictive error filtering) with later bandpass filtering (trapezoidal corner frequencies at 60, 90, 140, 280 kHz) was used to improve the vertical resolution and suppress the effect of reverberation. The dataset was imported to MATLAB by using the function of the open-source package SegyMAT [41]. The traces were padded with zeros from the start of recording to 0.2 ms, and trace normalization was applied. Bulk shifting of one transducer's traces by 2 sample intervals compensated for a small inaccuracy in the construction and ensured the continuous alignment of reflectors. A 3D Stolt migration, assuming a constant sound velocity of 1480 m/s was applied to improve the lateral resolution. Details on the theory and application of the 3D Stolt migration were given by [42]. The theoretical limit of vertical resolution for the experimental setting was 0.28 cm, while the lateral resolution of the seismic data prior to migration was determined by the first Fresnel zone [43], with a radius of ca. 4.1 cm at the sediment surface and decreased after migration of the data. The data cube was exported back to the SEGY format and imported to IHS Kingdom software for visualization.
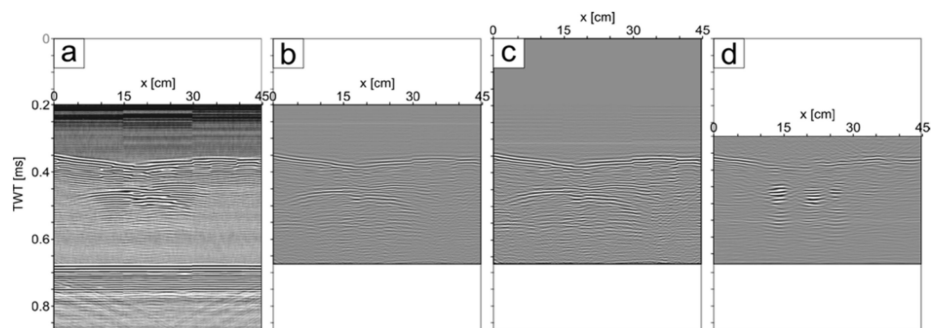

Figure 2. Seismic profile after different processing steps. (**a**) Raw data cut at TWT (two-way travel time) = 0.885 ms (first 0.2 ms not recorded). In x-direction, a tripartite segmentation due to recording with three transducers is noticeable by differences in water column noise and a small trace shift at x = 15 cm and x = 30 cm. (**b**) Cutting the traces at TWT= 0.68 ms removes the reflections of the box bottoms. Gain and bandpass filters are applied to the data, and deconvolution attenuates reverberation effects. (**c**) The initial 0.2 ms of the traces are padded with zeros, and trace normalization is applied. (**d**) Data following 3D migration. Reflections of three shells are visible, starting at TWT = 0.45 ms. Reflections at x = 13 cm and 21 cm are found at the shell's center, while the reflection at x = 26 cm is on a shell's edge. Later figures in this study only show data in the relevant range of TWT = 0.3–0.68 ms.

To measure the reflectivity in a specified zone, the root mean-squared (RMS) amplitude was calculated as the square root of the sum of squared amplitude divided by the number of samples within a specified window. The computation of the RMS amplitude was performed for different time intervals along the traces.

3. Results

All seismic volumes showed a set of strong amplitude reflectors at the sediment surface at about 0.3 m (0.4 ms TWT) below the transducers. Undisturbed sediments showed a continuous, high-amplitude reflector at the sediment surface and a homogeneous, transparent appearance below (Figure 3). In contrast, disturbed sediments showed medium to high-amplitude reflectors at the sediment surface (Figure 3). These reflectors were not continuous. Disrupted low-amplitude reflections were present below the sediment boundary in disturbed sediments. For one experiment setup, distinct parts of the sediment were manually disturbed to different depths. The different disturbance in the sediment was observed in the amplitude data (Figure 3), and vertical conduits existed where the spatula was pushed vertically into the sediment. The conduits were imaged by plots of RMS amplitudes for different time slices (Figure 4e–h). Compared to a largely undisturbed

sediment column, the disturbances affected both mean RMS amplitudes and its standard deviations (Table 1).
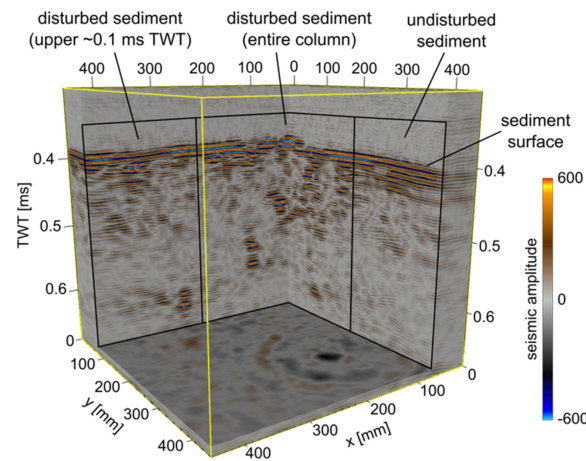

Figure 3. Seismic volume shows the reflections of varying manual disturbances in the soft sediment. Undisturbed sediment (**right**) is characterized by continuous high-amplitude reflectors at the surface and a transparent appearance below. The reflectors of the sediment surface of disturbed parts (**middle** and **left**) show interruptions and variations in amplitude strength. Reflections of disturbed sediment below appear discontinuous, with limits partly sharp, partly fading into transparency with varying strength of amplitude. This pattern ceases below 0.5 ms TWT where only the upper sediment layer was disturbed. To some extent, random reflector fragments appear due to the object exchange from previous experiments.
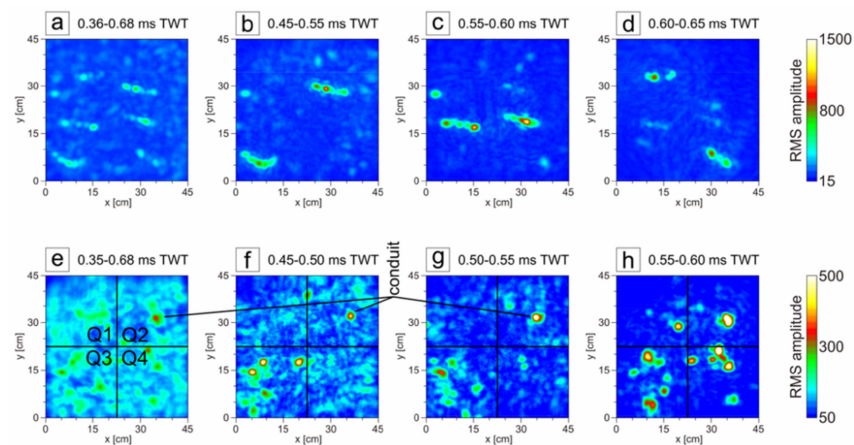

Figure 4. RMS amplitudes are calculated as volume attribute in different depths. (**a–d**) The data cube (Figure 5) includes six fruit gummy worms at different depths. The section including the entire sediment layer (**a**) shows the location and orientation of all six objects and the reflection of the sediment surface. Shorter time sections (**b–d**) allow for a more detailed display of only the two fruit gummy worms in the respective depth. (**e–h**) The data cube (see also Figure 3) is characterized by disturbances of variable extent in the sediment layer. The RMS amplitude, including the entire sediment column (**e**) shows little differences between the four quadrants. Shorter sections of increasing depth (**f–h**) provide a different pattern in the quadrants. Continuously highest amplitudes appear in the lower-left quadrant (Q3), where disturbances affect the entire sediment column. The constant lateral patch of high amplitudes in the upper right quadrant (Q2), marked as conduit, corresponds with the intersection point of the spatula pushes.

Table 1. Mean of RMS amplitude (standard deviation) in all quadrants (Q1–4) of RMS amplitude time slices (Figure 4e–h).

Time Slice [ms TWT]	Q1 (Undisturbed)	Q2 (Spatula Cross)	Q3 (Disturbed)	Q4 (Disturbed < 0.1 ms TWT)
0.35–0.68	123.3 (27.7)	119.5 (32.1)	129.9 (32.2)	128.6 (26.0)
0.45–0.50	91.5 (27.3)	100.5 (35.3)	113.6 (60.3)	99.9 (27.9)
0.50–0.55	70.1 (22.5)	80.1 (43.4)	92.3 (44.2)	67.8 (22.5)
0.55–0.60	56.4 (36.0)	68.2 (61.0)	84.4 (60.6)	75.7 (75.5)

Objects buried in the sediment appear as a sequence of high-amplitude reflections with sharp lateral limits. Sequences of ellipsoidal reflections reflect the locations of fruit gummy worms (Figure 5), while stones (Figure 6) and shells (Figure 7) have a circular reflection pattern. Stones are recognized by high-amplitude reflections, which are compact and symmetrical. In comparison, the reflection pattern of single shells with the outside facing up have a lower amplitude compared to stones of similar size (an example is shown in Figure 8). Shell reflectors are often asymmetrical.

The reflections of each object occurred over an extended time interval exceeding the object's size, and a weaker, narrower reflection followed the first reflector sequence. Therefore, it is difficult to measure the vertical extension and orientation of objects (Figures 6 and 7).

The horizontal extension of the reflector sequences was a better indicator of length or diameter of buried objects for relative comparison. At the same time, absolute values still showed wider deviations from the dimensions of stones and shells measured prior to burial. In case of the fruit gummy worms (Figure 5), the lengths of the reflectors, measured linearly between both ends, showed good agreement with the length measured prior to the experiment. However, a coincidental correction of reflector length is possible due to bends of flexible worms, and the worm diameter of 0.8 cm to 1.0 cm was overestimated in the lateral dimension. The directional orientation of six worms buried horizontally in different depths was accurately imaged and can well be observed in RMS plots (Figure 4).
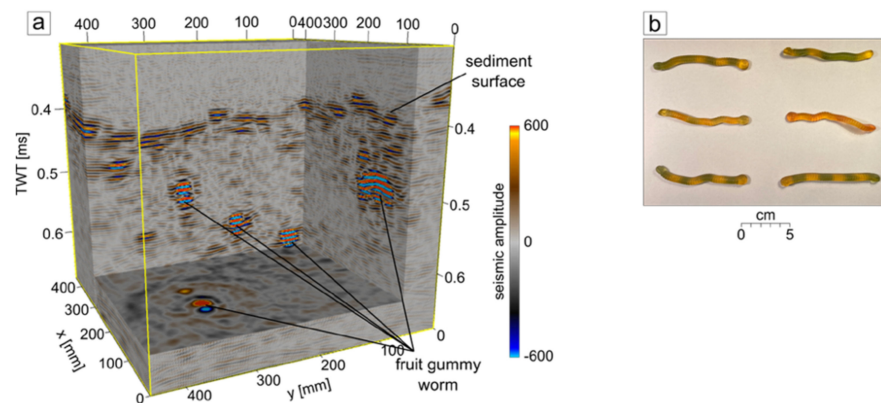

Figure 5. (**a**) Seismic volume showing the reflections of fruit gummy worms in 0.45 to 0.65 ms TWT depth. Five of six gummy worms buried during the experiment are visible. The gummy worm to the right is measured along its long axis. Its vertical extension is measured with 0.02 ms TWT (1.5 cm at 1500 m/s water sound velocity) and its length with 40 shot points (10 cm with 2.5 mm shot point distance). (**b**) Photography of the fruit gummy worms showing the plan view of the configuration they are buried in (the average worm is 11.5 cm in length and 0.7 cm wide). Due to their flexibility, buried worms might show small humps.
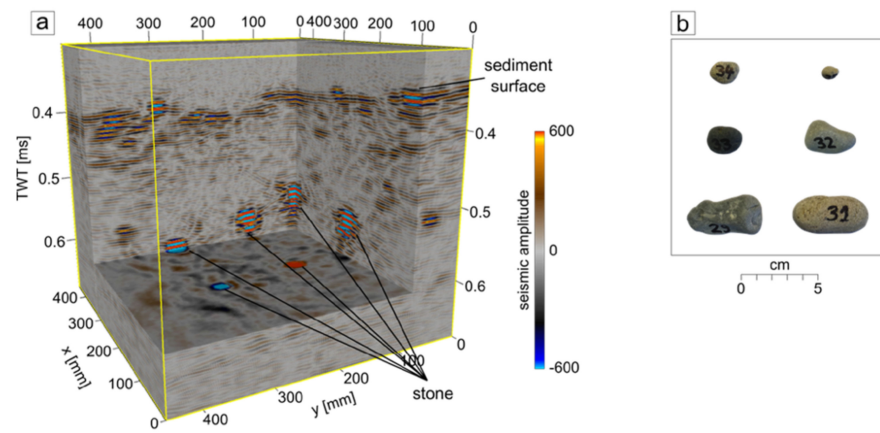
Figure 6. (**a**) Seismic volume showing the appearance of six stones in 0.5 to 0.65 ms TWT depth. All stones appear as high-amplitude reflections, with sharp lateral limits. Initially, all stones were placed in approximately the same depth, but heavier stones subsided. (**b**) Photography of the stones in the schematic configuration they are buried in. The diameters of stones are 1.9 × 1.5 × 0.9 cm and 1.1 × 1.0 × 0.8 cm (**upper row**), 2.3 × 2.8 × 1.6 cm and 3.2 × 2.2 × 1.0 cm (**middle row**), 4.7 × 2.5 × 1.8 cm, and 4.9 × 2.5 × 1.7 cm (**lower row**).
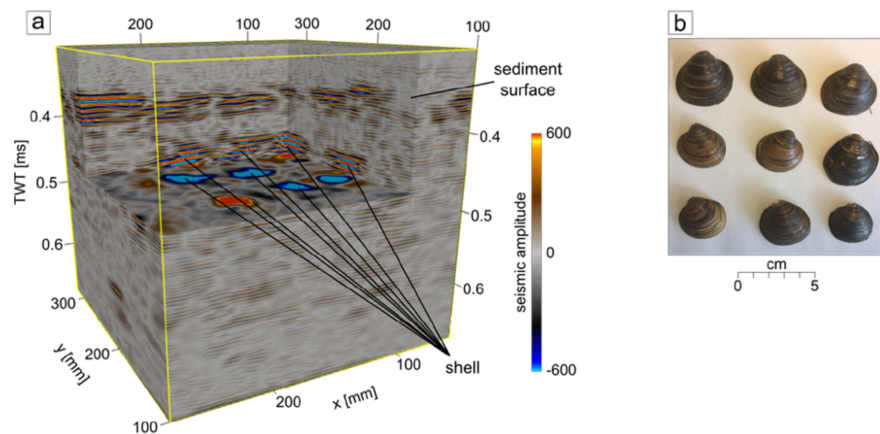

Figure 7. (**a**) Seismic volume showing the reflections of nine shells (of which eight are visible in this section) buried with (center to center) a spacing of 5 cm in 0.42–0.55 ms TWT depth. This setup was left to rest for two months before measuring. The shells appear as high-amplitude reflections below the reflections of the sediment surface. Due to the sharp limits of their reflectors, all shells can be well distinguished. (**b**) Photography of shells in the schematic configuration they are buried in. All shells are of medium size, with a measured length of 2.7 to 3.4 cm, a width of 2.9 to 3.7 cm, and a height of 1.0 to 1.1 cm.
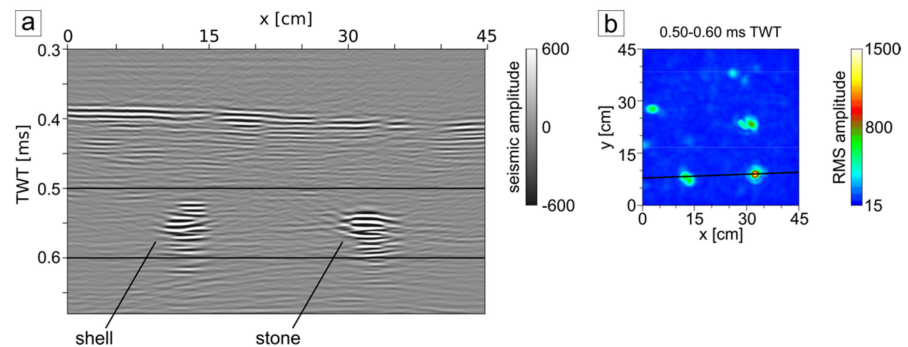
Figure 8. (**a**) Seismic profile showing the reflections of a shell (with outside facing upward) and a stone of comparable size. Amplitudes of the stone reflections are higher than the reflections of the shell, which appears to be more diffuse. The location of the seismic profile is indicated in (**b**). (**b**) RMS amplitudes of the corresponding time range (depth is indicated in (**a**)), showing a much higher amplitude for the stone than for the shell. The diameter measured in the time slice is 2.5–4.0 cm for the shell (2.9 × 3.2 × 1.0 cm), and 3.0–3.4 cm for the stone (3.2 × 2.2 × 1.0 cm).

4. Discussion

The identification of individual buried bivalves is of importance as they act as biodiffusors that have a marked impact on biogeochemical fluxes. However, they are typically found at sediment depths of 4 to 10 cm [3] and thus not easily accessible by optical remote sensing techniques. Mussel shells as small as 1 cm, which was the minimum size of tested objects, could be repeatedly detected with the considered setups. This is sufficient to image species of interest such as *Arctica islandica*, *Abra alba*, *Limecola balthica*, *Mya arenaria*, *Cerastoderma glaucum*, and *Phaxas pellucidus*, which have individual sizes of up to 6.5 cm, 2 cm, 2 cm, 4 cm, 2 cm, and 4 cm, respectively [44]. These species frequently occur in the Baltic Sea basins, which form our target investigation site. The sediment in the basins is composed of silt and clay particles with high organic contents [45], corresponding to our test setup. High-amplitude reflections in all measured seismic cubes image the bottom of the sediment box, the tank bottom, and eventually the air below. Therefore, the penetration depth at 130 kHz is greater than the sediment thickness in the laboratory experiment (21 ± 2 cm), which is sufficient for practical application in fine-grained deposits of Baltic Sea basins. The maximum penetration depth for the experimental setup needs further examination in future field studies. In the experiments, object detection was more difficult in the uppermost centimeters (e.g., Figure 4a,e). The inevitable exchange of object between the measurements causes artifacts in the sediment column, such as conduits, water inclusions, and changes in the sediment surface topography, which appear as noise in seismic imaging. The noise level can reach an amplitude strength similar to some objects' amplitude, and detangling it from the objects of interest remains to be solved.

Next to the direct imaging of endobenthic life, the tracing of bioturbation is of interest. Such activity modifies sediment properties and alters the redistribution of pollutants and biogeochemical fluxes [46]. Burrowing organisms move organic material to the lower part of their burrows and transport oxygen-rich seawater into anoxic zones of the sediment column [3], increasing, for example, oxygen uptake by a factor of 2 [47]. It was not possible to test in the field yet whether bioturbation traces left by the organisms can be detected, and their burrowing mechanisms cannot be reproduced in the laboratory. In nature, bioturbation traces have a wide range of appearances, ranging from U-shaped burrows with 1–2 mm in diameter (Arenicolites) to up to 1 m long, branching structures (Zoophycos) with diameters of up to 20 mm [48]. Imaging the displacement of soft sediments by manually disturbing the substrate and mapping the location of fruit gummy worms with a diameter of less than 1 cm demonstrated that in-situ mapping of some types of bioturbation traces is possible. Again, due to the impact of topography and noise level in the uppermost

centimeters of the sediment, simulated bioturbation traces are better visible towards the center and the base of the seismic cube. The fruit gummy worms could be distinguished from sediment disturbance by higher amplitudes, despite a composition similar to water. It cannot be expected that the results will match those of more sophisticated laboratory techniques such as CT scans [13], but the presented method may allow obtaining repeated in-situ measurements of bioturbation intensity that could not be obtained by common sampling techniques. Table 1 and Figure 4 show that simulated bioturbation traces affect both mean RMS amplitudes and the corresponding standard deviations in time slices where they occur when compared to sequences of largely undisturbed sediment. The disturbed sediments (Table 1, Q3) show on average 25.5% higher values for time slices below the sediment surface compared to undisturbed sediments (Table 1, Q1), but only 5% higher values considering the entire sediment column, including the effects caused by the sediment surface. The fact that this impact is measurable implies that it will be possible to determine the local bioturbation intensity based on high-resolution 3D seismic. For future field studies, a better distinction between bioturbation and other objects in the shallow subsurface is required.

The results of this study suggest that the spatial orientation and location of different objects can be distinguished. Regarding the distinction between objects required, e.g., to determine the bioturbation intensity, stones are generally registered with higher amplitudes in the laboratory setting (Figure 8), with approximately double intensity compared to shells of a similar size. However, the impact of shell orientation on the amplitude strength needs to be considered. In the laboratory experiment, the inside of the valve was placed downwards, while living mussels are often oriented upright with their umbo pointing up (e.g., *Arctica Astarte*, *Cerastoderma*), while others are orientated horizontally (e.g., *Macoma*, *Abra*), and some have a siphon reaching towards the sediment surface (e.g., *Mya*) [44]. This might change the reflection pattern as the edges of the shell show a different echo due to diffraction effects [49]. The soft body parts of the living mussel, enclosed by the shell valves, represent an additional interface for the acoustic signal to interact with. Living mussels filter the water and emit gaseous nitrous oxide [50], which results in additional material interfaces. These interfaces are likely to affect the reflection patterns, hence a differentiation between shells and living mussels might be possible. The amplitude of fruit gummy worms is generally similar to or lower than the amplitude of the shells, but the distinction is possible based on the geometries of the objects that are recognized in the seismic cubes (Figure 4). Some bright spots in the worm's amplitude (Figure 4) might trace back to the air enclosed in the fruit gummy or to small gas bubbles attached to their surface, which could remain as the dissolution of the worms required a short time interval between burial and measurement. Based on the shape and amplitude, a distinction between the fruit gummy worms and simulated bioturbation structures is difficult. For the purpose of deriving an index for bioturbation intensity, i.e., a sort of bioturbation potential, a distinction between the organisms and the traces they leave might, however, not be required. Nevertheless, the differentiation between objects and structures as well as the impact of coarser sediments, remain topics for future work [34]. Reverberations and (to a lesser extent) unknown seismic velocities obstruct qualitative measurements of the vertical size of objects. To improve the vertical resolution and reduce the overestimation of vertical object size, higher bandwidth chirp signals are to be used in future field studies [51]. The assumed constant sound velocity for the 3D Stolt migration also limits the accuracy in the horizontal directions. The interpretation of seismic volumes could further be improved using seismic attributes, which have been employed with great success in the geological interpretation of the 3D seismic data, for example, to recognize faults and chimneys. Albeit obviously of a much larger scale, these features are comparable in structure to the traces left by endobenthic life forms [52].

5. Conclusions

A stationary high-frequency seismic system can locate objects down to 1 cm in size buried in the mud in laboratory conditions. Through the ability to resolve objects in the centimeter range and penetration of at least 20 cm in a fine-grained substrate, the system can complement the ground validation of a ship-based acoustic survey. Potential applications also include (but are not limited to) time-series of bioturbation intensity and mussel abundance and complement to the analysis of sediment cores. Further work will focus on field applications, improvement of object differentiation, and the implementation of different waveforms.

References

1. Von Ziegelmeier, E. Beobachtungen über den Röhrenbau von *Lanice conchilega* (Pallas) im Experiment und am natürlichen Standort. *Helgoländer Wissenschafltiche Meeresunters* **1952**, *IV*, 107–129. [CrossRef]
2. Lyons, A.P. The Potential Impact of Shell Fragment Distributions on High-Frequency Seafloor Backscatter. *IEEE J. Ocean. Eng.* **2005**, *30*, 843–851. [CrossRef]
3. Michaud, E.; Desrosiers, G.; Mermillod-Blondin, F.; Sundby, B.; Stora, G. The functional group approach to bioturbation: II. The effects of the Macoma balthica community on fluxes of nutrients and dissolved organic carbon across the sediment–water interface. *J. Exp. Mar. Biol. Ecol.* **2006**, *337*, 178–189. [CrossRef]
4. Kauppi, L.; Bernard, G.; Bastrop, R.; Norkko, A.; Norkko, J. Increasing densities of an invasive polychaete enhance bioturbation with variable effects on solute fluxes. *Sci. Rep.* **2018**, *8*, 7619. [CrossRef]
5. Eleftheriou, A. *Methods for the Study of Marine Benthos*; John Wiley & Sons: Hoboken, NJ, USA, 2013.
6. Jørgensen, L.L.; Renaud, P.E.; Cochrane, S.K.J. Improving benthic monitoring by combining trawl and grab surveys. *Mar. Pollut. Bull.* **2011**, *62*, 1183–1190. [CrossRef]
7. Dück, Y.; Lorke, A.; Jokiel, C.; Gierse, J. Laboratory and field investigations on freeze and gravity core sampling and assessment of coring disturbances with implications on gas bubble characterization. *Limnol. Oceanogr. Methods* **2019**, *17*, 585–606. [CrossRef]
8. Shinn, E.A. Burrowing in Recent Lime Sediments of Florida and the Bahamas. *J. Paleontol.* **1968**, *42*, 879–894.
9. Rhoads, D.C.; Germano, J.D. Characterization of Organism-Sediment Relations Using Sediment Profile Imaging: An Efficient Method of Remote Ecological Monitoring of the Seafloor (RemotsTM System). *Mar. Ecol. Prog. Ser.* **1982**, *8*, 115–128. [CrossRef]
10. Pouliquen, E.; Lyons, A.P. Backscattering from bioturbated sediments at very high frequency. *IEEE J. Ocean. Eng.* **2002**, *27*, 388–402. [CrossRef]
11. Dufour, S.C.; Desrosiers, G.; Long, B.; Lajeunesse, P.; Gagnoud, M.; Labrie, J.; Archambault, P.; Stora, G. A new method for three-dimensional visualization and quantification of biogenic structures in aquatic sediments using axial tomodensitometry. *Limnol. Oceanogr. Methods* **2005**, *3*, 372–380. [CrossRef]
12. Pennafirme, S.F.; Machado, A.S.; Lima, I.; Suzuki, K.N.; Lopes, R.T. Viability of microcomputed tomography to study tropical marine worm galleries in humid muddy sediments. In Proceedings of the 2013 International Nuclear Atlantic Conference—INAC 2013, Recife, Brazil, 24–29 November 2013.

13. Rosenberg, R.; Grémare, A.; Duchêne, J.C.; Davey, E.; Frank, M. 3D visualization and quantification of marine benthic biogenic structures and particle transport utilizing computer-aided tomography. *Mar. Ecol. Prog. Ser.* **2008**, *363*, 171–182. [CrossRef]

14. Chang, A.; Jung, J.; Um, D.; Yeom, J.; Hanselmann, F. Cost-effective Framework for Rapid Underwater Mapping with Digital Camera and Color Correction Method. *KSCE J. Civ. Eng.* **2019**, *23*, 1776–1785. [CrossRef]

15. Gomes-Pereira, J.N.; Auger, V.; Beisiegel, K.; Benjamin, R.; Bergmann, M.; Bowden, D.; Buhl-Mortensen, P.; De Leo, F.C.; Dionísio, G.; Durden, J.M.; et al. Current and future trends in marine image annotation software. *Prog. Oceanogr.* **2016**, *149*, 106–120. [CrossRef]

16. Beisiegel, K.; Darr, A.; Gogina, M.; Zettler, M.L. Benefits and shortcomings of non-destructive benthic imagery for monitoring hard-bottom habitats. *Mar. Pollut. Bull.* **2017**, *121*, 5–15. [CrossRef] [PubMed]

17. Solan, M.; Germano, J.D.; Rhoads, D.C.; Smith, C.; Michaud, E.; Parry, D.; Wenzhöfer, F.; Kennedy, B.; Henriques, C.; Battle, E.; et al. Towards a greater understanding of pattern, scale and process in marine benthic systems: A picture is worth a thousand worms. *J. Exp. Mar. Biol. Ecol.* **2003**, *285–286*, 313–338. [CrossRef]

18. Brown, C.J.; Smith, S.J.; Lawton, P.; Anderson, J.T. Benthic habitat mapping: A review of progress towards improved understanding of the spatial ecology of the seafloor using acoustic techniques. *Estuar. Coast. Shelf Sci.* **2011**, *92*, 502–520. [CrossRef]

19. Dartnell, P.; Gardner, J.V. Predicting Seafloor Facies from Multibeam Bathymetry and Backscatter Data. *Photogramm. Eng. Remote Sens.* **2004**, *70*, 1081–1091. [CrossRef]

20. Heinrich, C.; Feldens, P.; Schwarzer, K. Highly dynamic biological seabed alterations revealed by side scan sonar tracking of *Lanice conchilega* beds offshore the island of Sylt (German Bight). *Geo-Mar. Lett.* **2016**, *37*, 289–303. [CrossRef]

21. Schimel, A.C.G.; Brown, C.J.; Ierodiaconou, D. Automated Filtering of Multibeam Water-Column Data to Detect Relative Abundance of Giant Kelp (*Macrocystis pyrifera*). *Remote Sens.* **2020**, *12*, 1371. [CrossRef]

22. Czechowska, K.; Feldens, P.; Tuya, F.; De Esteban, M.C.; Espino, F.; Haroun, R.; Schönke, M.; Otero-Ferrer, F. Testing Side-Scan Sonar and Multibeam Echosounder to Study Black Coral Gardens: A Case Study from Macaronesia. *Remote Sens.* **2020**, *12*, 3244. [CrossRef]

23. Feldens, P.; Schulze, I.; Papenmeier, S.; Schönke, M.; Von Deimling, J.S. Improved Interpretation of Marine Sedimentary Environments Using Multi-Frequency Multibeam Backscatter Data. *Geosciences* **2018**, *8*, 214. [CrossRef]

24. Held, P.; Von Deimling, J.S. New Feature Classes for Acoustic Habitat Mapping—A Multibeam Echosounder Point Cloud Analysis for Mapping Submerged Aquatic Vegetation (SAV). *Geosciences* **2019**, *9*, 235. [CrossRef]

25. Janowski, L.; Trzcinska, K.; Tegowski, J.; Kruss, A.; Rucinska-Zjadacz, M.; Pocwiardowski, P. Nearshore Benthic Habitat Mapping Based on Multi-Frequency, Multibeam Echosounder Data Using a Combined Object-Based Approach: A Case Study from the Rowy Site in the Southern Baltic Sea. *Remote Sens.* **2018**, *10*, 1983. [CrossRef]

26. Lurton, X.; Lamarche, G.; Brown, C.; Lucieer, V.; Rice, G.; Schimel, A.; Weber, T. *Backscatter Measurements by Seafloor-Mapping Sonars: Guidelines and Recommendations*. 2015, p. 200. Available online: https://niwa.co.nz/static/BWSG_REPORT_MAY2015_web.pdf (accessed on 8 December 2021).

27. Planke, S.; Erikson, F.N.; Berndt, C.; Mienert, J.; Masson, D.G. P-Cable High-Resolution Seismic. *Oceanography* **2009**, *22*, 85. [CrossRef]

28. Marsset, B.; Missiaen, T.; De Roeck, J.M.; Noblem, M.; Versteeg, R.J.; Henriet, J.P. Very high resolution 3D marine seismic data processing for geotechnical applications. *Geophys. Prospect.* **1998**, *46*, 105–120. [CrossRef]

29. Wilken, D.; Wunderlich, T.; Hollmann, H.; Schwardt, M.; Rabbel, W.; Mohr, C.; Schulte-Kortnack, D.; Nakoinz, O.; Enzmann, J.; Jürgens, F.; et al. Imaging a medieval shipwreck with the new PingPong 3D marine reflection seismic system. *Archaeol. Prospect.* **2019**, *26*, 211–223. [CrossRef]

30. Wilken, D.; Wunderlich, T.; Feldens, P.; Coolen, J.; Preston, J.; Mehler, N. Investigating the Norse Harbour of Igaliku (Southern Greenland) Using an Integrated System of Side-Scan Sonar and High-Resolution Reflection Seismics. *Remote Sens.* **2019**, *11*, 1889. [CrossRef]

31. Gutowski, M.; Malgorn, J.; Vardy, M. 3D sub-bottom profiling—high resolution 3D imaging of shallow subsurface structures and buried objects. In Proceedings of the OCEANS 2015—Genova, Genova, Italy, 18–21 May 2015; pp. 1–7. [CrossRef]

32. Wildman, R.A.; Huettel, M. Acoustic detection of gas bubbles in saturated sands at high spatial and temporal resolution: Acoustic detection of bubbles in sand. *Limnol. Oceanogr. Methods* **2012**, *10*, 129–141. [CrossRef]

33. Orr, M.H.; Rhoads, D.C. Acoustic imaging of structures in the upper 10 cm of sediments using a megahertz backscattering system: Preliminary results. *Mar. Geol.* **1982**, *46*, 117–129. [CrossRef]

34. Suganuma, H.; Mizuno, K.; Asada, A. Application of wavelet shrinkage to acoustic imaging of buried asari clams using high-frequency ultrasound. *Jpn. J. Appl. Phys.* **2018**, *57*, 07LG08. [CrossRef]

35. Mizuno, K.; Liu, X.; Katase, F.; Asada, A.; Murakoshi, M.; Yagita, Y.; Fujimoto, Y.; Shimada, T.; Watanabe, Y. Automatic non-destructive three-dimensional acoustic coring system for in situ detection of aquatic plant root under the water bottom. *Case Stud. Nondestruct. Test. Eval.* **2016**, *5*, 1–8. [CrossRef]

36. Mizuno, K.; Yu, Z.; Murakoshi, M.; Suganuma, H.; Asada, A.; Fujimoto, Y.; Takahashi, Y.; Shimada, T. Survey of the Lotus Root Habitats in the Sediment Using Acoustic Coring System. In Proceedings of the 2018 OCEANS-MTS/IEEE Kobe Techno-Oceans, Kobe, Japan, 28–31 May 2018; pp. 1–5.

37. Dorgan, K.M.; Ballentine, W.; Lockridge, G.; Kiskaddon, E.; Ballard, M.S.; Lee, K.M.; Wilson, P.S. Impacts of simulated infaunal activities on acoustic wave propagation in marine sediments. *J. Acoust. Soc. Am.* **2020**, *147*, 812–823. [CrossRef]

38. Leighton, T.G.; Evans, R.C.P. The detection by sonar of difficult targets (including centimetre-scale plastic objects and optical fibres) buried in saturated sediment. *Appl. Acoust.* **2008**, *69*, 438–463. [CrossRef]

39. Schwinghamer, P.; Guigne, J.Y.; Siu, W.C. Quantifying the impact of trawling on benthic habitat structure using high resolution acoustics and chaos theory. *Can. J. Fish. Aquat. Sci.* **1996**, *53*, 288–296. [CrossRef]

40. Stockwell, J.W. The CWP/SU: Seismic Un∗x package. *Comput. Geosci.* **1999**, *25*, 415–419. [CrossRef]

41. Thomas, M.H.; SegyMAT. Zenodo. Available online: http://doi.org/10.5281/zenodo.1305289 (accessed on 8 December 2021).

42. Stolt, R.H. Migration by fourier transform. *Geophysics* **1978**, *43*, 23–48. [CrossRef]

43. Yilmaz, Ö. *Seismic Data Analysis: Processing, Inversion, and Interpretation of Seismic Data*; Society of Exploration Geophysicists: Houston, TX, USA, 2001.

44. Zettler, M.L.; Alf, A. *Bivalvia of German Marine Waters of the North and Baltic Seas*; ConchBooks: Harxheim, Germany, 2021.

45. Tauber, F.; Lemke, W.; Endler, R. Map of Sediment Distribution in the Western Baltic Sea (1: 100,000), Sheet Falster—Mon. *Dtsch. Hydrogr. Z.* **1999**, *51*, 27. [CrossRef]

46. Nickell, L.A.; Black, K.D.; Hughes, D.J.; Overnell, J.; Brand, T.; Nickell, T.D.; Breuer, E.; Harvey, S.M. Bioturbation, sediment fluxes and benthic community structure around a salmon cage farm in Loch Creran, Scotland. *J. Exp. Mar. Biol. Ecol.* **2003**, *285-286*, 221–233. [CrossRef]

47. Michaud, E.; Desrosiers, G.; Mermillod-Blondin, F.; Sundby, B.; Stora, G. The functional group approach to bioturbation: The effects of biodiffusers and gallery-diffusers of the Macoma balthica community on sediment oxygen uptake. *J. Exp. Mar. Biol. Ecol.* **2005**, *326*, 77–88. [CrossRef]

48. Wetzel, A.; Werner, F.; Stow, D. Bioturbation and Biogenic Sedimentary Structures in Contourites. *Dev. Sedimentol.* **2008**, *60*, 183–202. [CrossRef]

49. Stanton, T.K.; Chu, D. On the acoustic diffraction by the edges of benthic shells. *J. Acoust. Soc. Am.* **2004**, *116*, 239–244. [CrossRef] [PubMed]

50. Stief, P.; Poulsen, M.; Nielsen, L.P.; Brix, H.; Schramm, A. Nitrous oxide emission by aquatic macrofauna. *Proc. Natl. Acad. Sci. USA* **2009**, *106*, 4296–4300. [CrossRef] [PubMed]

51. Lurton, X. *An Introduction to Underwater Acoustics: Principles and Applications*, 2nd ed.; Springer Science & Business Media: Chichester, UK, 2010.

52. Gay, A.; Mourgues, R.; Berndt, C.; Bureau, D.; Planke, S.; Laurent, D.; Gautier, S.; Lauer, C.; Loggia, D. Anatomy of a fluid pipe in the Norway Basin: Initiation, propagation and 3D shape. *Mar. Geol.* **2012**, *332–334*, 75–88. [CrossRef]

Chapter 6

Conclusion

Mapping of the ocean and seas is crucial for a sustainable use and an everlasting process as continuous monitoring is necessary. Existing, changing and newly arising pressures are a challenge to conservation and observation. Monitoring measures must be permanently adapted, while benefiting from recent technological and methodological developments.

This thesis investigated benthic life on object-based to local scale, using frequencies in the range from 130 kHz to 700 kHz. The investigated range reached from stones and boulders at the seafloor surface of the Baltic Sea to 20 cm sediment depth in the laboratory experiment. Different acoustic systems were used to record data sets supported by ground truthing in form of sedimentological and biological sampling and video footage. Despite the variety of investigated objects and settings, this thesis illustrates and expands the potential of hydroacoustic methods to detect benthic life.

The methods developed in this thesis improve habitat mapping in many ways. Habitats can be differentiated in more detail by the use of multiple frequencies. The study offshore the island of Sylt (Chapter 2) showed many features in the multifrequency backscatter maps, which were not visible in monofrequency maps, but interpretation was difficult due to lack in sufficiently positioned ground truthing data. In the Hohe Düne study (Chapter 4) densely spaced sampling stations and additional video profiles composed a solid ground truthing for the three habitat types. The low frequency (200 kHz) showed an increased sensitivity to changes in the shallow subsurface with the inhabiting benthic community. Tubeworms (Chapter 2) and seagrass rhizomes (Chapter 4) created heterogeneities in the sediment volume possibly influencing the backscatter strength. High frequencies (550 to 700 kHz) were found to highlight changes in coarse sediments, which can potentially improve the mapping of the ecologically valuable coarse sand and gravel areas in the Baltic Sea. However, in the case of mussel clusters on fine sand (Chapter 3), frequency differences in backscatter strength are low, but the study shows that already low mussel abundances influence the scattering at the seafloor surface.

Seasonal habitat changes are known from biological perspective but were not quantified in terms of acoustic backscatter responses. Considering the seasonal state while backscatter interpretation is indispensable as shown by the study in the Baltic Sea (Chapter 4). Backscatter intensity is influenced by the the growth state of seagrass blades or shifts of surface sediments due to local hydrodynamics. In case of the reef covered by mussels, seasonal dynamics seemed to be small with exception of a dense layer of red algae in August, which could not be detected in the hydroacoustic data. Further, this survey emphasized the need for the calibration of MBES backscatter to assess temporal and spatial habitat dynamics. More investigations will be necessary to achieve a more comprehensive idea of the habitat-specific backscatter responses and finally a catalog for the acoustic remote sensing of marine habitats.

Proper ground truthing is essential for the interpretation of hydroacoustic data. The composition and structure of the near subsurface comes to the fore when utilizing low frequencies. The 3D seismic lander (Chapter 5) showed its potential as a new (ground truthing) method for imaging of the very shallow subsurface using a high frequency of 130 kHz. In the laboratory, objects with less than 1 cm in diameter could be detected in soft sediments with a thickness of 20 cm. Furthermore, the intensity and extent of manual disturbances of the sediment could be distinguished, proving the potential for the imaging and quantification of bioturbation.

6.1   Outlook

The multifrequency backscatter investigations were successful for a small selection of benthic habitats. The expansion to more areas could lead to a hydroacoustic remote sensing catalog of Baltic Sea habitats in the future and an improved habitat monitoring.

The azimuth dependence of backscatter strength is another possible discrimination feature regarding benthic habitats (Lurton, Eleftherakis, & Augustin, 2018). A survey at the study site in Hohe Düne (Chapter 4) was repeated at three different azimuth directions for two frequencies each. Data processing and thorough investigation are still pending.

The 3D models derived from video data of the study in Chapter 3 enhanced the spatial visualization of the seafloor including the mussel clusters. Point clouds exported from the 3D model can be used to calculate roughness spectra of the to quantify the impact of mussels on surface roughness. This can be expanded by and compared to roughness spectra derived from laser line scanning of (different) shells on sand to further quantify and investigate the impact on backscatter intensities.

The 3D seismic lander (Chapter 5) was successfully tested during laboratory experiments with a soft, well sorted sediment. Performance when changing to coarser sediments or a layering of different substrates needs to be tested. A field application, which was not possible during the pandemic, is hopefully conducted in the near future. A possible combination with a laser line scanner (Schönke et al., 2017), available within the working group, opens up even more perspectives for an innovative ground truthing and the in situ observation of (burrowing) macrobenthos. The repeated measurement of the same seismic volume could investigate the temporal dynamics of bioturbation by benthic organisms. Finally, future work will focus on improving the discrimination of objects and the implementation of different waveforms.

References

References cited in the papers can be found at the end of the corresponding chapters in order of appearance.
The following list includes references from Chapters 1, 3 and 6 in alphabetical order.

Attard, K., Rodil, I., Berg, P., Mogg, A., Westerbom, M., Norkko, A., & Glud, R. (2020). Metabolism of a subtidal rocky mussel reef in a high-temperate setting: pathways of organic C flow. *Marine Ecology Progress Series*, *645*, 41–54.

Ballard, M. S., Lee, K. M., Sagers, J. D., Venegas, G. R., McNeese, A. R., Wilson, P. S., & Rahman, A. F. (2020). Application of acoustical remote sensing techniques for ecosystem monitoring of a seagrass meadow. *The Journal of the Acoustical Society of America*, *147*(3), 2002–2019. doi: 10.1121/10.0000954

Barstow, S. (1983). The ecology of Langmuir circulation: A review. *Marine Environmental Research*, *9*(4), 211–236. doi: 10.1016/0141-1136(83)90040-5

Beisiegel, K., Darr, A., Gogina, M., & Zettler, M. L. (2017). Benefits and shortcomings of non-destructive benthic imagery for monitoring hard-bottom habitats. *Marine Pollution Bulletin*, *121*(1-2), 5–15. doi: 10.1016/j.marpolbul.2017.04.009

Björg, S. (1995). A Review of the History of the Baltic Sea, 13.0-8.0 ka BP. *Quaternary International*, *27*, 22–40.

Blondel, P., & Gómez Sichi, O. (2009). Textural analyses of multibeam sonar imagery from Stanton Banks, Northern Ireland continental shelf. *Applied Acoustics*, *70*(10), 1288–1297. doi: 10.1016/j.apacoust.2008.07.015

Briggs, K. B., Williams, K. L., Richardson, M. D., & Jackson, D. R. (2001). Effects of Changing Roughness on Acoustic Scattering: (1) Natural Changes. *Proc. Inst. Acoust.*, *23*(part 2), 343–390.

Brown, C. J., & Blondel, P. (2009). Developments in the application of multibeam sonar backscatter for seafloor habitat mapping. *Applied Acoustics*, *70*(10), 1242–1247. doi: 10.1016/j.apacoust.2008.08.004

Brown, C. J., Smith, S. J., Lawton, P., & Anderson, J. T. (2011). Benthic habitat mapping: A review of progress towards improved understanding of the spatial ecology of the seafloor using acoustic techniques. *Estuarine, Coastal and Shelf Science*, *92*(3), 502–520. doi: 10.1016/j.ecss.2011.02.007

Böttner, C., Gross, F., Geersen, J., Crutchley, G. J., Mountjoy, J. J., & Krastel, S. (2018). Marine Forearc Extension in the Hikurangi Margin: New Insights From High-Resolution 3-D Seismic Data. *Tectonics*, *37*(5), 1472–1491. doi: 10.1029/2017TC004906

Bøe, R., Bjarnadóttir, L. R., Elvenes, S., Dolan, M., Bellec, V., Thorsnes, T., ... Longva, O. (2020). Revealing the secrets of Norway's seafloor – geological mapping within the MAREANO programme and in coastal areas. *Geological Society, London, Special Publications*, SP505–2019–82. doi: 10.1144/SP505-2019-82

Clarke, J. E. H. (2015). Multispectral Acoustic Backscatter from Multibeam, Improved Classification Potential. In *Proceedings of the United States Hydrographic Conference, San Diego, CA, USA* (pp. 15–19).

Colbo, K., Ross, T., Brown, C., & Weber, T. (2014). A review of oceanographic applications of water column data from multibeam echosounders. *Estuarine, Coastal and Shelf Science*, *145*, 41–56. doi: 10.1016/j.ecss.2014.04.002

Costa, B. (2019). Multispectral Acoustic Backscatter: How Useful Is it for Marine Habitat Mapping and Management? *Journal of Coastal Research*, *35*(5), 1062. doi: 10.2112/JCOASTRES-D-18-00103.1

Davenport, J., & Davenport, J. L. (2006). The impact of tourism and personal leisure transport on coastal environments: A review. *Estuarine, Coastal and Shelf Science*, *67*(1-2), 280–292. doi: 10.1016/j.ecss.2005.11.026

Diesing, M., Green, S. L., Stephens, D., Lark, R. M., Stewart, H. A., & Dove, D. (2014). Mapping seabed sediments: Comparison of manual, geostatistical, object-based image analysis and machine learning approaches. *Continental Shelf Research*, *84*, 107–119. doi: 10.1016/j.csr.2014.05.004

Diesing, M., Thorsnes, T., & Bjarnadóttir, L. R. (2021). Organic carbon densities and accumulation rates in surface sediments of the North Sea and Skagerrak. *Biogeosciences*, *18*(6), 2139–2160. doi: 10.5194/bg-18-2139-2021

Directive, H. (1992). Council Directive 92/43/EEC of 21 May 1992 on the conservation of natural habitats and of wild fauna and flora. *Official Journal of the European Union*, *206*, 7–50.

Dryzek, J. S., & Pickering, J. (2018). *The Politics of the Anthropocene*. Oxford University Press.

Eleftheriou, A., & Moore, D. C. (2013). Macrofauna Techniques. In A. Eleftheriou (Ed.), *Methods for the Study of Marine Benthos* (pp. 175–251). Oxford, UK: John Wiley & Sons, Ltd. doi: 10.1002/9781118542392.ch5

European Commission. (2017). *Commission Decision (EU) 2017/848 of 17 May 2017 laying down criteria and methodological standards on good environmental status of marine waters and specifications and standardised methods for monitoring and assessment, and repealing Decision 2010/477/EU (Text with EEA relevance.).* Retrieved 2022-05-19, from `http://data.europa.eu/eli/dec/2017/848/oj/eng` (Legislative Body: COM, ENV)

European Parliament, Council of the European Union. (2008). *Directive 2008/56/EC of the European Parliament and of the Council of 17 June 2008 establishing a framework for community action in the field of marine environmental policy (Marine Strategy Framework Directive) (Text with EEA relevance)* (Vol. 164).

Feldens, P. (2017). Sensitivity of Texture Parameters to Acoustic Incidence Angle in Multibeam Backscatter. *IEEE Geoscience and Remote Sensing Letters*, *14*(12), 2215–2219. doi: 10.1109/LGRS.2017.2756258

Feldens, P., Schulze, I., Papenmeier, S., Schönke, M., & Schneider von Deimling, J. (2018). Improved Interpretation of Marine Sedimentary Environments Using Multi-Frequency Multibeam Backscatter Data. *Geosciences*, *8*(6), 214. doi: 10.3390/geosciences8060214

Ferrini, V. L., & Flood, R. D. (2006). The effects of fine-scale surface roughness and grain size on 300 kHz multibeam backscatter intensity in sandy marine sedimentary environments. *Marine Geology*, *228*(1-4), 153–172. doi: 10.1016/j.margeo.2005.11.010

Fonseca, L., Brown, C., Calder, B., Mayer, L., & Rzhanov, Y. (2009). Angular range analysis of acoustic themes from Stanton Banks Ireland: A link between visual interpretation and multibeam echosounder angular signatures. *Applied Acoustics*, *70*(10),

1298–1304. doi: 10.1016/j.apacoust.2008.09.008

Fonseca, L., & Mayer, L. (2007). Remote estimation of surficial seafloor properties through the application Angular Range Analysis to multibeam sonar data. *Marine Geophysical Researches*, *28*(2), 119–126. doi: 10.1007/s11001-007-9019-4

Gaida, T. C., Tengku Ali, T. A., Snellen, M., Amiri-Simkooei, A., van Dijk, T. A. G. P., & Simons, D. G. (2018). A Multispectral Bayesian Classification Method for Increased Acoustic Discrimination of Seabed Sediments Using Multi-Frequency Multibeam Backscatter Data. *Geosciences*, *8*(12), 455. doi: 10.3390/geosciences8120455

Hansen, S. S., Ernstsen, V. B., Andersen, M. S., Al-Hamdani, Z., Baran, R., Niederwieser, M., . . . Kroon, A. (2021). Classification of Boulders in Coastal Environments Using Random Forest Machine Learning on Topo-Bathymetric LiDAR Data. *Remote Sensing*, *13*(20), 4101. doi: 10.3390/rs13204101

Harris, P. T. (2020). Anthropogenic threats to benthic habitats. In *Seafloor Geomorphology as Benthic Habitat* (pp. 35–61). Elsevier. doi: 10.1016/B978-0-12-814960-7.00003-8

Harris, P. T., & Baker, E. K. (2020). Why map benthic habitats? In *Seafloor Geomorphology as Benthic Habitat* (pp. 3–15). Elsevier. doi: 10.1016/B978-0-12-814960-7 .00001-4

Hasan, R. C., Ierodiaconou, D., & Monk, J. (2012). Evaluation of Four Supervised Learning Methods for Benthic Habitat Mapping Using Backscatter from Multi-Beam Sonar. *Remote Sensing*, *4*(11), 3427–3443. doi: 10.3390/rs4113427

Heinrich, C., Feldens, P., & Schwarzer, K. (2017). Highly dynamic biological seabed alterations revealed by side scan sonar tracking of Lanice conchilega beds offshore the island of Sylt (German Bight). *Geo-Marine Letters*, *37*(3), 289–303. doi: 10.1007/ s00367-016-0477-z

HELCOM. (2018). State of the Baltic Sea – Second HELCOM holistic assessment 2011-2016. *Baltic Sea Environment Proceedings*, *155*.

Held, P., & Schneider von Deimling, J. (2019). New Feature Classes for Acoustic Habitat Mapping—A Multibeam Echosounder Point Cloud Analysis for Mapping Submerged Aquatic Vegetation (SAV). *Geosciences*, *9*(5), 235. doi: 10.3390/geosciences9050235

Hellequin, L., Boucher, J. M., & Lurton, X. (2003). Processing of high-frequency multibeam echo sounder data for seafloor characterization. *IEEE J. Oceanic Eng.*, *28*(1), 78–89. doi: 10.1109/JOE.2002.808205

Howe, J. A., Stevenson, A., & Gatliff, R. (2014). Seabed Mapping for the 21st Century – The Marine Environmental Mapping Programme (MAREMAP): Preface. *Earth and Environmental Science Transactions of the Royal Society of Edinburgh*, *105*(4), 239–240. doi: 10.1017/S175569101500016X

Huff, L. C. (2008). Acoustic Remote Sensing as a Tool for Habitat Mapping in Alaska Waters. In J. Reynolds & H. Greene (Eds.), *Marine Habitat Mapping Technology for Alaska* (pp. 29–46). Alaska Sea Grant, University of Alaska Fairbanks. doi: 10.4027/mhmta.2008.03

Hustoft, S., Mienert, J., Bünz, S., & Nouzé, H. (2007). High-resolution 3D-seismic data indicate focussed fluid migration pathways above polygonal fault systems of the mid-Norwegian margin. *Marine Geology*, *245*(1-4), 89–106. doi: 10.1016/j.margeo.2007 .07.004

Inter-Departmental Marine Coordination Group. (2012). *Harnessing Our Ocean Wealth: An Integrated Marine Plan for Ireland*. Inter-Departmental Marine Coordination Group.

Jackson, D., & Richardson, M. (2007). *High-Frequency Seafloor Acoustics*. Springer Science & Business Media.

Janowski, L., Trzcinska, K., Tegowski, J., Kruss, A., Rucinska-Zjadacz, M., & Pocwiardowski, P. (2018). Nearshore Benthic Habitat Mapping Based on Multi-Frequency,

Multibeam Echosounder Data Using a Combined Object-Based Approach: A Case Study from the Rowy Site in the Southern Baltic Sea. *Remote Sensing*, *10*(12), 1983. doi: 10.3390/rs10121983

Jørgensen, L. L., Renaud, P. E., & Cochrane, S. K. (2011). Improving benthic monitoring by combining trawl and grab surveys. *Marine Pollution Bulletin*, *62*(6), 1183–1190. doi: 10.1016/j.marpolbul.2011.03.035

Kanneworff, E., & Nicolaisen, W. (1972). The "haps" a frame-supported bottom corer. *Ophelia*, *10*(2), 119–128.

Karstens, J., Berndt, C., Urlaub, M., Watt, S. F. L., Micallef, A., Ray, M., . . . Brune, S. (2019). From gradual spreading to catastrophic collapse – Reconstruction of the 1888 Ritter Island volcanic sector collapse from high-resolution 3D seismic data. *Earth and Planetary Science Letters*, *517*, 1–13. doi: 10.1016/j.epsl.2019.04.009

Kruss, A., Tęgowski, J., Tatarek, A., Wiktor, J., & Blondel, P. (2017). Spatial distribution of macroalgae along the shores of Kongsfjorden (West Spitsbergen) using acoustic imaging. *Polish Polar Research*, *38*(2), 205–229. doi: 10.1515/popore-2017-0009

Kuhwald, K., Schneider von Deimling, J., Schubert, P., & Oppelt, N. (2021). How can Sentinel-2 contribute to seagrass mapping in shallow, turbid Baltic Sea waters? *Remote Sensing in Ecology and Conservation*, *n/a*(n/a). (_eprint: https://onlinelibrary.wiley.com/doi/pdf/10.1002/rse2.246) doi: 10.1002/rse2.246

L-3 Communications SeaBeam Instruments. (2000). *Multibeam Sonar - Theory of Operation* (Tech. Rep.). East Walpole, MA. Retrieved 2022-05-02, from `https://www3.mbari.org/data/mbsystem/sonarfunction/SeaBeamMultibeamTheoryOperation.pdf`

Lamarche, G., & Lurton, X. (2018). Recommendations for improved and coherent acquisition and processing of backscatter data from seafloor-mapping sonars. *Marine Geophysical Research*, *39*(1), 5–22. doi: 10.1007/s11001-017-9315-6

Lucieer, V., Hill, N. A., Barrett, N. S., & Nichol, S. (2013). Do marine substrates 'look' and 'sound' the same? Supervised classification of multibeam acoustic data using autonomous underwater vehicle images. *Estuarine, Coastal and Shelf Science*, *117*, 94–106. doi: 10.1016/j.ecss.2012.11.001

Lurton, X. (2010). *An Introduction to Underwater Acoustics: Principles and Applications* (2nd ed.). Berlin Heidelberg: Springer-Verlag.

Lurton, X., Eleftherakis, D., & Augustin, J.-M. (2018). Analysis of seafloor backscatter strength dependence on the survey azimuth using multibeam echosounder data. *Marine Geophysical Research*, *39*(1-2), 183–203. doi: 10.1007/s11001-017-9318-3

Lurton, X., & Lamarche, G. (2015). Backscatter measurements by seafloor - mapping sonars. Guidelines and Recommendations. Retrieved 2022-05-28, from `https://niwa.co.nz/static/BWSG_REPORT_MAY2015_web.pdf`

Mejer Hansen, T. (2019, April). *SegyMAT*. Zenodo. Retrieved 2020-01-13, from `https://zenodo.org/record/1305289` doi: 10.5281/zenodo.1305289

Niemeyer, J., Song, Y., Kogut, T., & Heipke, C. (2015). Untersuchungen zum einsatz der laserbathymetrie in der seevermessung. *Project Report (Federal Hydrographic Agency BSH, Germany)*.

Norén, F., Haamer, J., & Lindahl, O. (1999). Changes in the plankton community passing a Mytilus edulis mussel bed. *Marine Ecology Progress Series*, *191*, 187–194. doi: 10.3354/meps191187

Roche, M., Degrendele, K., Vrignaud, C., Loyer, S., Le Bas, T., Augustin, J.-M., & Lurton, X. (2018). Control of the repeatability of high frequency multibeam echosounder backscatter by using natural reference areas. *Marine Geophysical Research*, *39*(1-2), 89–104. doi: 10.1007/s11001-018-9343-x

Schneider von Deimling, J., Brockhoff, J., & Greinert, J. (2007). Flare imaging with multi-

beam systems: Data processing for bubble detection at seeps: FLARE IMAGING. *Geochemistry, Geophysics, Geosystems*, *8*(6). doi: 10.1029/2007GC001577

Schneider von Deimling, J., & Feldens, P. (2021). ECOMAP. *Hydrographische Nachrichten*(120), 13–22. doi: 10.23784/HN120-02

Schneider von Deimling, J., Held, P., Feldens, P., & Wilken, D. (2016). Effects of using inclined parametric echosounding on sub-bottom acoustic imaging and advances in buried object detection. *Geo-Marine Letters*, *36*(2), 113–119. doi: 10.1007/s00367-015-0433-3

Schneider von Deimling, J., Weinrebe, W., Tóth, Z., Fossing, H., Endler, R., Rehder, G., & Spieß, V. (2013). A low frequency multibeam assessment: Spatial mapping of shallow gas by enhanced penetration and angular response anomaly. *Marine and Petroleum Geology*, *44*, 217–222. doi: 10.1016/j.marpetgeo.2013.02.013

Schulze, I., Wilken, D., Zettler, M. L., Gogina, M., Schönke, M., & Feldens, P. (2021). Laboratory Measurements to Image Endobenthos and Bioturbation with a High-Frequency 3D Seismic Lander. *Geosciences*, *11*(12), 508. doi: 10.3390/geosciences11120508

Schönke, M., Feldens, P., Wilken, D., Papenmeier, S., Heinrich, C., von Deimling, J. S., ... Krastel, S. (2017, June). Impact of Lanice conchilega on seafloor microtopography off the island of Sylt (German Bight, SE North Sea). *Geo-Marine Letters*, *37*(3), 305–318. doi: 10.1007/s00367-016-0491-1

Schönke, M., Wiesenberg, L., Schulze, I., Wilken, D., Darr, A., Papenmeier, S., & Feldens, P. (2019). Impact of Sparse Benthic Life on Seafloor Roughness and High-Frequency Acoustic Scatter. *Geosciences*, *9*(10), 454. doi: 10.3390/geosciences9100454

Steffen, W., Broadgate, W., Deutsch, L., Gaffney, O., & Ludwig, C. (2015). The trajectory of the Anthropocene: The Great Acceleration. *The Anthropocene Review*, *2*(1), 81–98. doi: 10.1177/2053019614564785

Stock, A. (2015). Satellite mapping of Baltic Sea Secchi depth with multiple regression models. *International Journal of Applied Earth Observation and Geoinformation*, *40*, 55–64. doi: 10.1016/j.jag.2015.04.002

Stockwell, J. W. (1999). The CWP/SU: Seismic Unx package. *Computers & Geosciences*, *25*(4), 415–419. Retrieved 2020-01-13, from `http://www.sciencedirect.com/science/article/pii/S0098300498001459` doi: 10.1016/S0098-3004(98)00145-9

Stolt, R. H. (1978). Migration by Fourier transform. *Geophysics*, *43*(1), 23–48. (Society of Exploration Geophysicists)

Tauber, F. (2012). *Meeresbodensedimente in der deutschen Ostsee= Seabed sediments in the German Baltic Sea.* Bundesamt für Seeschifffahrt und Hydrographie.

Tecchiato, S., Collins, L., Parnum, I., & Stevens, A. (2015). The influence of geomorphology and sedimentary processes on benthic habitat distribution and littoral sediment dynamics: Geraldton, Western Australia. *Marine Geology*, *359*, 148–162. doi: 10.1016/j.margeo.2014.10.005

Tulldahl, H. M., & Wikström, S. A. (2012). Classification of aquatic macrovegetation and substrates with airborne lidar. *Remote Sensing of Environment*, *121*, 347–357. doi: 10.1016/j.rse.2012.02.004

Turley, C., Keizer, T., Williamson, P., Gattuso, J.-P., Ziveri, P., Monroe, R., ... Huelsenbeck, M. (2016). *Hot, Sour and Breathless - Oceans under stress.* Plymouth Marine Laboratory, UK Ocean Acidification Research Programme, European Project on Ocean Acidification, Mediterranean Sea Acidification in a Changing Climate project, Scripps Institution of Oceanography at UC San Diego, OCEANA.

Turner, W., Spector, S., Gardiner, N., Fladeland, M., Sterling, E., & Steininger, M. (2003). Remote sensing for biodiversity science and conservation. *Trends in Ecology & Evolution*, *18*(6), 306–314. doi: 10.1016/S0169-5347(03)00070-3

United Nations. (n.d.-a). *THE 17 GOALS | Sustainable Development.* Retrieved 2022-05-19, from `https://sdgs.un.org/goals`

United Nations. (n.d.-b). *The Ocean Decade - The Science we need for the Ocean we want.* Retrieved 2022-05-28, from `https://www.oceandecade.org/`

United Nations Environment Programme. (2012). *Green economy in a blue world: synthesis report.* Retrieved from `http://www.unep.org/pdf/green_economy_blue.pdf` (OCLC: 789678308)

van der Zee, E. M., van der Heide, T., Donadi, S., Eklöf, J. S., Eriksson, B. K., Olff, H., ... Piersma, T. (2012). Spatially Extended Habitat Modification by Intertidal Reef-Building Bivalves has Implications for Consumer-Resource Interactions. *Ecosystems*, *15*(4), 664–673. doi: 10.1007/s10021-012-9538-y

Walker, T. R., Adebambo, O., Del Aguila Feijoo, M. C., Elhaimer, E., Hossain, T., Edwards, S. J., ... Zomorodi, S. (2019). Environmental Effects of Marine Transportation. In *World Seas: an Environmental Evaluation* (pp. 505–530). Elsevier. doi: 10.1016/B978-0-12-805052-1.00030-9

Weber, T. C., Rice, G., & Smith, M. (2018). Toward a standard line for use in multibeam echo sounder calibration. *Marine Geophysical Research*, *39*(1-2), 75–87. doi: 10.1007/s11001-017-9334-3

Weinrebe, W. (2020). Observations of marine life in the Indian Ocean by hydroacoustic water column imaging. *Hydrographische Nachrichten*(117), 6–12. doi: 10.23784/HN117-01

Westerbom, M., Lappalainen, A., Mustonen, O., & Norkko, A. (2018). Trophic overlap between expanding and contracting fish predators in a range margin undergoing change. *Scientific Reports*, *8*(1), 7895. doi: 10.1038/s41598-018-25745-6

Wohlfarth, B., Björg, S., Funder, S., Houmark-Nielsen, M., Ingólfsson, , Lunkka, J.-P., ... Vorren, T. (2008). Quaternary of Norden. *Episodes Journal of International Geoscience*, *31*(1), 73–81.

Yilmaz, (2001). *Seismic data analysis: Processing, inversion, and interpretation of seismic data.* Society of exploration geophysicists.

Appendix A

Appendix

A.1 Funding

A.2 Acknowledgements

There are many people I would like to acknowledge and thank for their assistance throughout this thesis:

Thanks to Prof. Helge Arz, for taking on the supervision of this dissertation project.

Peter Feldens, thank you for initiating this dissertation project and giving me the opportunity to learn from you, while leaving free space for own ideas. I am grateful for your support and encouragement when it was needed.

Thanks to my colleagues of the working group 'Marine Geophysics' at IOW, Mischa Schönke, Svenja Papenmeier, Agata Feldens, Matthias Hinz, for your support and help, cruises and conference visits together, many relaxing coffee breaks, open ears, and a wonderful work atmosphere.

Thanks to Gerald Nickel, for constructing the 3D seismic lander, a less successful trip to a polish lake and a lot of patience during many hours together surveying on Klaashahn.

Thanks to all members of the Geology Section at IOW for company during lunches and coffee breaks.

Thanks to Michael L. Zettler, Mayya Gogina and the working group 'Ecology of Benthic Organisms' at IOW for a successful cooperation, surveys together and answering questions.

Thanks to the Werkstatt at IOW, helping whenever they can and for driving the Klaashahn at Hohe Düne for many hours along very short profiles.

Thanks to the members of the ECOMAP project, especially Jens Schneider von Deimling as the coordinator, I learned a lot during the enjoyable meetings and summer schools.

Thanks to two experts in the field for giving the 3D seismic lander such a beautiful name as OWUHRSE... OverWhelmingly Ulta-High-Resolution Seismic Experience...

Thanks to Herrn D. Brockmann for his proficient and inspiring way of teaching physics in high school, which especially motivated my decision of studying the Physics of the Earthsystem.

Thanks to my parents and sister for always supporting me!

Thanks to Christoph for everything
and Astrid for taking my mind off the work and making me laugh!

"It's the frequency..."
(Kakkmaddafakka, 2019)